Simulating Miocene warmth: insights from an opportunistic Multi-Model ensemble (MioMIP1)

Natalie J Burls[1], Catherine Bradshaw[2], Agatha Margaretha De Boer[3], Nicholas Herold[4], Matthew Huber[5], Matthew Pound[6], Yannick Donnadieu[7], Alexander Farnsworth[8], Amanda Frigola Boix[9], Edward G. W. Gasson[8], Anna von der Heydt[10], David Karel Hutchinson[3], Gregor Knorr[11], Kira T Lawrence[12], Caroline H. Lear[13], Xiangyu Li[14], Gerrit Lohmann[15], Daniel J. Lunt[8], Alice Marzocchi[16], Matthias Prange[17], Catherine Anne Riihimaki[18], Anta-Clarisse Sarr[19], Nicholas Siler[20], and Zhongshi Zhang[21]

[1]George Mason University
[2]Exeter University
[3]Stockholm University
[4]University of New South Wales
[5]Purdue University
[6]Northumbria University
[7]CEREGE (Centre Européen de Recherche et d'Enseignement des Géosciences de l'Environnement)
[8]University of Bristol
[9]MARUM
[10]Universiteit Utrecht, Utrecht
[11]AWI Bremerhaven
[12]Lafayette College
[13]Cardiff University
[14]Institute of Atmospheric Physics, Chinese Academy of Sciences
[15]AWI
[16]National Oceanography Centre
[17]MARUM - Zentrum für Marine Umweltwissenschaften
[18]Princeton University
[19]Aix Marseille Univ, CNRS, IRD, Coll France, INRA, CEREGE
[20]Oregon State University
[21]China University of Geoscience, Wuhan

November 24, 2022

Abstract

The Miocene epoch, spanning 23.03-5.33Ma, was a dynamic climate of sustained, polar amplified warmth. Miocene atmospheric CO2 concentrations are typically reconstructed between 300-600ppm and were potentially higher during the Miocene Climatic Optimum (16.75-14.5Ma). With surface temperature reconstructions pointing to substantial midlatitude and polar warmth, it is unclear what processes maintained the much weaker-than-modern equator-to-pole temperature difference. Here we synthesize several Miocene climate modeling efforts together with available terrestrial and ocean surface temperature reconstructions. We

evaluate the range of model-data agreement, highlight robust mechanisms operating across Miocene modelling efforts, and regions where differences across experiments result in a large spread in warming responses. Prescribed CO2 is the primary factor controlling global warming across the ensemble. On average, elements other than CO2, such as Miocene paleogeography and ice sheets, raise global mean temperature by ˜ 2, with the spread in warming under a given CO2 concentration (due to a combination of the spread in imposed boundary conditions and climate feedback strengths) equivalent to ˜1.2 times a CO2 doubling. This study uses an ensemble of opportunity: models, boundary conditions, and reference datasets represent the state-of-art for the Miocene, but are inhomogeneous and not ideal for a formal intermodel comparison effort. Acknowledging this caveat, this study is nevertheless the first Miocene multi-model, multi-proxy comparison attempted so far. This study serves to take stock of the current progress towards simulating Miocene warmth while isolating remaining challenges that may be well served by community-led efforts to coordinate modelling and data activities within a common analysis framework.

Simulating Miocene warmth: insights from an opportunistic Multi-Model ensemble (MioMIP1)

N. J. Burls[1], C. D. Bradshaw[2], A. M. De Boer[3], N. Herold [4], M. Huber[5], M. Pound[6], Y. Donnadieu[7], A. Farnsworth[8], A. Frigola [9], E. Gasson[10], A. S. von der Heydt[11], D. K. Hutchinson[12], G. Knorr[13], K. T. Lawrence[14], C. H. Lear [15], X. Li[16], G. Lohmann[17], D. J. Lunt[18], A. Marzocchi[19], M. Prange[20], C. A. Riihimaki[21], A.-C. Sarr[22], N. Siler[23], and Z. Zhang[24,25]

[1] Department of Atmospheric, Oceanic and Earth Sciences & the Center for Ocean-Land-Atmosphere Studies, George Mason University, Fairfax, VA 22030, USA.

[2]The Global Systems Institute, University of Exeter, EX4 4QE, United Kingdom and Met Office Hadley Centre, Exeter EX1 3PB, United Kingdom.

[3]Department of Geological Sciences and Bolin Center for Climate Research, Stockholm University, 10691 Stockholm, Sweden.

[4]The NSW Department of Planning, Industry and Environment, Science Division, Climate and Atmospheric Science, New South Wales, Australia.

[5]Department of Earth, Atmospheric, and Planetary Sciences, Purdue University, West Lafayette, IN, 47907, USA.

[6]Department of Geography and Environmental Sciences, Northumbria University, Newcastle, NE1 8ST, UK.

[7]Aix Marseille Univ, CNRS, IRD, Coll France, INRA, CEREGE, 13545, Aix en Provence, France.

[8]School of Geographical Sciences, University of Bristol, Bristol, BS8 1SS, UK.

[9]MARUM – Center for Marine Environmental Sciences, University of Bremen, Klagenfurter Str., D-28359 Bremen, Germany.

[10]School of Geographical Sciences, University of Bristol, Bristol, BS8 1SS, UK.

[11]Institute for Marine and Atmospheric Research, Department of Physics, Faculty of Science, Utrecht University, Princetonplein 5, 3584CC Utrecht, The Netherlands.

[12]Department of Geological Sciences and Bolin Center for Climate Research, Stockholm University, 10691 Stockholm, Sweden.

[13]Alfred Wegener Institute Helmholtz Centre for Polar and Marine Research, Bussestrasse 24, D-27570, Germany.

[14]Department of Geology and Environmental Geosciences, Lafayette College, 102 Van Wickle Hall, Easton, PA 18042, USA.

[15]School of Earth and Ocean Sciences, Cardiff University, Main Building, Park Place, Cardiff, CF10 3AT, UK.

[16]Department of Atmospheric Science, School of Environmental studies, China University of Geoscience, Wuhan, 430074, China.

[17]Alfred Wegener Institute Helmholtz Centre for Polar and Marine Research, Bussestrasse 24, D-27570, Germany.

[18]School of Geographical Sciences, University of Bristol, Bristol, BS8 1SS, UK.

[19]National Oceanography Centre, Southampton, UK.

[20]MARUM – Center for Marine Environmental Sciences, University of Bremen, Klagenfurter Str., D-28359 Bremen, Germany.

[21]Council on Science and Technology, Princeton University, Princeton, NJ 08544, USA.

[22]Aix Marseille Univ, CNRS, IRD, Coll France, INRA, CEREGE, 13545, Aix en Provence, France.

[23]College of Earth, Ocean, and Atmospheric Sciences, Oregon State University, Corvallis, OR, USA.

[24]Department of Atmospheric Science, School of Environmental studies, China University of Geoscience, Wuhan, 430074, China.

[25]NORCE Norwegian Research Centre, Bjerknes Centre for Climate Research, 5007 Bergen, Norway.

Corresponding author: Natalie J. Burls (nburls@gmu.edu)

Key Points:

- A synthesis of Miocene modelling efforts, and surface temperature reconstructions, is presented within a single analysis framework.
- Miocene GMST estimates span ~5.3-11.5°C higher than preindustrial, only ~2°C is explain by non-CO_2 boundary conditions in climate models.
- Some simulations overlap with reconstructed global mean surface temperature estimates but fail to capture the weak temperature gradient.

Abstract

The Miocene epoch, spanning 23.03-5.33Ma, was a dynamic climate of sustained, polar amplified warmth. Miocene atmospheric CO_2 concentrations are typically reconstructed between 300-600ppm and were potentially higher during the Miocene Climatic Optimum (16.75-14.5Ma). With surface temperature reconstructions pointing to substantial midlatitude and polar warmth, it is unclear what processes maintained the much weaker-than-modern equator-to-pole temperature difference. Here we synthesize several Miocene climate modeling efforts together with available terrestrial and ocean surface temperature reconstructions. We evaluate the range of model-data agreement, highlight robust mechanisms operating across Miocene modelling efforts, and regions where differences across experiments result in a large spread in warming responses. Prescribed CO_2 is the primary factor controlling global warming across the ensemble. On average, elements other than CO_2, such as Miocene paleogeography and ice sheets, raise global mean temperature by ~ 2℃, with the spread in warming under a given CO_2 concentration (due to a combination of the spread in imposed boundary conditions and climate feedback strengths) equivalent to ~1.2 times a CO_2 doubling. This study uses an ensemble of opportunity: models, boundary conditions, and reference datasets represent the state-of-art for the Miocene, but are inhomogeneous and not ideal for a formal intermodel comparison effort. Acknowledging this caveat, this study is nevertheless the first Miocene multi-model, multi-proxy comparison attempted so far. This study serves to take stock of the current progress towards simulating Miocene warmth while isolating remaining challenges that may be well served by community-led efforts to coordinate modelling and data activities within a common analysis framework.

Plain Language Summary

As human activity continues to increase atmospheric carbon dioxide concentrations, scientists turn to warm intervals in Earth's history to develop insight into the behavior of the climate system under elevated carbon dioxide and temperature. One such interval is the Miocene epoch which has become increasingly relevant as reconstructions of Miocene atmospheric CO_2 concentrations point to values ranging between current concentrations of ~400ppm and those projected for the end of this century under Shared Socioeconomic Pathways 3 & 4. In this study we evaluate the surface warming patterns simulated by a range of different climate models configured with Miocene paleogeography and CO_2 concentrations spanning 200 to 850 ppm. We also synthesize available Miocene surface temperature reconstructions. The primary factor controlling the amount of global warming seen across the Miocene simulations analyzed is the CO_2 concentration that was prescribed within a given simulation. On average, Miocene elements other than CO_2, such as Miocene paleogeography and ice sheets, raise global mean temperature by ~2℃. While some Miocene simulations with high CO_2 forcing overlap with the reconstructed global mean surface temperature estimates for their target Miocene interval, they still generally fail to capture the reconstructed warming pattern of warming.

1 Introduction

The Miocene epoch (23.03-5.33 Ma) encompasses much of the range of climate states between the Cenozoic endmembers of peak Eocene warmth and the modern ice-house state with extensive glaciation at both poles (Fig. 1). Terrestrial and marine records show that Miocene climate was significantly warmer than today and highly dynamic. Oxygen isotope records of

benthic foraminifera ($\delta^{18}O_c$) show that peak Miocene warmth and minimum ice volume occurred in the Early to Middle Miocene (16.75-14.5 Ma), known as the Miocene Climate Optimum (MCO) (Fig. 1). During the MCO, current reconstructions suggest that sea surface temperatures (SSTs) were 8-10°C warmer than present in the high southern latitudes (Shevenell et al., 2004) and 10-15°C warmer in the high northern latitudes (Super et al., 2020), while deep ocean temperatures were ~5-8°C warmer (Lear et al., 2000; Lear et al., 2015), leading to an estimated global mean surface temperature anomaly of 7.6 ± 2.3°C compared to preindustrial (Goldner et al., 2014). The warmer conditions shifted the bioclimatic zones poleward (Pound et al., 2012). While the extent of the Greenland glaciation remains unclear (Thiede et al., 2011), it contributed negligibly to global ice volume and there is evidence to suggest that even during the late Miocene the Arctic experienced sea ice free summers (Stein et al. 2016). Regions of Antarctica supported woody temperate vegetation that graded into tundra further inland with a much-reduced ice sheet extent (Warny et al., 2009; Pound et al., 2012; Sangiorgi et al., 2018). Although cooler than the peak warmth of the MCO, in the late Miocene (11.6-5.33 Ma) SSTs still ranged between 10-15°C warmer than modern in the high latitudes, and 2-4°C warmer in the Tropics (LaRiviere et al., 2012; Herbert et al., 2016), while temperatures in the deep ocean are estimated to have been ~4°C warmer than present (LaRiviere et al., 2012). Geochemical and ice rafted debris records indicate increasing prevalence of colder temperatures as cooling progressed into the late Miocene (Winkler et al., 2002, Stein et al., 2016). The wide dynamic range of Miocene climate implies either strong sensitivity to forcing or strong and highly variable forcings through the Miocene.

The driving forces behind Miocene warmth and its fluctuations remain enigmatic, and several aspects have been difficult to reconcile with CO_2 reconstructions that are generally similar to modern or end-of-century projections (Fig. 1). Typical proxy estimates for the Miocene are in the 300-600 ppmv range (Fig. 1, Foster et al., 2012, 2017; Sosdian et al, 2018), although during the MCO recent reconstructions suggest that CO_2 may have been as high as 800-1100ppm (Sosdian et al., 2018; Stoll et al., 2019). A full description of the Miocene CO_2 reconstructions and their uncertainties is given in Section 8 of Steinthorsdottir et al. (this issue). A prolonged carbon isotope excursion between ~16.7 Ma and ~13.5 Ma (the Monterey Excursion; Vincent and Burger, 1985) documents a marked perturbation of the carbon cycle at this time, modulated by orbital forcing. It is suggested that this excursion is due to enhanced organic matter burial on submerged continental shelves and higher CO_2 concentrations resulting in higher biological carbon isotope fractionation (Sosdian et al., 2020).
With CO_2 concentrations in the 300-600ppmv range, it has not been possible to simulate the observed polar amplified warmth of the Miocene, as well as the lack of summer sea-ice more typical of mid-to-late Miocene conditions (Stein et al. 2016). A long-term decrease in the global carbon isotopic composition record for the late Miocene coincides with the long-term decrease in global temperatures, suggesting that carbon cycle changes were the driver for late Miocene global cooling.

Numerous studies have therefore explored the role of other potential mechanisms. Although geologically recent, paleogeographic differences between the Miocene and today are substantial. There were major differences in ocean gateway configurations such as connections between the Pacific and Atlantic Oceans, the Atlantic and Indian Oceans, and the Indian and Pacific Oceans, which today are either restricted or closed completely (Fig. 2). Mountain building was occurring in all of the world's major mountain chains in the Miocene (see He et al, this issue), which transformed local hydrological regimes. Changes in the land surface itself may

also be important for driving global warmth. Smaller ice sheets at both poles likely contributed to the polar amplified warmth and the weaker latitudinal temperature gradient of the time. Vegetation distributions resulting from a warmer global climate may itself provide a stabilizing feedback mechanism to maintain that warmth (e.g. Knorr et al. 2011; Bradshaw et al., 2015). As described in more depth in the following section, while these mechanisms have been shown to contribute to warming in models, they generally fall short of explaining the full extent, and the polar amplified spatial structure, of Miocene warmth (also see summary in Steinthorsdottir et al., this issue).

In this paper we synthesize available Miocene modeling efforts, together with available terrestrial and ocean surface temperature reconstructions, within a single analysis framework. We evaluate the current range of model-data agreement, highlight robust mechanisms operating across Miocene modelling efforts, as well as the regions where the differences across models (coming from a combination of model differences in imposed non-CO_2 Miocene boundary conditions and model feedbacks) result in a large spread in warming responses. In section 2, we provide some background on Miocene modelling and the motivation for this study. In Section 3, we detail the Miocene modelling efforts analyzed, as well as the Miocene surface temperature records that we have synthesized to facilitate a model-data comparison and Miocene global mean surface temperature estimates. The intermodel analysis is presented in Section 4, where we discuss global mean warmth, simulated warming patterns and present the model-data comparison. We conclude with Section 5.

2 Background

Climate model simulations pertaining to the Miocene date to the early days of climate modelling itself. Experiments to assess the role of uplift of the Himalayas and the Tibetan Plateau and of the American Rockies found that lower orography resulted in marked changes in precipitation patterns and warmer winter temperatures, but that the magnitude of the temperature change simulated was insufficient to rule out the need for other climate forcings (Ruddiman and Kutzbach, 1989; Kutzbach et al., 1993). These early simulations used atmosphere-only models, however, and more recent coupled atmosphere-ocean models show that uplift of the Tibetan Plateau also impacts ocean circulation resulting in far-field warming (Su et al., 2018).

Several modelling studies have investigated the role of changes in ocean gateways. Miocene Ocean General Circulation Models (OGCMs) simulating an open Isthmus of Panama tend to have a net volume transport that is eastward from the Pacific to the Atlantic Ocean (Maier-Reimer et al., 1990; Mikolajewicz et al., 1993; Zhang et al., 2012b). Water from the Pacific Ocean is fresher than that in the Atlantic Ocean, causing these modelling studies with an open Isthmus of Panama to simulate a freshening of the North Atlantic, a resulting weakening of North Atlantic Deep Water (NADW) formation and strength of the Atlantic Meridional Overturning Circulation (AMOC). This reorganization of ocean circulation results in cooling of the Northern Hemisphere and warming of the Southern Hemisphere, but the global mean annual temperature changes are small (~+0.25°C or less, Lunt et al., 2008). With a wide-open Panama Gateway there no longer needs to be a strong relationship between NADW formation and the AMOC, the North Atlantic can import water through the open Isthmus and through Tethys in the surface branch and exported in through the Panama Gateway in the deep branch. Although the Isthmus would have been closing throughout the Miocene, most proxy records show that NADW did not strengthen significantly until after the Miocene (Burton et a, 1997; Ling, 1997; Lear et

al., 2003; Bartoli et al., 2005; Haug and Tiedemann, 1998; O'Dea et al., 2016). That said, NADW probably initiated and fluctuated in strength since the late Eocene (Coxall et al., 2018). Therefore, although the timing of emergence of the Isthmus is still hotly debated (e.g. Montes et al., 2012), tectonic changes in this region are not thought to be the cause of Miocene warmth. Together with the Isthmus of Panama, the depth and width of other ocean gateways may have also played a role in the Miocene temperature distribution. It has been suggested that the closure of the Tethys tropical connection between Indian and Atlantic Oceans, together with a deepening or widening of the Drake Passage induced a reversal of the net ocean flow through the Isthmus (Omta and Dijkstra 2003; von der Heydt and Dijkstra 2006) approximately in the Early Miocene. Before the Tethys closure, net transport through the Isthmus was towards the Pacific, while after closure it was directed towards the Atlantic as several other Miocene GCMs have shown. Nevertheless, independent of the net flow direction in the Isthmus, GCM simulations show export of Northern Component Water formed in the Atlantic (though much weaker than present) towards the Pacific (von der Heydt and Dijkstra 2006), keeping intermediate-to-deep waters relatively warm compared to present day (Sijp et al 2014); the latter holds in particular for the closed-Tethys situation, which is representative of most of the middle-to-late Miocene.

Modelling studies which have taken all of the reconstructed paleogeographic, ice sheet and vegetation differences into account simultaneously show that these changes alone (discounting any CO_2 differences or orbital variability) make the Miocene world globally warmer than today. For preindustrial CO_2 concentrations, the models estimate that annual mean temperatures are warmer than preindustrial conditions by 0.3°C to 3°C (Herold et al., 2011; Knorr et al., 2011; Bradshaw et al., 2012) for the late Miocene and 3.1°C for the middle Miocene (Stärz et al., 2017) due to these non-greenhouse gas forcings. For middle Miocene boundary conditions, even with a slightly lower CO_2 concentration than preindustrial (at 200 ppm), a global annual mean temperature 1.7°C warmer than modern has been simulated (Frigola et al., 2018). The anomaly between the Miocene temperatures and modern temperatures scales with the CO_2 concentration, however, because of higher Miocene climate sensitivity (Knorr and Lohmann, 2014; Bradshaw et al., 2015). Miocene model experiments also show that the combined Miocene boundary conditions make the world wetter than today (Herold et al., 2011; Knorr et al., 2011; Bradshaw et al., 2012, 2015; Stärz et al., 2017; Frigola et al., 2018).

The inability of Miocene simulations to capture the full extent of the polar amplified warmth and meridional temperature gradient reduction reflected in reconstructions is a problem that is not unique to the Miocene. Historically it has been equally challenging to fully simulate the high-latitude warmth of the Eocene (Huber and Sloan, 2001; Huber and Caballero 2011), but the latest DeepMIP effort which targets the Eocene has seen some improvement - two of the DeepMIP models show improved skill in capturing elements of the polar amplification (Lunt et al., 2020) as reconstructed by a comprehensive synthesis of all the available Eocene data (Hollis et al., 2019). In the DeepMIP ensemble, the non-CO_2 component of warming from preindustrial to Eocene boundary conditions ranges from 3°C to 5°C (Lunt et al., 2020). This indicates that a significant contribution to warming comes from paleogeographic forcing, including vegetation changes, and ice-albedo effects. The improved model-data agreement seen in these Eocene simulations is likely also related to the better representation of cloud microphysics overall (Sagoo et al, 2013; Kiehl and Shields 2013; Zhu et al, 2019). Interestingly, the two DeepMIP models that best represented the proxy data were also the two models that implemented adapted aerosol concentrations, either coupling aerosols to a new cloud microphysics scheme (CESM; Zhu et al., 2019) or including aerosol forcing as a new fixed boundary condition (GFDL;

Hutchinson et al., 2018; Lunt et al., 2020). These aerosol changes influence cloud microphysics and hence the radiative properties of these simulations and represent a major advance in their physical realism, but one that is largely unconstrained by geological data (Huber, 2013).

If the Eocene and DeepMIP is the warmer endmember for the Miocene, the Late Pliocene which has been a target of the Pliocene Model Intercomparison Project represents the cooler endmember. This model intercomparison project is now in its second phase (PlioMIP2, Haywood et al. 2016), with a more tightly constrained time slice defined compared to the first phase aimed at reducing uncertainty in the proxy data. Because the Late Pliocene paleogeography is much more similar to modern day, the non-CO_2 component of warming is much smaller than for DeepMIP. The polar amplification shown in PlioMIP2 is similar to that shown for RCP simulations. Global annual mean surface air warming for the multi-model ensemble of PlioMIP2 is 3.2˚C (with a range between 1.7 and 5.2˚C) relative to pre-industrial. All of these simulations use an atmospheric CO_2 concentration of 400 ppm. The multi-model-mean warming is larger than for the previous phase of PlioMIP and this is a result of the contribution of ensemble members from recent models with modified aerosol and cloud microphysics, that have a relatively high climate sensitivity (Haywood et al., 2020). PlioMIP2 models exhibit polar amplification that is in better agreement with proxies than in PlioMIP1 models (Haywood et al, 2011; Haywood et al, 2013), at mid and high latitudes, in part due to re-assessment of high latitude proxy records (McClymont et al, 2020), and in part due to changes in configuration of the Bering Straits (Haywood et al, 2020, Otto-Biesner et al, 2016) in the model simulations. Pliocene model-data comparisons can also provide constraints on climate sensitivity (Haywood et al, 2020; Renoult et al, 2020; Hargreaves and Annan, 2016), the relationship between climate sensitivity and Earth system sensitivity (Haywood et al, 2020; Lunt et al, 2010), and the contribution to warming from non-CO_2 forcings (Chandan and Peltier, 2018). Overall, the Pliocene represents a world that is in equilibrium with near-modern CO_2 forcing, and exhibits a climate similar to that expected at the end of this century under relatively optimistic emissions scenarios (Burke et al, 2018)

Although the Miocene represents a climate state in-between that of the early Eocene and the mid-Pliocene, and presents unique modelling challenges, no formal MIP exists for the Miocene. The existing Miocene model-data comparison efforts have used different proxy datasets and validation techniques (Micheels et al., 2011; Bradshaw et al., 2012; Krapp and Jungclaus, 2011; and Herold et al., 2011; Goldner et al., 2014), and are restricted to interpreting results in a single model framework. Here we seek to take advantage of the fact that several Miocene modelling efforts have been conducted and evaluate them within a single, consistent, model-data comparison framework to establish not only the degree of model-data agreement in simulating Miocene warmth but also the spread in model responses.

As a community we have endeavored to take the first step toward the ideal solution of having a model-model and model-data intercomparison effort with uniform boundary conditions and standardized reference proxy data sets. Taking a similar approach as in the early steps of the DeepMIP process (Lunt et al, 2012), we have surveyed the existing modelling experiments and sorted them into two groups based on the Miocene time period they have targeted: 1) Late Miocene experiments with a paleogeography that falls within 11.6-5.3Ma (Tortonian & Messinian) & 2) Middle to Early Miocene experiments with paleogeography that falls within 20-11.6Ma (Burdigalian, Langhian & Serravallian). Unlike a formal model intercomparison where the same boundary conditions are used in each model, it is difficult to isolate the model

dependence of the climate response to specific forcing (e.g. CO_2 versus paleogeography). Nevertheless, the informal model intercomparison presented in this paper serves to provide a "multi-model-ensemble of opportunity" view of the spread in model responses to a range of Miocene boundary conditions and CO_2 forcings, within a single model-data comparison framework; an approach that has previously been used in deep-time paleoclimate modelling (Lunt et al, 2012). The results presented in this paper serve to synthesize the current range of model-data agreement seen across Miocene modelling efforts to date, highlight robust mechanisms operating across Miocene modelling efforts, and take stock of the current progress towards simulating Miocene warmth while isolating remaining challenges. Our eventual aim is to catalyze a formalized and community-based MioMIP project.

3 Methods

3.1 Available Modelling Efforts

Several studies targeting the Miocene have been performed by modelling groups across the globe. In this section we provide a brief overview of the simulations performed by these studies as summarized in Tables 1, 2 and 3. Table 1 summarizes the modelling studies targeting the Late Miocene 11.63-5.333Ma (Messinian and Tortonian), Table 2 summarizes the modelling studies targeting Middle/Early Miocene 11.6-20Ma (Burdigalian, Langhian & Serravallian). There are 10 Late Miocene and 31 Middle/Early Miocene experiments with a total of 41 experiments analyzed. Table 3 lists two additional sets of Miocene simulations from studies in which sensitivity to orbital changes were assessed. A summary of the key characteristics associated with the various baseline paleogeographic forcing used is provided in Table 4. All of the fully coupled model simulations have been run for at least 1100 years and so the atmosphere and surface ocean are considered to have reached a state of near equilibrium.

CCSM3-NH: A series of simulations have been published using the National Center for Atmospheric Research (NCAR) Community Climate System Model (CCSM3) to simulate Middle to Early Miocene climate utilizing the boundary conditions of Herold et al (2008), i.e. Herold et al (2010), You et al (2009), or the updated boundary conditions of Herold et al. (2011a), i.e. Herold et al. 2011b, 2012. The details of these CCSM3 simulations are summerized in Tables 1 & 2. Table 4 summerizes the key features associated with the Herold et al. 2011a paleogeography boundary conditions which have been widely used by other groups and have formed the basis for some other Miocene boundary condition efforts. For the sake of this intercomparison study, output from the last 100 years of the CCSM3-NH simulation (Herold et al., 2011b, 2012; Table 2) run for 1100 years have been provided, at which point global mean ocean temperature varied by less than 0.01° per century.

CCSM3 T42 (MARUM): CCSM3 T42 (MARUM) simulations have been performed for the periods just before (Middle Miocene Climate Optimum; MMCO) and after (Middle Miocene Glaciation; MMG) the Middle Miocene Climate Transition around 13-15 Ma (Table 2). These two experiments differ in the atmospheric CO_2 concentration (400 ppmv in MMCO and 200 ppmv in MMG) and the volume of the Antarctic ice sheet (43 m difference in sea-level equivalent). In addition, two sensitivity experiments with respect to atmospheric CO_2 have been carried out: experiment MMCO_200 uses the MMCO Antarctic ice sheet but an atmospheric CO_2 level of 200 ppmv, while MMG_400 uses the larger MMG ice sheet but an atmospheric CO_2 level of 400 ppm. All other greenhouse gases as well as ozone distribution, aerosols, solar

constant and orbital configuration were set to pre-industrial levels. All Miocene experiments use Middle Miocene global topography, bathymetry and vegetation as described in Frigola et al. (2018). The experiments were integrated for a total of 1500 years each, where the last 100 years were used for analyses.

CCSM4: Following on from Goldner et al. (2014) which used a "slab ocean", fully coupled simulations have been conducted using version 1.0.5 of the Community Earth System Model with version 4 of the Community Atmosphere Model (the equivalent of CCSM4; Gent et al., 2011). The CESM1.0 model improvements, in comparison to older generation models, are described in previous work focused on both modern-day climate (Bitz et al., 2012; Neale et al., 2010) and paleoclimate (Shields et al., 2012; Goldner et al., 2014). >2000 years were simulated. The simulations were initialized with initial conditions from the prior CCSM3-NH simulations so that they equilibrated quickly, and were run with Early to Middle Miocene boundary conditions updated from Herold et al. (2008) and Herold et al. (2011; 2012). These updates to the paleogeography were extensive (Fig. 2b) and not previously described. We therefore provide a description of how these boundary conditions where constructed (Supplementary Text S1) and make them available to the community (Supplementary Dataset S1). These simulations used the bulk aerosol mode (BAM) with preindustrial aerosols prescribed.

CESM1-CAM5: The CESM1-CAM5 simulations are run using Miocene boundary conditions that are essentially identical to those used in the CCSM4 simulations. The updated paleogeography described above are used throughout. Orbital parameters and other boundary conditions follow the pre-industrial configuration.

The main difference between the CCSM4 and CESM1-CAM5 cases lies in the physics of the atmospheric component. CAM5 has many improvements over its predecessors in its handling of clouds and aerosols (Neale et al., 2010, Bacmeister et al., 2012; Gettleman et al., 2008, 2010, 2015), radiative transfer (Iacono et al., 2008), deep convection (Neale et al., 2010), and shallow convection and moist boundary layer processes (Bretherton and Park, 2009). The combination of these improvements in physical parameterization allow for the simulation of complete aerosol-cloud interactions of cloud droplet activation by aerosols, precipitation processes due to particle size dependent behavior, and explicit radiative interaction of cloud particles. These simulations are run with the standard CAM5 3-mode modal aerosol mode (MAM). The aerosol flux is tuned to be close to the preindustrial control flux. Using MAM ensures self-consistent aerosol-cloud microphysical interaction.

As described in Zhou et al. (2018) these CESM1-CAM5 simulations were initialized from the end of the CCSM4 simulations (at 2,200 model years). The CCSM4 simulation were equilibrated with a surface radiative imbalance of 0.08 Wm^{-2}. The CESM1-CAM5 simulation used here was continued for another 1800 years at which point the global mean surface temperature was nearly unchanged and the long-term mean surface radiative imbalance was 0.07 Wm^{-2}. These simulations were then extended, and the output archived for this study.

COSMOS (AWI): COSMOS, with its ECHAM5 (Roeckner et al. 2003) atmospheric component and MPIOM (Marsland et al. 2003) oceanic component, has been used for simulating the Late Miocene in Knorr et al. (2011) and the Middle Miocene Climate transition in Knorr and Lohmann (2014). For further details regarding the paleogeography reconstruction and proxy-based reconstruction of the Late Miocene vegetation refer to Micheels et al., (2007), Micheels et al. (2011) and the references therein. The corresponding boundary conditions are available at

PANGAEA (Knorr et al., 2019). Further details on ECHAM5/MPIOM are described in Jungclaus et al. (2006). Furthermore, Middle to Early Miocene simulations have been performed in a COSMOS model configuration (Stäerz et al. 2017; Huang et al., 2017) that additionally include dynamical vegetation as part of the land surface scheme JSBACH (Raddatz et al., 2007; Brovkin et al., 2009). The model setup targets the Middle to Early Miocene time period (~23–15 Ma) using the boundary conditions of Herold et al. (2008), including orography, paleobathymetry, and ice sheet adjustments. Additionally, a regional high-resolution bathymetric reconstruction comprising the North Atlantic/Arctic Ocean (Ehlers and Jokat, 2013) has been implemented.

Genesis-slab ocean: The Genesis simulations were performed to provide boundary meteorology to an Antarctic regional climate model; they have different Antarctic ice sheet extents and have extremes of astronomical parameters that lead to highs (ecc. = 0.05, obliquity = 24.5˚, longitude of precession = 270˚) and lows (ecc. = 0.05, obliquity = 22.5˚, longitude of precession = 90˚) of insolation for Antarctica. Simulations were also performed with an astronomical configuration similar to modern day (ecc. = 0, obliquity = 23.5˚) . The atmospheric is coupled to a 50-m slab diffusive mixed-layer ocean and dynamical sea-ice model (Thompson and Pollard, 1997). The runs include dynamic vegetation and oxygen isotope tracing. The paleogeography is from Herold et al., (2008) with modifications to Antarctica. Simulations were run for 50 years with 30 years used for analysis.

HadCM3L-Bradshaw: These simulations use the HadCM3LB-M2.1a (Valdes et al., 2017) coupled atmosphere-ocean general circulation model with a dynamic vegetation scheme. The late Miocene simulations were run for 2100 years and the middle Miocene simulations continue on from the late Miocene simulations and have been run for a further 2000 years. The last 50 years of the simulations are used for analyses. Both the late Miocene and the middle Miocene configurations use paleogeographies from Markwick, 2007.

HadCM3L-Marzocchi: These orbital parameter sensitivity simulations are initialized from the end of the 2100-year late Miocene simulation by Bradshaw et al. (2012), so the model setup is identical to that described above as “HadCM3L-Bradshaw”. These simulations are all run for an additional 200 years with varying orbital parameters. Climatological means of the last 50 years of simulation are used for analyses.

HadCM3L-Farnsworth: These simulations use the HadCM3LB-M2.1a (Valdes et al., 2017) coupled atmosphere-ocean general circulation model with a dynamic vegetation scheme. The Getech Plc. paleogeographic (topography, bathymetry, ice sheets) boundary conditions are the same as Farnsworth, et al. (2019b) with stage specific solar luminosity for the Langhian, Tortonian and Messinian (see tables 1 and 2) as calculated by Gough et al. (1981). *p*CO2 is set to 400ppm (as well as two sensitivity studies at 280ppm and 560ppm) in line with proxy estimates (Foster, et al. 2018). Each simulation is integrated for 7422 model years and has reached equilibrium in both the atmosphere and deep ocean with climate means taken from the last 100 years of each run. Each simulation was initialized from a stationary state in the ocean with the atmosphere initialized from a preindustrial state (for full details see Lunt, et al. 2017; Farnsworth, et al. 2019a).

IPSLCM5A2: These simulations use the IPSL-CM5A2 Earth System Model (Sepulchre et al. 2019), which is built upon IPSL-CM5A-LR; the Coupled Model Intercomparision Project phase 5 (CMIP5) Earth System Model developed at IPSL (Institut Pierre-Simon Laplace,

Dufresne et al., 2013). As IPSL-CM5A-LR, it is composed of the LMDZ atmospheric model (Hourdin et al., 2013), the ORCHIDEE land surface and vegetation model (Krinner et al., 2005), and the NEMO ocean model (NEMO v3.6, Madec, 2008), which include modules for ocean dynamics (OPA8.2), biochemistry (PISCES, Aumont et al. 2015) and sea-ice (LIM2). Atmospheric and oceanic grids are connected via a coupler (OASIS, Valcke, 2006). The ocean domain is an irregular tri-polar grid (ORCA2, Madec & Imbard, 1996, Dufresne et al., 2013). For more detailed descriptions of the model and its different components, the reader is referred to Sepulchre et al. (2019).

NorESM-L: These simulations use NorESM-L which couples the spectral Community Atmosphere Model (CAM4) (Eaton, 2010; Neale et al., 2013) and the Miami Isopycnic Coordinate Ocean Model (MICOM). NorESM-L performs well in simulating the pre-industrial climate (Zhang et al., 2012a) and has good skill in simulating paleoclimates (Zhang et al., 2013; 2014). Detailed introduction of NorESM-L can be found in Zhang et al., 2012a; Bentsen et al., 2013, and the Miocene boundary conditions can be found in Zhang et al., 2014.

3.2 Available Temperature Reconstructions

Here we describe the proxy data sources used in the model-data comparison shown.

3.2.1. Late and Middle Miocene Terrestrial Mean Annual Temperature Estimates

The Bradshaw et al. (2012) synthesis has been used, as is, to provide Late Miocene terrestrial Mean Annual Temperature (MAT) estimates. A new synthesis of global terrestrial MATs has been generated for the Middle Miocene through the updating and expansion of the Pound et al. (2012) and Goldner et al. (2014) syntheses. Most estimates are from fossil plant data and use either the Co-existence Approach, CLAMP or Leaf Margin Analysis. The Co-existence Approach uses the modern climatic range of a fossil taxons nearest living relative to determine the climatic envelope of co-existence for a fossil assemblage (Mosbrugger and Utescher, 1997; Utescher et al., 2014). CLAMP and Leaf Margin Analysis use the morphological characteristics of fossil leaves to determine climatic parameters (Wolfe, 1971; Uhl et al., 2003; Yang et al., 2011). The new synthesis expands the original datasets of 52 to 110 sites with important additional localities in the southern hemisphere (Supplementary Table 1). Additional data points have been synthesized from the published literature with a cut-off date of October 2019. To maximize geographic spread, some sites with published taxa lists and no climate reconstructions have had MAT estimates reconstructed. New MAT reconstructions are based upon the Co-existence Approach, following the advice of Utescher et al. (2014) and the updated dataset of Pound and Salzmann (2017). All error margins and uncertainty ranges follow the published authors, unless none were provided in which case a 5˚C uncertainty range was applied. A subset of the records within this new Middle Miocene MAT dataset, with ages that fall between 14.5-16.75Ma, are used to estimate MCO global mean surface temperature as outlined in Section 3.4.

3.2.2. Late, Middle Miocene and MCO Sea Surface Temperature Estimates

Published Miocene SST reconstructions (Mg/Ca, U^k_{37} and TEX_{86}) have been synthesized from the literature to provide Late and Middle Miocene mean annual SST estimates (Fig. 2 and Supplementary Table 2). The Herbert et al. (2016) U^k_{37} synthesis was used as a starting point. Both the previously published and new records within this dataset were recalibrated/calibrated by Herbert et al. (2016) using the Müller et al. (1998) calibration. Any additional Miocene SST reconstructions not included in Herbert et al. (2016) were then added, without any recalibration

or age model adjustments (i.e. the original calibrations and age models were used). A community effort to place all available records within a common calibration and age model framework, similar to the recent Eocene effort of Hollis et al, (2019), is planned, for which the summary provided in Table S2 can serve as a starting point together with new records published as part of this special issue.

The majority of the Miocene SST records are U^{k}_{37} records to which we assign a 95% confidence interval uncertainty of +-3˚C (Lawrence et al., 2007). This value is aligned with one standard deviation uncertainty estimates of +-1.1˚C (Conte et al., 2006) to +-1.5˚C (Tierney et al., 2018). The remainder are Mg/Ca or TEX_{86} records. Care needs to be taken when interpreting TEX_{86} records as they have been shown to be influenced by temperature signals below the surface mixed layer (Lopes dos Santos et al., 2010). For the TEX_{86} uncertainty estimates, we use the stated the 90 or 95% confidence intervals published with a given record or convert the stated one standard deviation uncertainty estimate to a 95% confidence interval. Care also needs to be taken when using Miocene age Mg/Ca records given uncertainties in the Mg/Ca of seawater, salinity, and pH (Gray and Evans, 2019; Holland et al. 2020). Therefore, whilst most modern Mg/Ca-temperature calibrations have a standard deviation on the order of +-1.2˚C (Anand et al. 2003), here we assign a 95% confidence interval uncertainty of +-4˚C on absolute Mg/Ca SSTs. This Mg/Ca uncertainty estimate is based on the average 95% confidence interval assigned to the Mg/Ca records synthesized for the Eocene in Hollis et al (2019), where the DeepMIP community did a thorough assessment of the impacts of the above mentioned factors on Mg/Ca uncertainty for the Eocene. While a comparable assessment for the Miocene Mg/Ca records is planned, this serves as an appropriate intermediate estimate. Given that the number of ocean surface temperature records from high latitude regions is limited, future analysis may consider comparing against published benthic temperature records.

Late Miocene reconstructed values are defined as all available estimates from a given site falling between 11.63-5.33Ma and Middle Miocene reconstructed values are defined as all available estimates falling between 15.97-11.63Ma. It is important to note that the records differ in temporal resolution and while some records span the entire interval, others cover only a portion. To partially address the caveat that some records are more representative of the end of the Middle Miocene interval while others the beginning, and given that significant cooling occurs towards the end of the Middle Miocene (end of the Langhian though the Serravallian), the sensitivity of the model-data SST bias results to focusing on a narrower interval within the MCO (14.5-16.75Ma) has been assessed - noting however that fewer sites are available for the comparison after this refinement.

3.3 Model-Data Comparison Methodology

The model-data comparison methodology employed in Section 4.3 is similar to that used in previous Miocene studies (Bradshaw et al., 2012; Bradshaw et al., 2015). For each site, the 1 standard deviation (68%) uncertainty intervals are added to the mean reconstruction values across the given timeslice and the site location is translated back to an estimated paleolocation. The method used to estimate these paleolocations uses plate reconstructions consistent with the paleogeographies described in Markwick and Valdes (2004) that were based on Rowley (1995, pers. comm.). All model output is interpolated, using bilinear interpolation, to a common 1-degree by 1-degree grid. Reconstructed values are compared to the minimum and maximum values simulated in the model grid cell containing the reconstructed data, and all adjacent model

grid cells. This allows for data location uncertainties and model uncertainties such as the misplacement of large-scale climate features (it is unreasonable to expect a model to reconstruct the exact climate of a single grid cell, also note that by using degrees this encompasses a larger zonal distance in the tropics than high latitudes). Since the model simulations and data reconstructions are ranges of possible values rather than a single value, the term overlap is used to define where the two value ranges are consistent (see Fig. S1). Bias between the model and data is determined where there is no overlap between the model and data uncertainty ranges and the magnitude of this bias is determined by the degree of separation between the uncertainty intervals of the two datasets (see Fig. S1, note that as illustrated in Fig. S1 this represents the minimum possible bias within the given uncertainty ranges). When, for a given model setup, a grid point that corresponds with a given terrestrial MAT (SST) site location, as well as its neighboring grid points, are in the ocean (over land) the site is removed from the bias calculation.

Note that rather than using the mean reconstructed SST values for the given time interval, +- the assigned data uncertainty, an alternative approach would be to fully encompass the variability in SST estimates seen across the Late Miocene, Middle Miocene and MCO time intervals and use maximum and minimum recorded values plus uncertainty - as in Bradshaw et al. (2012) and Bradshaw et al. (2015). Given that the SST reconstructions have varying temporal resolutions, and are not collocated in time, this approach has the potential to mask spatial covariance signals (e.g. a higher resolution record can capture more of the sample variance even when the two samples have similar means, which in turn could lead to a smaller "bias" derived using the approach outlined above, even though the means are similar). Given that this paper focuses on the ability of Miocene simulations to represent gross features of Miocene warmth, we feel that the use of mean reconstructed SST values is more appropriate in this context.

3.4 Global Mean Surface Temperature Estimates

Global Mean Surface Temperature (GMST) estimates for the Late Miocene, Middle Miocene and MOC are calculated using the proxy MAT and SST syntheses compiled (Section 3.2). We use a method that has been previously employed to provide Eocene GMST estimates. Despite its simplicity, when applied to the same set of Eocene temperature reconstructions (Hollis et al, 2019) this method produces values that are largely consistent with a range of other methods (Inglis et al., 2020). The zonal mean temperature (T) profile at sea level is approximated using a simple model:

$$\mathrm{T}(\phi) \approx a + b\theta + c\cos\phi \quad \text{(eqn. 1)}$$

where the coefficients a, b, and c are chosen to minimize the sum of the squared residuals relative to the Miocene surface temperature proxy data (Fig. 3). As demonstrated in Fig. 3 of Inglis et al. 2020, this model provides an accurate approximation of the modern $\mathrm{T}(\phi)$ profile. For both the MAT and SST data we account for the uncertainty in each temperature estimate by assuming a normal probability distribution around each temperature estimate with the stated uncertainty interval treated as the 90% confidence interval. For the MAT data we also account for the uncertainty in the elevation of each site by assuming a skew-normal distribution with a 90% confidence interval equal to the lowest and highest elevations within all paleotopographic grid points adjacent to the given site (with a lower bound of zero). For the Middle Miocene and MOC calculations, the paleotopography from the Middle Miocene paleogeography described in this article (updated Herold et al., 2012) is used, while the Knorr et al. (2011) paleogeography is

used for the Late Miocene. The temperature and elevation distribution at each site is then randomly sampled and corrected to sea level by applying a lapse-rate adjustment of 6°K/km. This implies that errors in the paleotopography may influence the estimate of global mean surface temperature, and the resolution and fidelity of the paleotopography used will be a possible source of errors when the terrestrial data is included. Using a standard Monte Carlo bootstrapping method, we resample the same number of data points with replacement and find the coefficients in Equation 1 that best fit the sub-sampled data. A probability distribution for $T(\phi)$ is found by repeating this procedure 10,000 times. The result is shown in Fig. 3, with shading indicating +/- one standard deviation. The latitudinally weighed average of $T(\phi)$ is taken to provide an GMST estimate with an associated uncertainty of one standard deviation.

3.5 Zonal Mean Energy Balance Analysis

To established the relative contribution of energy flux convergence and each radiative component to the meridional warming patterns within the Miocene simulations, we employ a 1-D zonal mean energy balance analysis framework (Heinemann et al., 2009; Lunt et al., 2012; Hill et al., 2014; Feng et al., 2017; Lunt et al., 2020). 1-D energy balance is used to approximate zonal mean surface temperature:

$$C\partial_t T(\phi) = SW^{\downarrow}_{toa}(\phi)[1-\alpha(\phi)] + H - \varepsilon\sigma T(\phi)^4 \text{ (eqn. 2)}$$

Where $T(\phi)$ is the zonal mean surface temperature, a function of latitude, ϕ. $SW^{\downarrow}_{toa}$ is the incoming shortwave radiation at the top of the atmosphere, α the planetary albedo defined as $\alpha = \frac{SW^{\uparrow}_{toa}}{SW^{\downarrow}_{toa}}$, H is the combined atmospheric and oceanic energy flux convergence defined as $H = -(SW^{net}_{toa} + LW^{net}_{toa})$, ε is a measure of the emissivity of the atmospheric $\varepsilon = \frac{LW^{\uparrow}_{toa}}{LW^{\uparrow}_{surf}}$, and C the surface heat capacity. When applied to equilibrated or near equilibrated, annual-mean, climatological fields, the term on the left hand side is negligible and simulated zonal mean surface temperature profiles are well approximated by the balance on the right hand side of Equation 2. This balance is between net downward shortwave, net outgoing longwave, and the convergence of energy by atmospheric and ocean energy transport, such that the solution for $T(\phi) = \left[\frac{SW^{\downarrow}_{toa}(\phi)[1-\alpha(\phi)]+H(\phi)}{\varepsilon(\phi)\sigma}\right]^{0.25} \equiv T(\varepsilon, \alpha, H)$.

The change in $T(\phi)$ between each Miocene experiment and its repective control is then $\Delta T(\phi) = T(\varepsilon, \alpha, H) - T(\varepsilon', \alpha', H')$, where the prime respresents the control simulation. Given that changes in ε, α and H are small relative to their absolute values, the contribution of changes in emissivity, albedo and heat transport can be approximated as $\Delta T(\phi) \cong \Delta T_{emm}(\phi) + \Delta T_{alb}(\phi) + \Delta T_{tran}(\phi)$, where $\Delta T_{emm}(\phi) = T(\varepsilon, \alpha, H) - T(\varepsilon', \alpha, H)$, $\Delta T_{alb}(\phi) = T(\varepsilon, \alpha, H) - T(\varepsilon, \alpha', H)$ and $\Delta T_{tran}(\phi) = T(\varepsilon, \alpha, H') - T(\varepsilon', \alpha, H)$.

Using clear-sky (cs) radiative fluxes ΔT_{emm} can be decomposed into the contribution due to the greenhouse effect (CO_2, water vapor and lapse rate), $\Delta T_{gg}(\phi) = T(\varepsilon_{cs}, \alpha_{cs}, H_{cs}) - T(\varepsilon'_{cs}, \alpha_{cs}, H_{cs})$, and longwave cloud changes $\Delta T_{lwc}(\phi) = \Delta T_{emm}(\phi) - \Delta T_{gg}(\phi)$. Similarly ΔT_{alb} can be decomposed into the contribution of clear-sky changes due to surface albedo and

aerosols, $\Delta T_{salb}(\phi) = T(\varepsilon_{cs}, \alpha_{cs}, H_{cs}) - T(\varepsilon_{cs}, \alpha'_{cs}, H_{cs})$, and shortwave cloud changes $\Delta T_{swc}(\phi) = \Delta T_{alb}(\phi) - \Delta T_{salb}(\phi)$.

There are limitations in this diagnostic approach, particularly when it comes to separating out the changes due to clear-sky and cloud radiative forcing in the presence of seaice, and we have not separated the contribution of changes in surface elevation from the greenhouse effect. Nevertheless, it provides insight into the relative contribution of the 5 components, $\Delta T(\phi) \cong \Delta T_{gg}(\phi) + \Delta T_{lwc}(\phi) + \Delta T_{salb}(\phi) + \Delta T_{swc} + \Delta T_{tran}(\phi)$, based on what was feasible given the output available within our MioMIP dataset.

4 Results

4.1 Global Mean Temperature

Across all the Miocene experiments, which span a range of models and paleogeographic boundary conditions, prescribed CO_2 concentration exerts the primary control on the global mean temperature change relative to the preindustrial control climate, explaining around 75% of the variance (Fig. 4a). The best fit regression across these experiments is for a climate sensitivity of $0.97℃/Wm^{-2}$which assuming ~$3.7Wm^{-2}$per CO_2 doubling (this is less valid when doubling at higher CO_2; Etminan et al, 2016) translates into ~3.6℃ per doubling. This first order linear relationship can be used to provide a few additional insights based on this particular ensemble performed with a broad range of boundary conditions reflective of how conditions may have changed throughout the Miocene. Firstly, the X-intercept suggests that the mean impact of the range of non-CO_2 Miocene boundary conditions used is to raise global mean surface temperature by 1.96℃ (this statement ignores non-linear interactions between CO_2 induced temperature changes and temperature changes induced by other changes in the boundary conditions but provides an insightful starting point). Secondly, deviations from this first order linear relationship range from -1.87 to 2.39℃, providing an indication of the spread in warming responses arising due to a combination of the spread in imposed boundary conditions, as well as the spread in climate feedback strengths across models. Using the above stated climate sensitivity estimate of $0.97℃/Wm^{-2}$as an example, this spread in global mean temperature responses is equivalent to an uncertainty of $4.4Wm^{-2}$or 1.2 times the forcing from a CO_2 doubling.

As described in Section 3.4, GMST estimates +/- one standard deviation have been calculated using the Late Miocene, Middle Miocene and MOC syntheses described in Section 3.2. Two different estimates have been derived for each interval, first an estimate derived using both the terrestrial MAT and SST datasets (Fig. 3, top row), and second an estimate based on only the SST data (Fig. 3, bottom row). When both the terrestrial MAT and SST are included, this method estimates Late Miocene GMST as 19.30℃ +/- 0.98, Middle Miocene GMST as 21.21℃ +/- 0.56 and MCO GMST as 22.93℃ +/- 1.01. If the terrestrial sites are excluded, these GMST estimates based only on SST reconstructions are substantially warmer: Late Miocene GMST as 21.95℃ +/- 0.81, Middle Miocene GMST as 24.46℃ +/- 0.81 and MCO GMST as 25.47℃ +/- 1.17. There are several reasons why the terrestrial data might bias the estimate cold, including calibration techniques biased toward the modern temperature range and that many of these records are from mountain ranges (while we have applied a lapse rate correction, it is only as good as our elevation estimate derived from a low resolution paleotopography product which might lead to a cold/warm biasing). On the other hand, the number of SST reconstructions is

limited such that increasing the sample size is needed to constrain the large uncertainty in GMST that falls out of our analysis. Using a preindustrial value of 14℃ (Hansen et al., 2013), Fig. 4a compares these Miocene GMST estimates with the simulated GMST changes. For the Middle Miocene and MCO, with the exception of the COSMOS Late Miocene simulation with 450ppm CO_2, only Middle to Early Miocene simulations with 840-850ppm CO_2 intersect with the GMST change estimates based on both terrestrial MAT and SST. All the simulations fall below the higher SST-only Middle Miocene and MCO GMST change estimates. Of the Late Miocene simulations, the COSMOS simulation with 450ppm and 25% of the modern Antarctic ice sheet height, and the NorESM-L simulation with 560ppm CO_2, intercept the reconstructed Late Miocene GMST change estimate based on both terrestrial MAT and SST. None of the Late Miocene simulations intercept the reconstructed Late Miocene GMST change estimate based only on SST.

4.2 Warming Patterns

Starting with the zonal-mean changes in surface temperature (Figs. S2 & S3), across the entire ensemble the magnitude of tropical warming spans ~ 0 to 8℃, while high-latitude warming (latitude > 60N&S) spans ~ 0 to 38℃ in the SH and ~ 0 to 18℃ in the NH. While there is substantial spread in its magnitude, polar amplified warming is a robust feature across the ensemble (Fig. 5). The wide range of warming responses seen in the SH reflects the range of boundary conditions prescribed for the Antarctic Ice Sheet given the uncertainty in its evolution across the Miocene. Interestingly, once the zonal-mean responses are stratified by prescribed CO_2 concentration, there does not appear to be a consistent mapping between the degree of high-latitude warming and tropical warming, with the degree of polar amplification ranging substantially across the experiments (e.g. when looking at the 560ppm experiments in Fig. S3 widely different high latitude warming due to varying ice sheet extents has a limited impact on tropical temperatures). This result points to a somewhat limited impact of high-latitude glacial changes on the tropics relative to the more systematic influence of CO_2 on tropical temperature (Fig. 5). This feature appears to hold not only across the different models, but within a given model, namely HadCM3L, for which experiments with a range of Antarctic ice-sheets display considerable variability in high-latitude surface temperature but limited variability in tropical temperature (Fig. S3).

Stratifying the energy balance analysis by prescribed CO_2 concentration we see that a stronger polar greenhouse effect (due to CO_2, water vapor and lapse rate) and decreased surface albedo, are the dominant contributors to the polar amplified warming – a result consistent with the literature on future climate change e.g. Pithan and Mauritsen, (2014) . One caveat with differencing the all-sky and clear-sky to separate the surface and cloud albedo components is that the masking of surface albedo changes by clouds is not adequately deconvolved, particularly in the presence of sea ice. For example, in a polar region where climatologically high cloud cover largely masks the influence of surface albedo, the method will overestimate the contribution of reduced surface albedo given that the cloud albedo is taken as the residual between total albedo and surface albedo. Therefore the method can incorrectly indicate a cooling signal due to cloud albedo changes even if cloud properties remain similar to the control. Given this caveat, the high-latitude cooling/warming signal seen in Fig. 5 due to changes in cloud/surface albedo may not be as strong as the analysis suggests. Regardless, the total albedo change due to the combined effect of surface and cloud albedo changes is a dominant driver of high-latitude warming. Interestingly, across the ensemble changes in oceanic and atmospheric energy flux convergence

tend to warm the southern high-latitudes and cool the northern high latitudes (there are of course exceptions, Figs. S2 & S3). Cloud longwave forcing are generally second order. Equatorward of ~60°N&S the warming signal is generally more uniform with the greenhouse effect term dominating as a function of CO_2 concentrations. With this uniformity in mind it is not surprising that while the tropics to high-latitude temperature difference generally scales as a function of global warming across the ensemble (Fig. 4b), the tropics to mid-latitude temperature difference only displays a weak sensitivity, with the exception of the NorESM (Fig. 4c).

Moving beyond the zonal-mean, the two-dimensional annual mean surface temperature changes for each of the Late and Middle to Early Miocene simulations, relative to their preindustrial control simulations, are shown in Supplementary Figs. S4 and S5 respectively. The limited impact of high-latitude glacial changes relative to CO_2 forcing on tropical warming is further illustrated when looking at the two-dimensional warming patterns stratified according to imposed CO_2 concentration (Fig. 6). The ensemble mean captures the average response to a given CO_2 concentration across a range of models and Miocene boundary conditions, and broadly indicates an increase in the degree of polar amplification with CO_2. When looking at the variability in warming for a given CO_2 range, the influence of the range of boundary conditions prescribed for the Antarctic Ice Sheet is most evident, giving rise to a substantial range in warming responses over the Antarctic continent. Particularly striking is the limited footprint of this variability. Other dominant sources of spread in the surface temperature response for a given CO_2 concentration include differences in continental warming. Hotspots like North Africa are presumably due to variability in vegetation changes, either prescribed or dynamic. While differences in prescribed orography may be more important in regions like Southern Asia.

Variability in ocean warming seen across the MioMIP ensemble, once stratified by CO_2 concentration, is muted relative to the spread in warming signals seen over the continents (Fig. 7, note the difference in the standard deviation (STD) colorbar range when compared to Fig. 6), but still substantial. There are several hotspots of large spread in the response seen across the models. Firstly, the spread across models in the degree of warming experienced in the Pacific cold tongue region (typically the central to south-eastern equatorial Pacific, but depending on model biases this can extend well into the western Pacific) is larger (STD between 2-4℃) than in the Indo-Pacific and eastern Pacific warm pool regions (STD < 2℃). This result indicates that for a given CO_2 forcing there is considerable spread across models in the warming of equatorial upwelling regions relative to the rest of the tropics, and hence in the zonal gradient response. This disagreement in the response of the tropical Pacific to warming across models is not unique to simulating the Miocene. There is considerable disagreement across CMIP models in the historical and projected response of the tropical Pacific (Kociuba and Power, 2015), due to complex and competing atmosphere-ocean interactions operating on a range of timescales (Heede et al., 2020). Other hotspots in the spread in the SST response include the subpolar gyres in the North Atlantic and Pacific basins and the Southern Ocean. Possible explanations for differing model responses in these regions include differing dynamical responses in wind-driven and thermohaline ocean circulation or regional cloud feedbacks. Alternatively, the model circulation responses might be dynamically similar but there are differences in the extent to which gyre boundaries have shifted.

Speaking specifically to the role of the spread in shortwave cloud feedbacks, Fig S7 confirms that the above-mentioned hotspots of variable SST responses do tend to correspond with hotspots of variable cloud albedo responses - clouds being the primary cause of TOA

albedo changes over ocean regions too warm for sea-ice (Fig. S7). There are several notable features in the model mean TOA albedo response stratified by CO_2 forcing. Firstly, the north-south dipole signature seen in the eastern equatorial Pacific for all CO_2 concentrations indicates a southward shift in convection and the ITCZ. Similarly, increased albedo in the central Pacific relative to the western Pacific Maritime continent region is indicative of an eastward expansion of tropical convection in the Pacific basin, with a similar westward expansion in the Indian Ocean, a feature consistent with the enhanced ensemble mean SST warming in these regions relative to the western Pacific (Fig. 7). Secondly, model mean TOA albedo decreases over the subtropical to mid-latitude ocean, more so at higher CO_2 levels (Fig. S7). This shortwave cloud feedback mechanism (Fig. 5) contributes to weaker midlatitude to tropical surface temperature gradients with higher CO_2, but as the model-data comparison results in the next section reveal this does not manifest in enough midlatitude warming to match reconstructed SSTs from these latitudes – with perhaps the exception of the Late Miocene NH at 560ppm. This in turn has implications for the ability of Miocene simulations to reproduce the reconstructed weakening of the meridional SST gradient between the tropics and the subtropics to mid-latitudes (Fig. 4c); and potentially the enhanced warming seen in the eastern equatorial Pacific sites following the ocean tunnel mechanism - whereby the ocean wind driven subtropical cells communicate subtropical warming signals to equatorial upwelling regions (Fedorov et al., 2015; Erfani and Burls, 2019). Thirdly, Southern Ocean TOA albedo increases poleward of ~50S, a feature seen in future projections associated with a southward shift in the storm tracks (Ceppi et al., 2014; Shaw et al., 2016). Finally, reductions in both land and sea ice lead to model mean TOA albedo decreases in both the NH and SH high latitudes, with variability in the prescribed extent of ice sheets leading to the large STDs seen over both Antarctica and Greenland (Fig. S7).

Sensitivity tests to differences in astronomical parameters were performed with two models in the MioMIP ensemble (Fig. 8). Compared with the sensitivity to other uncertain boundary conditions these results show important, yet relatively small (comparing Fig. 8 with Fig. 6), and regional, surface temperature sensitivity to changes in orbit. Simulations with differences in atmospheric CO_2 and Antarctic Ice Sheet extent show an increasing sensitivity to astronomical forcing with decreasing CO_2 and with decreasing ice sheet extent (Fig. S6). The sensitivity to CO_2 is likely linked to sea ice extent. There is minimal sea ice in the high atmospheric CO_2 simulations, and with lower atmospheric CO_2 the sea ice extent increases as does the variability in sea ice area between simulations with different astronomical boundary conditions. Similarly, in the absence of an Antarctic Ice Sheet there is greater variability in the Antarctic land surface albedo and increased sensitivity to changes in orbit. It is worth noting that orbital variability during the Miocene likely would have been accompanied by some sort of CO_2 variability (as in the Quaternary), and therefore the magnitude of orbitally-induced climate change modelled here is a minimum estimate.

4.3 Model-Data Comparison

Starting with the Late Miocene, Figs. 9 & 10 compare the simulated zonal-mean land and sea surface temperature profiles for all the experiments targeting the Late Miocene against available proxy data estimates. The experiments are again stratified by CO_2 forcing. Both the terrestrial and SST records indicate a reduced meridional surface temperature gradient (Figs. 9 & 10). Generally speaking, subtropical to midlatitude warmth tends to fall into better alignment with the proxy data as CO_2 levels increase. For the Northern Hemisphere, the NorESM-L simulation with 10Ma boundary conditions and 560ppm of CO_2 appears to provide a reasonable

fit from a zonal mean SST perspective (Fig. 10), but there are however large zonal asymmetries such that midlatitude SSTs are too warm in the Pacific basin, yet too cold in the Atlantic (Fig. 13e & S9). Although still falling short of the proxy estimate, this experiment simulates one of the strongest relaxations of the meridional temperature gradients (Fig. 4) with only a few degrees of tropical warming, between ~4 to 8℃ of subtropical warming, and significant high latitude warming, exceeding well over 20℃ in the Antarctic. It also provides one of the best fits with the terrestrial data (Fig. 9). With Late Miocene CO_2 estimates spanning ~300-450ppm (Fig. 1), one might expect the experiments forced with 350-450ppm of atmospheric CO_2 to provide the best fit with that data. When looking at the mean SST bias across simulations (Fig. 13) the root-mean-square-error (RMSE) is lowest for 560ppm (Fig. 13e). That said, there is still the general indication that the deep tropics are warming too much while the mid- to high-latitudes are too cold (Fig. 13c). It also appears that the zonal gradient in the equatorial Pacific is generally too strong in the models with not enough warming the eastern Pacific cold tongue region and too much warming in the western Pacific (Fig. 13c). From the perspective of the terrestrial MAT proxies the 560ppm Late Miocene simulation leads to the lowest RMSE (Fig. 13f).

Moving on to the Middle Miocene, both the terrestrial and SST proxies point to a further weakening of the meridional surface temperature gradient with a strikingly flat temperature gradient between the tropics and the subtropics to midlatitudes (Figs. 4c, 11 & 12). Increasing CO_2 levels brings extra-tropical warmth into better alignment with the proxy data but the models still fall short (Figs. 11 & 12), particularly on the regional scale e.g. cold SST biases persist in the North Atlantic and Southern Ocean even at 850ppm (Fig. 14g). Both the tropical Middle Miocene SST proxies and the tropical Middle Miocene terrestrial proxies indicate that 850ppm of CO_2 leads to too much tropical warming (Figs. 14g & h). That said all the simulations with lower CO_2 concentrations generally suffer from cold biases everywhere outside of the tropics (Figs. 14 & S11), supporting the conclusion that the models are generally failing to capture the weakening of meridional surface temperature gradients and the full extent of Middle Miocene warmth seen in the proxy data (Fig. 4). This finding holds and intensifies when one narrows the data window to the MCO (Fig. S12).

5 Conclusions

In this study, we have brought together a suite of Miocene climate simulations performed with a range of climate models and Late to Early Miocene boundary conditions. Serving as a first pass of this multi-model ensemble dataset, the focus has been placed on surface warming, specifically the spread and sensitivity of warming responses to the range of boundary conditions imposed across the ensemble. Furthermore, a model-data comparison has been performed to assess the fidelity with which the ensemble is capturing large-scale Miocene warming patterns over both land and ocean, and to develop insight into how high CO_2 concentrations need to be

from a modelling perspective to reproduce the broad warming patterns, specifically the weak meridional temperature gradient patterns seen in the data.

Summarizing first the key features emanating from our analysis of the global-mean, zonal-mean and 2-dimensional surface warming seen across the ensemble:

- Prescribed CO_2 forcing is the primary boundary condition controlling the global mean temperature change relative to preindustrial across the Miocene simulations analyzed.
- On average, Miocene boundary conditions other than CO_2 raise global mean temperature by just under 2℃
- Reconstructed global mean surface temperature estimates range from 19.30℃ +/- 0.98 to 21.95℃ +/- 0.81 for the Late Miocene, from 21.21℃ +/- 0.56 to 24.46℃ +/- 0.81, and from 22.93℃ +/- 1.01 to 25.47℃ +/- 1.17 depending on the type of surface temperature proxy informing the estimate.
- While some Miocene simulations with >=400ppm CO_2 forcing overlap with the minimum bound of the reconstructed global mean surface temperature estimates for their target Miocene interval, they generally fail to capture the reconstructed warming pattern. No combination of model and boundary condition choices to date satisfactorily simulates Miocene climate.
- A stronger polar greenhouse effect and decreased surface albedo are the dominant contributors to the polar amplified warming.
- Strong regional warming is seen in the response to prescribed changes in the Antarctic Ice Sheet but the influence beyond the Southern Hemisphere high latitudes is limited.
- The degree of polar amplified warming and weakening of the meridional temperature gradient increases with prescribed CO_2 forcing, but generally falls short of the reconstructed meridional gradient weakening seen in the proxies.
- “Hot spots” in which the SST response within a narrow range of CO_2 forcings is particularly variable across models include the eastern equatorial upwelling regions, the subpolar gyres and the Southern Ocean, and appear to be linked to the spread in cloud albedo and ocean responses over these regions.
- Simulations with perturbed orbital parameters show important, yet relatively small and regional, surface temperature sensitivity with an increased sensitivity to orbital changes as CO_2 concentrations or the extent of the Antarctic Ice Sheet decrease.

The extent to which the Miocene surface temperatures within the ensemble align with available terrestrial and sea surface temperature reconstructions has been assessed. Broadly speaking the low meridional temperature gradient indicated by the proxies, specifically between the mid-latitudes and tropics, is difficult to reconcile with the simulations. Under Miocene-like CO_2 forcing (the 350-450 ppm experiments), the modelled climates still retain relatively large equator-to-pole temperature gradients, especially in the Northern Hemisphere. The models do not exhibit the estimated 5-10℃ warming of the high latitudes with these CO_2 levels. In practice this means that in order to produce realistic warming of the northern high-latitudes, the models require higher CO_2. Increasing CO_2 forcing leads to enhanced warming bringing the midlatitudes into better alignments with the data, but this in turn leads to overshooting in the tropics which become too warm. This pattern is surprisingly robust across the both the Late Miocene, Middle Miocene and MOC datasets, as well as the independent terrestrial and ocean datasets. Achieving

the low meridional temperature gradient recorded in the Miocene thus remains an outstanding problem for most models.

That said, the latest generation of climate models with state-of-the-art parameterizations of cloud microphysics and cloud-aerosol interactions tend to support more positive cloud radiative feedbacks of the midlatitude oceans (Zhu et al., 2019, Lunt et al., 2020, Zhu and Poulsen, 2019). In addition, changes in aerosols may also be important as seen for the Eocene (Lunt et al, 2020) and Pliocene (Feng et al., 2019; Sagoo and Storelovmo, 2017). These model improvements may lead to enhanced midlatitude warming at lower CO_2 concentrations, but how they will then fare at simulating tropical Miocene warmth and the reduced meridional temperature gradient remains to be evaluated. More idealized sensitivity studies have revealed that both the meridional and the zonal equatorial Pacific SST gradients scale with the meridional gradient in cloud radiative forcing (specifically cloud albedo, Burls and Fedorov, 2014; Erfani and Burls, 2019), and provide a plausible mechanism for maintaining Early Pliocene SST patterns (Burls and Fedorov, 2014; Fedorov et al. 2015) and the hydrological cycle response (Burls and Fedorov, 2017).

The model ensemble we have used here was an 'post-hoc' model intercomparison using different boundary conditions and forcings for each model. Although we can still group the models into two time frames (Middle and Late Miocene) and into different CO_2 forcing ranges, it is impossible to cleanly assess how much of the inter-model spread can be attributed to differences in boundary conditions versus model feedback strengths. In particular, even if we could assign one simulation as a good match with the proxies, the reasons for this better match would not necessarily be clear. Therefore, in order to more rigorously test the models' ability to simulate Miocene warmth, meridional gradients and other features such as ocean circulation, cloud feedbacks, land surface behavior, and the hydrological cycle, carrying out a formal MIP is desirable.

The current study can guide a discussion on the careful design of the boundary conditions and model configurations to be used in such a formal model intercomparison.

I. In terms of paleogeography, the modelling groups participating in a formal MIP should use the same configuration for each model, and specific time slices (e.g. the MCO) should be chosen.

II. Sensitivity studies isolating the impact of gateway changes can then be encouraged by providing alternative continental geometries exploring different depths and widths of gateways based on minimum/maximum estimates from plate tectonic reconstructions. Key gateways to be investigated include the Central American Seaway, the Tethys Seaway, the Indoneisan Seaway, the Fram Strait as well as the Greenland-Scotland Ridge. More detailed discussions about these gateway conditions can be found in He et al., (this issue) and Brierley and Fedorov (2016) .

III. Models should be grouped into those with static or dynamic vegetation, and all models with static vegetation should use the same static vegetation distributions. Using a dynamic vegetation model is optimal as this allows for more direct

comparison with vegetation cover indicated by the fossil flora record e.g. Hernot et al. (2017)

IV. A common set of prescribed ice sheet boundary conditions that sample the uncertainty in reconstructed estimate should be used.

V. Ideally all models would treat aerosols in the same way, but if this is not feasible, differences should at least be well-documented (e.g. the PlioMIP2 protocol, Haywood et al, 2016; and DeepMIP protocol, Lunt et al, 2017)

VI. Finally, simulation should be run with a set of CO_2 concentrations that span the spread of uncertainty within Miocene CO_2 reconstructions. With the "best estimate" CO_2 concentration specified for when modelling groups can only carry out one simulation.

While a coordinated Miocene model intercomparison effort is an aspiration within the Miocene community, the analysis of the informal multi-model ensemble presented here has focused only on annual mean surface temperature and albedo responses and there remain several other aspects within this valuable dataset for investigation in future work e.g. the hydrological cycle, subsurface ocean temperature and circulation, differences in seasonality etc. We hope that the synthesis presented here will serve as a valuable starting point.

Acknowledgments, and Data Availability

NJB is supported by the National Science Foundation (NSF; AGS-1844380 and OCN-2002448), as well as the Alfred P. Sloan Foundation as a Research Fellow. AdB acknowledges support of the Swedish Research Council Project 2016-03912. AvdH acknowledges support by the program of the Netherlands Earth System Science Centre (NESSC), financially supported by the Ministry of Education, Culture and Science (OCW) (Grantnr. 024.002.001). DKH acknowledges the support of FORMAS grant 2018-01621. CDB acknowledges NERC grant NE I006281/1 and a NERC PhD studentship. CHL acknowledges NERC grant NE/P019102/1. DJL and AF acknowledge NERC grant NE/K014757/1. MH and NH acknowledge funding from the NSF P2C2 program for this project through grant #1602905. EG acknowledges funding from the Royal Society and NERC grant NE/T007397/1. We thank S. Sosdian, S. Modestou, and F. Sangiorgi for assistance in compiling the ocean temperature data.

The new synthesis of terrestrial MATs generated here for the Middle Miocene can be found in the supplementary material of this paper (additional excel file Table S1). As described in the Methods section of the paper, the Late, Middle and MCO SST estimates where compiled using published dataset, a summary of these datasets with links to their repositories has been complied in the supplementary material, together with the average estimates derived from each dataset for each time period (additional excel file Table S2). These Table S1 and S2 excel files have been archived in the Zenodo repository (*These files are temporarily available in the following google folder for the reviewers, on acceptance this link will be replaced with a Zenodo doi*) together with netcdf files containing the updated Herold et al. 2011a Middle Miocene paleogeography and land surface datasets described in the supplementary information, and a netcdf file containing the MioMIP variables used to make all the figures shown. A description of each model's setup is provided in the methods section of this paper, together with the relevant configuration information and reference to the original modelling study in Tables 1 & 2.

References

Akgün, F., Kayseri, M.S., & Akkiraz, M.S., 2007. Palaeoclimatic evolution and vegetational changes during the Late Oligocene-Miocene period in Western and Central Anatolia (Turkey). *Palaeogeography, Palaeoclimatology, Palaeoecology* 253, 56-90

Akgün, F., & Akyol, E., 1999. Palynostratigraphy ofthe coal-bearing Neogene deposits graben in Büyük Menderes Western Anatolia. *Geobios*, 32, 367-383

Anand, P., H. Elderfield, and M. H. Conte, 2003. Calibration of Mg/Ca thermometry in planktonic foraminifera from a sediment trap time series, *Paleoceanography*, *18*(2).

Aumont, O., Ethé, C., Tagliabue, A., Bopp, L., & Gehlen, M. 2015. PISCES-v2: an ocean biogeochemical model for carbon and ecosystem studies. *Geosci. Model Dev.*, 8, 2465–2513

Axelrod, D.I., 2000. A Miocene (10-12Ma) Evergreen Laurel-Oak forest from Carmel Valley, California. *University of California Publications: Geological Sciences*, 145, 1-34

Axelrod, D.I., 1995. The Miocene Purple Mountain Flora of Western Nevada. *University of California Publications: Geological Sciences*, 139, 1-63

Bacmeister JT, Lauritzen PH, Dai A, & Truesdale JE, 2012. Assessing possible dynamical effects of condensate in high resolution climate simulations. *Geophysical Research Letters*, 39(4):L04806

Barrón, E., Rivas-Carballo, R., Postigo-Mijarra, J.M., Alcalde-Olivares, C., Vieira, M., Castro, L., Pais, J., & Valle-Hernández, M., 2010. The Cenozoic vegetation of the Iberian Peninsula: A synthesis. *Review of Palaeobotany and Palynology*, 162, 382-402

Bartoli, G., Sarnthein, M., Weinelt, M., Erlenkeuser, H., Garbe-Schönberg, D. & Lea, D.W., 2005. Final closure of Panama and the onset of northern hemisphere glaciation. *Earth and Planetary Science Letters*, 237(1-2), 33-44

Bentsen, M., Bethke, I., Debernard, J. B., Iversen, T., Kirkevåg, A., Seland, Ø., Drange, H., Roelandt, C., Seierstad, I. A., Hoose, C., & Kristjánsson, J. E., 2013. The Norwegian Earth System Model, NorESM1-M – Part 1: Description and basic evaluation of the physical climate. *Geosci. Model Dev.*, 6, 687–720

Bitz, C. M., Shell, K. M., Gent, P. R., Bailey, D., Danabasoglu, G., Armour, K. C., Holland, M. M., & Kiehl, J. T., 2012. Climate sensitivity of the community climate system model version 4, *Journal of Climate*, 25, 3053-3070, doi:10.1175/JCLI-D-11-00290.1.

Böhme, M., Bruch, A.A., & Selmeier, A., 2007. The reconstruction of Early and Middle Miocene climate and vegetation in Southern Germany as determined from the fossil wood flora. *Palaeogeography, Palaeoclimatology, Palaeoecology*, 253, 91-114

Bradshaw, C., Lunt, D., Flecker, R., Salzmann, U., Pound, M., Haywood, A. & Eronen, J., 2012. The relative roles of CO_2 and palaeogeography in determining late Miocene climate: results from a terrestrial model-data comparison. *Climate of the Past*, 8(2), 715-786

Bradshaw, C.D., Lunt, D.J., Flecker, R. & Davies-Barnard, T., 2015. Disentangling the roles of late Miocene palaeogeography and vegetation – Implications for climate sensitivity. *Palaeogeography, Palaeoclimatology, Palaeoecology*, 417, 17-34

Bretherton, C.S. & Park, S., 2009. A new moist turbulence parameterization in the Community Atmosphere Model. *Journal of Climate*, 22(12), 3422-3448

Bretherton, C.S., 2015. Insights into low-latitude cloud feedbacks from high-resolution models. *Phil. Trans. R. Soc. A*, 373: 20140415

Brierley, C.M., & Federov, A.V., 2016. Comparing the impacts of Miocene-Pliocene changes in inter-ocean gateways on climate: central American Seaway, Bering Strait, and Indonesia. *EPSL*, 444, 116-130.

Brovkin, V., T. Raddatz, C. Reick, M. Claussen & Gayler, 2009. Global biogeophysical interactions between forest and climate. *Geophys. Res. Lett.*, 36, L07405

Bruch, A., & Gabrielyan, I., 2002. Quantitative data of the Neogene climatic development in Armenia and Nakhichevan. *Acta Universitatis Carolinae Geologica*, 46, 41-48

Bruch, A.A., Uhl, D., & Mosbrugger, V., 2007. Miocene climate in Europe -- Patterns and evolution: A first synthesis of NECLIME. *Palaeogeography, Palaeoclimatology, Palaeoecology*, 253, 1-7

Burke, K. D. et al. 2018. Pliocene and Eocene provide best analogs for near-future climates. *Proceedings of the National Academy of Sciences,* 115, 13288–13293.

Burls, N. J., & Fedorov, A. V., 2017 . Wetter subtropics in a warmer world: Contrasting past and future hydrological cycles. *Proceedings of the National Academy of Sciences*, 114(49), 12888-12893

Burls, N. J., & Fedorov, A. V., 2014. Simulating Pliocene warmth and a permanent El Niño-like state: The role of cloud albedo. *Paleoceanography*, 29(10), 893–910 http://doi.org/10.1002/2014PA002644

Burls, N. J., & Fedorov, A. V., 2014. What Controls the Mean East–West Sea Surface Temperature Gradient in the Equatorial Pacific: The Role of Cloud Albedo. *Journal of Climate*, 27(7), 2757–2778. http://doi.org/10.1175/JCLI-D-13-00255.1

Burton, K.W., Ling, H.F. & O'Nions, R.K., 1997. Closure of the Central American Isthmus and its effect on deep-water formation in the North Atlantic. *Nature*, 386(6623), 382-385

Ceppi, P., Zelinka, M. D., & Hartmann, D. L., 2014. The response of the Southern Hemispheric eddy-driven jet to future changes in shortwave radiation in CMIP5. *Geophysical Research Letters*, 41(9), 3244-3250

Chandan, D. & Peltier, W. R. 2018. On the mechanisms of warming the mid-Pliocene and the inference of a hierarchy of climate sensitivities with relevance to the understanding of climate futures. *Clim Past,* 14, 825–856.

Chirilă, G., & Ţabără, D., 2010. Palynological study of the outcrop from the Ciofoaia Brook (Moldavian Platform) - palaeoclimatic and palaeoenvironmental implications. *Proceedings of the International Symposium Geology of Natural Systems* – Geo Iași 2010, 94-99

Chirilă, G., & Tabără, D., 2008. Palaeofloristic study of the Volhyian from Rasca (Moldavian Platform) - palaeoclimatic and palaeoenvironmental implications. *Acta Palaeontologica Romaniae*, 6, 29-42

Conte, M. H., Sicre, M. A., Ruhlemann, C., Weber, J. C., Schulte, S., Schulz-Bull, D., & Blanz, T., 2006. Global temperature calibration of the alkenone unsaturation index (Uk'_{37}) in surface waters and comparison with surface sediments. *Geochemistry Geophysics Geosystems*, *7*(1), doi:10.129/2005GC001054

Coxall, H. K., Huck, C. E., Huber, M., Lear, C. H., Legarda-Lisarri, A., O'Regan, M., et al. 2018. Export of nutrient rich Northern Component Water preceded early Oligocene Antarctic glaciation. *Nature Publishing Group*, 11(3), 190–196. http://doi.org/10.1038/s41561-018-0069-9

Cramer, B. S., K. G. Miller, P. J. Barrett, & J. D. Wright, 201. Late Cretaceous–Neogene trends in deep ocean temperature and continental ice volume: Reconciling records of benthic foraminiferal geochemistry (δ18O and Mg/Ca) with sea level history, *Journal of Geophysical Research: Oceans*, 116(C12), C12023

Deng, T., Hou, S., Wang, H., 2007. The Tunggurian Stage of the Continental Miocene in China. *Acta Geologica Sinica - English Edition*, 81, 709-721

Denk, T., Grimsson, F., & Kvacek, Z., 2005. The Miocene floras of Iceland and their significance for late cainozoic North Atlantic biogeography, *Botanical Journal of the Linnean Society*, 149(4), 369-417

Dolan, A. M., 2012. Modelling mid-Pliocene Climate and Ice Sheets, Ph. D. Thesis, University of Leeds.

Drury, A. J., Lee, G. P., Gray, W. R., Lyle, M., Westerhold, T., Shevenell, A. E., & John, C. M., 2018. Deciphering the State of the Late Miocene to Early Pliocene Equatorial Pacific. *Paleoceanography and Paleoclimatology*, 33(3), 246–263

Dufresne, J.-L., Foujols, M.-A., Denvil, S., Caubel, A., Marti, O., Aumont, O., Balkanski, Y., Bekki, S., Bellenger, H., Benshila, R., Bony, S., Bopp, L., Braconnot, P., Brockmann, P., Cadule, P., Cheruy, F., Codron, F., Cozic, A., Cugnet, D., & Vuichard, N., 2013. Climate change projections using the IPSL-CM5 Earth System Model: from CMIP3 to CMIP5.

Climate Dynamics, 40(9–10), 2123–2165

Dunn, R.E., Strömberg, C.A.E., Madden, R.H., Kohn, M.J., & Carlini, A.A., 2015. Linked canopy, climate, and faunal change in the Cenozoic of Patagonia. *Science*, 347, 258-261

Eaton, B., 2010. User's Guide to the Community Atmosphere Model CAM-4.0. http://www.cesm.ucar.edu/models/ccsm4.0/cam/docs/users_guide/ug.html

Ehlers, B.-M., & Jokat, W., 2013. Paleo-bathymetry of the northern North Atlantic and consequences for the opening of the Fram Strait. *Marine Geophysical Research*, 34(1), 25–43

Emeis, K.-C., Struck, U., Schulz, H.-M., Rosenberg, R., Bernasconi, S., Erlenkeuser, H., et al., 2000. Temperature and salinity variations of Mediterranean Sea surface waters over the last 16,000 years from records of planktonic stable oxygen isotopes and alkenone unsaturation ratios. Palaeogeography, Palaeoclimatology, *Palaeoecology*, 158(3), 259–280

Emeis, K.-C., Schulz, H., Struck, U., Rossignol-Strick, M., Erlenkeuser, H., Howell, M. W., et al., 2003. Eastern Mediterranean surface water temperatures and $\delta^{18}O$ composition during deposition of sapropels in the late Quaternary. *Paleoceanography*, 18(1). https://doi.org/10.1029/2000PA000617

Erfani, E., & Burls, N. J., 2019. The Strength of Low-Cloud Feedbacks and Tropical Climate: A CESM Sensitivity Study. *Journal of Climate*, 32(9), 2497–2516

Erdei, B., Hably, L., Kázmér, M., Utescher, T., & Bruch, A.A., 2007. Neogene flora and vegetation development of the Pannonian domain in relation to palaeoclimate and palaeogeography. *Palaeogeography, Palaeoclimatology, Palaeoecology*, 253, 115-140

Etminan, M., Myhre, G., Highwood, E. J. and Shine, K. P. 2016. Radiative forcing of carbon dioxide, methane, and nitrous oxide: a significant revision of the methane radiative forcing. *Geophysical Research Letters*, 43 (24). 12614-12623. ISSN 0094-8276

Farnsworth, A., Lunt, D. J., O'Brien, C., Foster, G. L., Inglis, G. N., Markwick, P., Pancost. R.D. & Robinson, S. A., 2019a. Climate sensitivity on geological timescales controlled by non-linear feedbacks and ocean circulation. Geophysical Research Letters, 46, 9880–9889

Farnsworth, A., Lunt, D., Robinson, S., Valdes, P., Roberts, W., Clift, P., Markwick, P., Su, T., Wrobel, N., Bragg, F., Kelland, S.-J., & Pancost, R. 2019b. Past East Asian monsoon evolution controlled by palaeogeography, not CO_2. *Science Advances*, 5(10), eaax1697

Fedorov, A. V., Burls, N. J., Lawrence, K. T., & Peterson, L. C., 2015. Tightly linked zonal and meridional sea surface temperature gradients over the past five million years. *Nature Geoscience*, 8(12), 975-980

Feng, R. et al., 2017. Amplified Late Pliocene terrestrial warmth in northern high latitudes from greater radiative forcing and closed Arctic Ocean gateways. *Earth and Planetary Science Letters* 466, 129–138

Feng, R., Otto-Bliesner, B. L., Xu, Y., Brady, E., Fletcher, T., & Ballantyne, A. 2019. Contributions of aerosol-cloud interactions to mid-Piacenzian seasonally sea ice-free Arctic Ocean. Geophysical Research Letters, 46. https://doi.org/10.1029/2019GL083960

Ferguson, D.K., Pingen, M., Zetter, R., & Hofmann, C.-C., 1998. Advances in our knowledge of the Miocene plant assemblage from Kreuzau, Germany. *Review of Palaeobotany and Palynology*, 101, 147-177

Figueiral, I., Mosbrugger, V., Rowe, N.P., Utescher, T., Jones, T.P., Fritz Von Der, H., 2002. Role of Charcoal Analysis for Interpreting Vegetation Change and Paleoclimate in the Miocene Rhine Embayment (Germany). *PALAIOS*, 17, 347-365

Foster, G. L., Royer, D. L., & Lunt, D. J. 2017. Future climate forcing potentially without precedent in the last 420 million years. *Nature Communications*, 8, 14845

Foster, GL et al., 2012. The evolution of pCO2, ice volume and climate during the middle Miocene. *Earth and Planetary Science Letters*, 341-344, 243-254

Frederiksen, N.O., 1984. Stratigraphic, paleoclimatic and paleobiogeographic significance of Tertiary sporomorphs from Massachusetts. U.S. Geological Survey Professional Paper 1308, 1-25

Fretwell, P., et al., 2012. Bedmap2: improved ice bed, surface and thickness datasets for Antarctica, *The Cryosphere Discuss*., 6(5), 4305-4361

Frigola, A., Prange, M., & Schulz, M., 2018. Boundary conditions for the Middle Miocene Climate Transition (MMCT v1. 0). *Geosci-Model-Dev.*, 11, 1607-1626

Gasson, E., DeConto, R. M., Pollard, D., & Levy, R. H., 2016. Dynamic Antarctic ice sheet during the early to mid-Miocene. *Proceedings of the National Academy of Sciences*, 113(13), 3459–3464. http://doi.org/10.1073/pnas.1516130113

Gent, P. R., Danabasoglu, G., Donner, L. J., Holland, M. M., Hunke, E. C., Jayne, S. R., Lawrence, D. M., Neale, R. B., Rasch, P. J., Vertenstein, M., Worley, P. H., Yang, Z.-L., & Zhang, M., 2012. The Community Climate System Model Version 4, *Journal of Climate*, 24, 4973-4991, doi:10.1175/2011JCLI4083.1

Gettelman, A., Liu, X., Ghan, S., Morrison, H., Park, S., Conley, A., Klein, S., Boyle, J., Mitchell, D., & Li, J., 2010. Global simulations of ice nucleation and ice supersaturation with an improved cloud scheme in the community atmosphere model. *Journal of Geophysical Research*, 115(D18), D18216

Gettelman, A., Morrison, H., & Ghan, S., 2008. A new two-moment bulk stratiform cloud microphysics scheme in the community atmosphere model, version 3 (cam3). part ii: Single-column and global results. *Journal of Climate*, 21(15), 3660–3679.

Gettelman, A., Morrison, H., Santos, S., Bogenschutz, P., & Caldwell, P. M., 2015. Advanced Two-Moment Bulk Microphysics for Global Models. Part II: Global Model Solutions and Aerosol-Cloud Interactions. *Journal of Climate*, 28, 1288-1307.

Gnibidenko, Z.N., Martynov, V.A., Nikitin, V.P., & Semakov, N.N., 1999. Magnetostratigraphic and paleobotanical description of the Miocene deposits in the Beshcheul Horizon of West Siberia. *Russian Geology and Geophysics*, 40, 1776-1788

Goldner, A., Herold, N. & Huber, M., 2014. The Challenge of Simulating the Warmth of the Mid-Miocene Climatic Optimum in CESM1. Climate of the Past, 10(2), 523-536

Goldner, A., Huber, M., & Caballero, R. 2013, Does Antarctic glaciation cool the world? *Clim. Past*, 9, 173-189

Gough, D.O., 1981. Solar interior structure and luminosity variations. Sol. Phys. v.74, 21–34

Graham, A., Gregory-Wodzicki, K.M., & Wright, K.L., 2001. Studies in neotropical paleobotany. XA Mio-Pliocene palynoflora from the Eastern Cordillera, Bolivia: implications for the uplift history of the Central Andes. *American Journal of Botany*, 88, 1545-1557

Gray, W. R., and Evans D., 2019. Nonthermal Influences on Mg/Ca in Planktonic Foraminifera: A Review of Culture Studies and Application to the Last Glacial Maximum, *Paleoceanography and Paleoclimatology*, *34*(3), 306-315

Gregory-Wodzicki, K.M., McIntosh, W.C., & Velasquez, K., 1998. Climatic and tectonic implications of the late Miocene Jakokkota flora, Bolivian Altiplano. *Journal of South American Earth Sciences*, 11, 533-560

Grímsson, F., Denk, T. & Símonarson L. A., 2007. Middle Miocene floras of Iceland -- the early colonization of an island?, *Review of Palaeobotany and Palynology*, 144(3-4), 181-219

Guitián, J., Phelps, S., Polissar, P. J., Ausín, B., Eglinton, T. I., & Stoll, H. M., 2019. Midlatitude Temperature Variations in the Oligocene to Early Miocene. *Paleoceanography and Paleoclimatology*, 34(8), 1328–1343. https://doi.org/10.1029/2019PA003638

Hall, R., 2012. Sundaland and Wallacea: geology, plate tectonics and palaeogeography, in: Biotic Evolution and Environmental Change in Southeast Asia, edited by: Gower, D. J., Richardson, J. E., Rosen, B. R., Rueber, L., and Williams, S. T., Cambridge University Press, 32–78

Hansen, J., Sato, M., Russell, G. & Kharecha, P., 2013: Climate sensitivity, sea level and atmospheric carbon dioxide. *Philosophical Transactions of the Royal Society A: Mathematical, Physical and Engineering Sciences* 371, 20120294–20120294.

Hargreaves, J. C. & Annan, J. D. 2016. Could the Pliocene constrain the equilibrium climate sensitivity? *Clim Past*, 12, 1591–1599.

Hartley, A. 2003. Andean uplift and climate change, *Journal of the Geological Society*, 160(1), 7-10

Haug, G. H., & Tiedemann, R., 1998. Effect of the formation of the Isthmus of Panama on Atlantic Ocean thermohaline circulation. *Nature*, *393*(6686), 673–676. http://doi.org/10.1038/31447

Haywood, A. M., Tindall, J. C., Dowsett, H. J., Dolan, A. M., Foley, K. M., Hunter, S. J., Hill, D. J., Chan, W.-L., Abe-Ouchi, A., Stepanek, C., Lohmann, G., Chandan, D., Peltier, W. R., Tan, N., Contoux, C., Ramstein, G., Li, X., Zhang, Z., Guo, C., Nisancioglu, K. H., Zhang, Q., Li, Q., Kamae, Y., Chandler, M. A., Sohl, L. E., Otto-Bliesner, B. L., Feng, R., Brady, E. C., von der Heydt, A. S., Baatsen, M. L. J., & Lunt, D. J., 2020. A return to large-scale features of Pliocene climate: the Pliocene Model Intercomparison Project Phase 2, *Clim. Past Discuss.*, https://doi.org/10.5194/cp-2019-145

Haywood, A. M., Dowsett, H. J., Dolan, A. M., Rowley, D., Abe-Ouchi, A., Otto-Bliesner, B. L., Chandler, M. A., Hunter, S. J., Lunt, D. J., Pound, M. & Salzmann, U., 2016. The Pliocene Model Intercomparison Project (PlioMIP) Phase 2: scientific objectives and experimental design. *Climate of the Past*, 12(3), 663–675. http://doi.org/10.5194/cp-12-663-2016.

Haywood, A. M. et al. 2013. Large-scale features of Pliocene climate: results from the Pliocene Model Intercomparison Project. *Climate of the Past*, 9, 191–209

Haywood, A.M., Dowsett H.J., Robinson M.M., Stoll D.K., Dolan A.M., Lunt D.J., Otto-Bliesner B., and Chandler M.A. 2011. Pliocene Model Intercomparison Project (PlioMIP): experimental design and boundary conditions (Experiment 2). *Geoscientific Model Development*, 4, 571-577.

Heede, U. K., Fedorov, A. V., & Burls, N. J., 2020., Timescales and mechanisms for the Tropical Pacific response to global warming: a tug of war between the Ocean Thermostat and weaker Walker. Journal of Climate, JCLI–D–19–0690.1. http://doi.org/10.1175/JCLI-D-19-0690.1

Heinemann, M., Jungclaus, J. H., and Marotzke, J. 2009. Warm Paleocene/Eocene climate as simulated in ECHAM5/MPI-OM, *Clim. Past*, 5, 785–802, doi:10.5194/cp-5-785-2009

Herbert, T. D., Peterson, L. C., Lawrence, K. T., & Liu, Z., 2010. Tropical Ocean Temperatures Over the Past 3.5 Myr. *Science*, 328, 1530–1534. https://doi.org/10.1126/science.1185435

Herbert, T. D., Lawrence, K. T., Tzanova, A., Peterson, L. C., Caballero-Gill, R., & Kelly, C. S., 2016. Late Miocene global cooling and the rise of modern ecosystems. Nature Geoscience, v.9(11) , 843-847

Herbert, T. D., Ng, G., & Peterson, L. C., 2015. Evolution of Mediterranean sea surface temperatures 3.5–1.5 Ma: Regional and hemispheric influences. *Earth and Planetary Science Letters*, 409, 307–318. https://doi.org/10.1016/j.epsl.2014.10.006

Henrot, A. J. et al. 2017. Middle Miocene climate and vegetation models and their validation with proxy data. *Palaeogeography, Palaeoclimatology, Palaeoecology,* 467, 95–119

Herold, N., Seton, M., Müller, R. D., You, Y., & Huber, M., 2008. Middle Miocene tectonic boundary conditions for use in climate models. Geochemistry, Geophysics, Geosystems, 9(10), Q10009

Herold, N., Müller, R. D., & Seton, M., 2010. Comparing early to middle Miocene terrestrial climate simulations with geological data, *Geosphere*, 6, 952-961.

Herold, N., Huber, M., & Müller, R. D., 2011a. Modeling the Miocene Climatic Optimum. Part I: Land and Atmosphere, *Journal of Climate*, 24, 6353–6372, doi:10.1029/2010PA002041

Herold, N., Huber, M., Greenwood, D. R., Müller, R. D., & Seton, M., 2011b. Early to middle Miocene monsoon climate in Australia. *Geology*, 39(1), 3-6

Herold, N., Huber, M., Müller, R. D., & Seton, M., 2012. Modeling the Miocene climatic optimum: Ocean circulation, *Paleoceanography*, 27, PA1209, doi:10.1029/2010PA002041

Hill, D. J. et al. 2014. Evaluating the dominant components of warming in Pliocene climate simulations. *Clim Past,* 10, 79–90

Hobbs, K.M., Parrish, J.T., 2016. Miocene global change recorded in Columbia River basalt–hosted paleosols. *GSA Bulletin*, 128, 1543-1554

Holbourn, A., Kuhnt, W., Regenberg, M., Schulz, M., Mix, A., & Andersen, N., 2010. Does Antarctic glaciation force migration of the tropical rain belt? *Geology*, 38(9), 783–786 https://doi.org/10.1130/G31043.1

Holbourn, A. E., Kuhnt, W., Clemens, S. C., Kochhann, K. G. D., Jöhnck, J., Lübbers, J., & Andersen, N., 2018. Late Miocene climate cooling and intensification of southeast Asian winter monsoon. *Nature Communications*, 9(1), 1584. https://doi.org/10.1038/s41467-018-03950-1

Holdgate, G.R., Cartwright, I., Blackburn, D.T., Wallace, M.W., Gallagher, S.J., Wagstaff, B.E., Chung, L., 2007. The Middle Miocene Yallourn coal seam -- The last coal in Australia. *International Journal of Coal Geology*, 70, 95-115

Holland, K et al., 2020. Constraining multiple controls on planktic foraminifera Mg/Ca. *Geochimica et Cosmochimica Acta*, 273, 116-136, https://doi.org/10.1016/j.gca.2020.01.015.

Hollis, C. J., Dunkley Jones, T., Anagnostou, E., Bijl, P. K., Cramwinckel, M. J., Cui, Y., Dickens, G. R., Edgar, K. M., Eley, Y., Evans, D., Foster, G. L., Frieling, J., Inglis, G. N., Kennedy, E. M., Kozdon, R., Lauretano, V., Lear, C. H., Littler, K., Lourens, L., Meckler, A. N., Naafs, B. D. A., Pälike, H., Pancost, R. D., Pearson, P. N., Röhl, U., Royer, D. L., Salzmann, U., Schubert, B. A., Seebeck, H., Sluijs, A., Speijer, R. P., Stassen, P., Tierney, J., Tripati, A., Wade, B., Westerhold, T., Witkowski, C., Zachos, J. C., Zhang, Y. G., Huber, M., & Lunt, D. J., 2019.

The DeepMIP contribution to PMIP4: methodologies for selection, compilation and analysis of latest Paleocene and early Eocene climate proxy data, incorporating version 0.1 of the DeepMIP database, *Geosci. Model Dev.*, 12, 3149–3206

Hoorn, C., et al., 2010. Amazonia Through Time: Andean Uplift, Climate Change, Landscape Evolution, and Biodiversity, *Science*, 330(6006), 927-931

Hourdin, F., Grandpeix, J.-Y., Rio, C., Bony, S., Jam, A., Cheruy, F., Rochetin, N., Fairhead, L., Idelkadi, A., Musat, I., Dufresne, J.-L., Lahellec, A., Lefebvre, M.-P., & Roehrig, R., 2013. LMDZ5B: the atmospheric component of the IPSL climate model with revisited parameterizations for clouds and convection. *Climate Dynamics*, 40(9–10), 2193–2222

Huang, X., Stärz, M., Gohl, K., Knorr, G. & Lohmann, G., 2017. Impact of Weddell Sea shelf progradation on Antarctic bottom water formation during the Miocene, *Paleoceanography*, 32, doi:10.1002/2016PA002987

Huang, Y., Clemens, S. C., Liu, W., Wang, Y., & Prell, W. L., 2007. Large-scale hydrological change drove the late Miocene C4 plant expansion in the Himalayan foreland and Arabian Peninsula. *Geology*, 35(6), 531–534. https://doi.org/doi: 10.1130/G23666A

Huber, M., & Caballero, R., 2011. The early Eocene equable climate problem revisited. *Climate of the Past*, 7(2), 603–633. http://doi.org/10.5194/cp-7-603-2011

Huber, M., & Sloan, L. C., 2001. Heat transport, deep waters, and thermal gradients: Coupled simulation of an Eocene greenhouse climate. *Geophysical Research Letters*, 28(18), 3481–3484.

Hui, Z., Zhang, J., Ma, Z., Li, X., Peng, T., Li, J., Wang, B., 2018. Global warming and rainfall: Lessons from an analysis of Mid-Miocene climate data. *Palaeogeography, Palaeoclimatology, Palaeoecology*, 512, 106-117

Hurrell J.W., Holland M.M., Gent P.R., Ghan S., Kay J.E., Kushner P.J., Lamarque J.F., Large W.G., Lawrence D., Lindsay K., & Lipscomb W.H., 2013. The community earth system model: a framework for collaborative research. *Bulletin of the American Meteorological Society*. 94(9), 1339-60

Hüsing, S. K., Zachariasse, W.-J., van Hinsbergen, D. J. J., Krijgsman, W., Inceöz, M., Harzhauser, M., Mandic, O. & Kroh, A., 2009. Oligocene–Miocene basin evolution in SE Anatolia, Turkey: constraints on the closure of the eastern Tethys gateway, *Geological Society, London, Special Publications*, 311(1), 107-132

Hutchinson, D. K., Coxall, H. K., O'Regan, M., Nilsson, J., Caballero, R., and de Boer, A. M., 2019. Arctic closure as a trigger for Atlantic overturning at the Eocene-Oligocene Transition, *Nature Communications*, 10, 3797

Iacono M. J., et al. 2008. Radiative forcing by long-lived greenhouse gases: Calculations with the AER radiative transfer models. *Journal of Geophysical Research: Atmospheres*, v.113(D13)

Inglis, G. N., Bragg, F., Burls, N., Evans, D., Foster, G. L., Huber, M., Lunt, D. J., Siler, N., Steinig, S., Wilkinson, R., Anagnostou, E., Cramwinckel, M., Hollis, C. J., Pancost R. D., & Tierney J. E., 2020. Global mean surface temperature and climate sensitivity of the EECO, PETM and latest Paleocene. *Climate of the Past Discussions*. http://doi.org/10.5194/cp-2019-167

Iturralde-Vinent, M. A., 2006. Meso-Cenozoic Caribbean Paleogeography: Implications for the Historical Biogeography of the Region, *International Geology Review*, 48(9), 791-827

Ivanov, D.A., Ashraf, A.R., & Mosbrugger, V., 2007. Late Oligocene and Miocene climate and vegetation in the Eastern Paratethys area (northeast Bulgaria), based on pollen data. *Palaeogeography, Palaeoclimatology, Palaeoecology*, 255, 342-360

Ivanov, D., Ashraf, A.R., Mosbrugger, V., Palamarev, E., 2002. Palynological evidence for Miocene climate change in the Forecarpathian Basin (Central Paratethys, NW Bulgaria). *Palaeogeography, Palaeoclimatology, Palaeoecology*, 178, 19-37

Jacobs, B.F., & Deino, A.L., 1996. Test of climate-leaf physiognomy regression models, their application to two Miocene floras from Kenya, and 40Ar/39Ar dating of the Late Miocene Kapturo site. *Palaeogeography, Palaeoclimatology, Palaeoecology*, 123, 259-271

Jarzen, D.M., Corbett, S.L., & Manchester, S.R., 2010. Palynology and paleoecology of the Middle Miocene Alum Bluff flora, Liberty County, Florida, USA. Palynology; Lott, T.A., Manchester, S.R., Corbett, S.L., 2019. The Miocene flora of Alum Bluff, Liberty County, Florida. *Acta Palaeobotanica*, 59, 75-129

Jiménez-Moreno, G., 2006. Progressive substitution of a subtropical forest for a temperate one during the middle Miocene climate cooling in Central Europe according to palynological data from cores Tengelic-2 and Hidas-53 (Pannonian Basin, Hungary). *Review of Palaeobotany and Palynology*, 142, 1-14

Jungclaus, J. H., Keenlyside, N., Botzet, M., Haak, H., Luo, J. J., Latif M., & Marotzke J., 2006. Ocean circulation and tropical variability in the coupled model ECHAM5/MPI-OM, *Journal of Climate,* 19, 3952–3972

Karami, M. P., 2011. Paleoceanography of the Miocene Mediterranean Sea and Paratethys: Regional ocean modelling of the response to closure of the Tethys Seaway, Utrecht.

Kayseri Özer, M.S., Sözbilir, H., & Akgün, F., 2014. Miocene palynoflora of the Kocaçay and Cumaovası basins: a contribution to the synthesis of Miocene palynology, palaeoclimate, and palaeovegetation in western Turkey. *Turkish Journal of Earth Sciences*, 23, 233-259

Kayseri, M.S., & Akgün, F., 2010. The Late Burdigalian-Langhian interval in Turkey and the palaeoenvironmental and palaeoclimatic implications and correlation of Europe and Turkey: Late Burdigalian-Langhian palynofloras and palaeoclimatic properties of the Muğla-Milas (Kultak). *Geological Bulletin of Turkey*, 53, 1-44

Kershaw, A.P., 1997. A Bioclimatic Analysis of Early to Middle Miocene Brown Coal Floras, Latrobe Valley, South-eastern Australia. Australian Journal of Botany 45, 373-387

Khan, M.A., Spicer, R.A., Bera, S., Ghosh, R., Yang, J., Spicer, T.E., Guo, S.X., Su, T., Jacques, F. and Grote, P.J., 2014. Miocene to Pleistocene floras and climate of the Eastern Himalayan Siwaliks, and new palaeoelevation estimates for the Namling–Oiyug Basin, Tibet. *Global and Planetary Change*, 113, 1-10

Kiehl, J. T., & Shields, C. A., 2013. Sensitivity of the Palaeocene-Eocene Thermal Maximum climate to cloud properties. *Philosophical Transactions of the Royal Society a: Mathematical, Physical and Engineering Sciences*, 371(2001), 20130093–20130093. http://doi.org/10.1098/rsta.2013.0093

Knorr, G., & Lohmann, G., 2014. Climate warming during Antarctic ice sheet expansion at the Middle Miocene transition. *Nature Geosciences*, 7(5), 376–381. http://doi.org/10.1038/ngeo2119

Knorr, G., Butzin, M., Micheels, A., & Lohmann, G., 2011. A warm Miocene climate at low atmospheric CO_2 levels. *Geophysical Research Letters*, 38(20), http://doi.org/10.1029/2011GL048873

Knorr, G, Butzin, M., Micheels, A., Lohmann, G., 2019. Late Miocene model boundary conditions. PANGAEA, https://doi.org/10.1594/PANGAEA.904264, Supplement to: Knorr, G et al. (2011): A warm Miocene climate at low atmospheric CO2 levels. *Geophysical Research Letters*, 38(20), https://doi.org/10.1029/2011GL048873.

Kociuba, G., & Power S. B., 2015. Inability of CMIP5 models to simulate recent strengthening of the Walker circulation: Implications for projections. *Journal of Climate*, 28 (1), 20–35

Kotthoff, U., Greenwood, D.R., McCarthy, F.M.G., Müller-Navarra, K., Prader, S., & Hesselbo, S.P., 2014. Late Eocene to middle Miocene (33 to 13 million years ago) vegetation and climate development on the North American Atlantic Coastal Plain (IODP Expedition 313, Site M0027). *Clim. Past*, 10, 1523-1539

Kováčová, M., Hohenegger, J., & Ćorić, S., 2009. Palaeovegetation and climate based on pollen analysis of the Baden-Sooss section (Middle Miocene, Vienna Basin, Austria). In: Filipescu, S. (Ed.), 3rd International Workshop Neogene of Central and South-Eastern Europe. *Cluj University Press, Cluj-Napoca*, 65-65

Krapp, M., & Jungclaus, J. H., 2011. The Middle Miocene climate as modelled in an atmosphere-ocean-biosphere model. *Climate of the Past*, 7, 1169-1188

Krinner, G., Viovy, N., de Noblet-Ducoudré, N., Ogée, J., Polcher, J., Friedlingstein, P., Ciais, P., Sitch, S., & Prentice, I. C., 2005. A dynamic global vegetation model for studies of the coupled atmosphere-biosphere system. *Global Biogeochemical Cycles*, 19(1). https://doi.org/10.1029/2003GB002199

Kutzbach, J. E., Prell, W. L., & Ruddiman, W. F., 1993. Sensitivity of Eurasian Climate to Surface Uplift of the Tibetan Plateau. *The Journal of Geology,* 101(2), 177–190. http://doi.org/10.1086/648215

Langford, R. P., Wilford, G. E., Truswell, E. M., & Isern, A. R., 1995. Palaeogeographic Atlas of Australia, *Australian Geological Survey Organisation*, Canberra, http://www.ga.gov.au/resources/multimedia/animation/palaeo/html/palaeo.html

LaRiviere, J. P., Ravelo, A. C., Crimmins, A., Dekens, P. S., Ford, H. L., Lyle, M., & Wara, M. W., 2012. Late Miocene decoupling of oceanic warmth and atmospheric carbon dioxide forcing. *Nature*, 486, 97–100. https://doi.org/doi:10.1038/nature11200

Larsson, L.M., Dybkjær, K., Rasmussen, E.S., Piasecki, S., Utescher, T., Vajda, V., 2011. Miocene climate evolution of northern Europe: A palynological investigation from Denmark. *Palaeogeography, Palaeoclimatology, Palaeoecology*, 309, 161-175

Lawrence, D. M., Oleson, K. W., Flanner, M. G., Fletcher, C. G., Lawrence, P. J., Levis, S., Swenson, S. C., & Bonan, G. B., 2012. The CCSM4 land simulation, 1850-2005: assessment of surface climate and new capabilities, *Journal of Climate*, 25, 2240-2260, doi:10.1175/JCLI-D-11-00103.1, 2012

Lawrence, K. T., Herbert, T. D., Dekens, P. S., & Ravelo, A. C., 2007. The application of the alkenone organic proxy to the study of Plio-Pleistocene climate. *Deep-Time Perspectives on Climate Change: Marrying the Signal from Computer Models and Biological*, 539-562.

Lawrence, K. T., 2006. Characterizing the Plio-Pleistocene Evolution of Sea Surface Conditions Using the Alkenone Organic Proxy (PhD). Brown University, Providence, RI

Lawrence, K. T., Herbert, T. D., Brown, C. M., Raymo, M. E., & Haywood, A. M., 2009. High-amplitude variations in North Atlantic sea surface temperature during the early Pliocene warm Period. *Paleoceanography*, 24, doi:10.1029/2008PA001669

Lear, C.H., Rosenthal, Y. & Wright, J.D., 2003. The closing of a seaway: ocean water masses and global climate change. *Earth and Planetary Science Letters*, 210(3-4), 425-436

Lear, C. H., Elderfield, H., & Wilson, P. A., 2000. Cenozoic deep-sea temperatures and global ice volumes from Mg/Ca in benthic foraminiferal calcite. *Science*, 287(5451), 269–272

Leopold, E.B., Liu, G., 1994. A long pollen sequence of Neogene age, Alaska Range. Quaternary International 22/23, 103-140; Grimaldi, D.A., Triplehorn, D.M., 2008. Insects from the Upper Miocene Grubstake Formation of Alaska. *American Museum novitates*, 3612, 1-19

Levy, R., Harwood, D., Florindo, F., Sangiorgi, F., Tripati, R., von Eynatten, H., et al., 2016. Antarctic ice sheet sensitivity to atmospheric CO_2 variations in the early to mid-Miocene. *Proceedings of the National Academy of Sciences*, 113(13), 3453–3458. https://doi.org/10.1073/pnas.1516030113

Liang, M.M., Bruch, A., Collinson, M., Mosbrugger, V., Li, C.S., Sun, Q.G. & Hilton, J., 2003. Testing the climatic estimates from different palaeobotanical methods: an example from the Middle Miocene Shanwang flora of China. *Palaeogeography, Palaeoclimatology, Palaeoecology*, 198(3-4), 279-301

Ling, H.F., Burton, K.W., O'nions, R.K., Kamber, B.S., von Blanckenburg, F., Gibb, A.J. & Hein, J.R., 1997. Evolution of Nd and Pb isotopes in Central Pacific seawater from ferromanganese crusts. *Earth and Planetary Science Letters*, 146(1-2), 1-12

Liu, Z., & Herbert, T. D., 2004. High-latitude influence on the eastern equatorial Pacific climate in the early Pleistocene epoch. *Nature*, 427, 720–723

Liu, G., & Leopold, E.B., 1994. Climatic comparison of Miocene pollen floras from northern East-China and south-central Alaska, USA. *Palaeogeography, Palaeoclimatology, Palaeoecology*, 108, 217-228

Liu, Y.-S., Utescher, T., Zhou, Z., Sun, B., 2011. The evolution of Miocene climates in North China: Preliminary results of quantitative reconstructions from plant fossil records. *Palaeogeography, Palaeoclimatology, Palaeoecology*, 304, 308-317

Lopes dos Santos, R. A., Prange M., Castañeda I. S., Schefuß E., Mulitza S., Schulz M., Niedermeyer, Sinninghe E. M., Damsté J. S., & Schouten S., 2010. Glacial-interglacial variability in Atlantic meridional overturning circulation and thermocline adjustments in the tropical North Atlantic. *Earth and Planetary Science Letters*, 300, 407-414

Lunt, D. J., Bragg, F., Chan, W.-L., Hutchinson, D. K., Ladant, J.-B., Niezgodzki, I., Steinig, S., Zhang, Z., Zhu, J., Abe-Ouchi, A., de Boer, A. M., Coxall, H. K., Donnadieu, Y., Knorr, G., Langebroek, P. M., Lohmann, G., Poulsen, C. J., Sepulchre, P., Tierney, J., Valdes, P. J., Dunkley Jones, T., Hollis, C. J., Huber, M., & Otto-Bliesner, B. L., 2020, DeepMIP: Model intercomparison of early Eocene climatic optimum (EECO) large-scale climate features and comparison with proxy data, *Clim. Past Discuss.*, https://doi.org/10.5194/cp-2019-149

Lunt, D. J., Huber, M., Anagnostou, E., Baatsen, M. L. J., Caballero, R., DeConto, R., Dijkstra, H. A., Donnadieu, Y., Evans, D., Feng, R., Foster, G. L., Gasson, E., von der Heydt, A. S., Hollis, C. J., Inglis, G. N., Jones, S. . M., Kiehl, J., Kirtland Turner, S., Korty, R. L., Kozdon, R., Krishnan, S., Ladant, J.-B., Langebroek, P., Lear, C. H., LeGrande, A. N., Littler, K., Markwick, P., Otto-Bliesner, B., Pearson, P., Poulsen, C. J., Salzmann, U., Shields, C., Snell, K., Stärz, M., Super, J., Tabor, C., Tierney, J. E., Tourte, G. J. L., Tripati, A., Upchurch, G. R., Wade, B. S., Wing, S. L., Winguth, A. M. E., Wright, N. M., Zachos, J. C., & Zeebe, R. E., et al., 2017. The DeepMIP contribution to PMIP4: experimental design for model simulations of the EECO, PETM, and pre-PETM (version 1.0). Geoscientific Model Development, 10(2), 889–901. http://doi.org/10.5194/gmd-10-889-2017

Lunt, D. J., Dunkley Jones, T., Heinemann, M., Huber, M., LeGrande, A., Winguth, A., et al., 2012. A model–data comparison for a multi-model ensemble of early Eocene atmosphere-ocean simulations: EoMIP. *Climate of the Past*, 8(5), 1717–1736. http://doi.org/10.5194/cp-8-1717-2012

Lunt, D.J., Valdes, P.J., Haywood, A. & Rutt, I.C., 2008. Closure of the Panama Seaway during the Pliocene: implications for climate and Northern Hemisphere glaciation. *Climate Dynamics*, 30(1), 1-18

Löwemark, L., Zheng, Y.-C., Das, S., Yeh, C.-P., Chen, T.-T., 2016. A peculiar reworking of Ophiomorpha shafts in the Miocene Nangang Formation, Taiwan. *Geodinamica Acta*, 28, 71-85

Ma, Y., 1991. Tertiary sporo-pollen assemblages from southern Dunhuang Basin, Gansu Province. Acta Micropalaeontologica Sinica 8, 207-225

Madec, G., & Imbard, M., 1996. A global ocean mesh to overcome the North Pole singularity. *Climate Dynamics*, 12(6), 381–388. https://doi.org/10.1007/BF00211684

Madec, G., 2008. NEMO ocean engine. Technical note, IPSL, available at http://www.nemo-ocean.eu/content/download/11245/56055/file/NEMO_book_v3_2.pdf

Maier-Reimer, E., Mikolajewicz, U. & Crowley, T., 1990. Ocean general circulation model sensitivity experiment with an open Central American Isthmus. *Paleoceanography*, 5(3), 349-366

Mao, X., Retallack, G., 2019. Late Miocene drying of central Australia. Palaeogeography, Palaeoclimatology, *Palaeoecology*, 514, 292-304

Markwick, P. J., 2007. Deep time perspectives on climate change: marrying the signal from computer models and biological proxies. In Williams, M., Haywood, A.M., Gregory, F.J., Schmidt, D.N. (Eds.), (chap. The palaeogeographic and palaeoclimatic significance of climate proxies for data-model comparisons). The Micropalaeontological Society Special Publications, Geological Society of London.

Marsland, S. J., Haak, H., Jungclaus, J. H., Latif M., & Röske F., 2003. The Max-Planck-Institute global ocean/sea ice model with orthogonal curvilinear coordinates. *Ocean Modelling,* 5, 91–127

Marzocchi, A., Lunt, D. J., Flecker, R., Bradshaw, C. D., Farnsworth, A., & Hilgen, F. J., 2015. Orbital control on late Miocene climate and the North African monsoon: insight from an ensemble of sub-precessional simulations, *Clim. Past*, 11, 1271-1295, doi:10.5194/cp-11-1271-2015

Marzocchi, A., Flecker, R., Lunt, D. J., Krijgsman, W., & Hilgen, F. J., 2019. Precessional drivers of late Miocene Mediterranean sedimentary sequences: African summer monsoon and Atlantic winter storm tracks. *Paleoceanography and Paleoclimatology*, 34, 1980–1994

McClymont, E. L. et al. 2020. Lessons from a high-CO2 world: an ocean view from ~3 million years ago. Clim Past 16, 1599–1615

Meulenkamp, J. E., & Sissingh W., 2003. Tertiary palaeogeography and tectonostratigraphic evolution of the Northern and Southern Peri-Tethys platforms and the intermediate domains of the African–Eurasian convergent plate boundary zone, *Palaeogeography, Palaeoclimatology, Palaeoecology*, 196(1–2), 209-228

Micheels, A., Bruch, A. A., Uhl, D., Utescher, T., & Mosbrugger V., 2007. A Late Miocene climate model simulation with ECHAM4/ML and its quantitative validation with terrestrial proxy data. *Palaeogeography Palaeoclimatology Palaeoecology,* 253, 267–286

Micheels, A., Bruch, A. A., Eronen, J., Fortelius, M., Harzhauser, M., Utescher, T., & Mosbrugger, V., 2011. Analysis of heat transport mechanisms from a Late Miocene model experiment with a fully-coupled atmosphere–ocean general circulation model. *Palaeogeography, Palaeoclimatology, Palaeoecology*, 304(3-4), 337–350. http://doi.org/10.1016/j.palaeo.2010.09.021

Mikolajewicz, U., Maier-Reimer, E., Crowley, T.J. & Kim, K.Y., 1993. Effect of Drake and Panamanian gateways on the circulation of an ocean model. *Paleoceanography*, 8(4), 409-426

Milovanovic, D., Mihajlovic, D., 1984. A Miocene flora from Zagubica basin, eastern Serbia. *Annales Geologiques de la Peninsule Balkanique*, 48, 201-213

Molnar, P. (2008), Closing of the Central American Seaway and the Ice Age: A critical review, *Paleoceanography*, 23(2), PA2201

Montes, C., Cardona, A., McFadden, R., Morón, S.E., Silva, C.A., Restrepo-Moreno, S., Ramírez, D.A., Hoyos, N., Wilson, J., Farris, D. & Bayona, G.A., 2012. Evidence for middle Eocene and younger land emergence in central Panama: Implications for Isthmus closure. GSA Bulletin, 124(5-6), 780-799

Morrison, H. & Gettelman, A., 2008. A new two-moment bulk stratiform cloud microphysics scheme in the community atmosphere model, version 3 (cam3). part i: Description and numerical tests. *Journal of Climate*, 21(15), 3642-3659

Mosbrugger, V., Utescher, T., Dilcher, D.L., 2005. Cenozoic continental climatic evolution of Central Europe. *Proceedings of the National Academy of Sciences of the United States of America*, 102, 14964-14969

Mosbrugger, & Utescher, T., 1997. The coexistence approach—a method for quantitative reconstructions of Tertiary terrestrial palaeoclimate data using plant fossils. *Palaeogeography, Palaeoclimatology, Palaeoecology*, 134(1-4), 61-86

Müller, R. D., Sdrolias, M., Gaina, C., & Roest, W. R., 2008a. Age, spreading rates, and spreading asymmetry of the world's ocean crust, *Geochem. Geophys. Geosyst.*, 9(4), Q04006.

Müller, R. D., M. Sdrolias, Gaina C., Steinberger B., & H. C., 2008b. Long-Term Sea-Level Fluctuations Driven by Ocean Basin Dynamics, *Science*, 319(5868), 1357-1362.

Müller, P. J., Kirst, G., Ruhland, G., von Storch, I. & Rosell-Melé, A., 1998. Calibration of the alkenone paleotemperature index Uk on core-tops from the eastern South Atlantic and the global ocean (60◦N–60◦S). *Geochem. Cosmochim. Acta*, 62, 1757–1772

Nagy, E., 2005. Palynological evidence for Neogene climatic change in Hungary. *Ocassional Papers of the Geological Institute of Hungary*, 205, 5-120

Neale, R.B., Richter, J., Park, S., Laurtizen, P., Vavrus, S.J., Rasch, P.J., & Zhang, M., 2013. The mean climate of the Community Atmosphere Model (CAM4) in forced SST and fully coupled experiments, *J. Clim.*, 26, 5150–5168

Neale R.B. & Coauthors, 2010. Description of the NCAR Community Atmosphere Model (CAM5.0). *NCAR Technical Note*, NCAR/TN-486-STR:268.

O'Dea, A., Lessios, H.A., Coates, A.G., Eytan, R.I., Restrepo-Moreno, S.A., Cione, A.L., Collins, L.S., De Queiroz, A., Farris, D.W., Norris, R.D. & Stallard, R.F., 2016. Formation of the Isthmus of Panama. *Science Advances*, 2(8), p.e1600883

Omta, A.W., Dijkstra, H.A., 2003. A physical mechanism for the Atlantic–Pacific flow reversal in the early miocene. *Glob. Planet. Change,* 36, 265–276

Otto-Bliesner, B. L. et al. 2017. Amplified North Atlantic warming in the late Pliocene by changes in Arctic gateways. 44, 957–964

Pantic, N.K., & Mihajlovic, D.S., 1977. Neogene floras of the Balkan land areas and their bearing on the study of palaeoclimatology, palaeobiogeography and biostratigraphy (part 2). The lower Sarmatian flora of Beograd. *Annales Geologiques de la Peninsule Balkanique*, 41.

Pantic, N.K., 1956. Biostratigraphie des flores tertiaires de Serbie. *Annales Geologiques de la Peninsule Balkanique*, 24, 199-317

Park, S. & Bretherton, C.S., 2009. The University of Washington Shallow Convection and Moist Turbulence Schemes and Their Impact on Climate Simulations with the Community Atmosphere Model. *Journal of Climate*, 22(12), 3449-3469

Pekar, S. F., & DeConto R. M., 2006. High-resolution ice-volume estimates for the early Miocene: Evidence for a dynamic ice sheet in Antarctica, *Palaeogeography, Palaeoclimatology, Palaeoecology*, 231(1-2), 101-109

Pithan, F. & Mauritsen, T. 2014. Arctic amplification dominated by temperature feedbacks in contemporary climate models, *Nature Geoscience,* **7**, 181–184

Pollard, D., & DeConto R. M., 2009. Modelling West Antarctic ice sheet growth and collapse through the past five million years, *Nature*, 458(7236), 329-332

Popova, S., Utescher, T., Gromyko, D., Bruch, A., & Mosbrugger, V., 2012. Palaeoclimate evolution in Siberia and the Russian Far East from the Oligocene to Pliocene–evidence from fruit and seed floras. *Turkish Journal of Earth Sciences*, 21, 315-334

Poore, H. R., Samworth, R., White, N. J., Jones, S. M. & McCave, I. N., 2006. Neogene overflow of Northern Component Water at the Greenland-Scotland Ridge, *Geochem. Geophys. Geosyst*., 7(6), Q06010

Pound, M.J. & Salzmann, U., 2017. Heterogeneity in global vegetation and terrestrial climate change during the late Eocene to early Oligocene transition. *Scientific Reports*, 7, 43386

Pound, M. J., Haywood, A. M., Salzmann, U., & Riding, J. B., 2012. Global vegetation dynamics and latitudinal temperature gradients during the Mid to Late Miocene (15.97–5.33Ma). *Earth-Science Reviews*, 112(1-2), –22

Prebble, J.G., Reichgelt, T., Mildenhall, D.C., Greenwood, D.R., Raine, J.I., Kennedy, E.M., & Seebeck, H.C., 2017. Terrestrial climate evolution in the Southwest Pacific over the past 30 million years. *Earth and Planetary Science Letters*, 459, 136-144

Raddatz, T., Reick, C. H., Knorr, W., Kattge, J. Roeckner, E., Schnur, R. Schnitzler, K. G. Wetzel P. & Jungclaus, J., 2007. Will the tropical land biosphere dominate the climate-carbon cycle feedback during the twenty-first century?, *Clim. Dyn.*, 29, 565– 574

Reichgelt, T., Kennedy, E.M., Conran, J.G., Mildenhall, D.C., & Lee, D.E., 2015. The early Miocene paleolake Manuherikia: vegetation heterogeneity and warm-temperate to subtropical climate in southern New Zealand. *Journal of Paleolimnology*, 53, 349-365

Renoult, M. et al. 2020. A Bayesian framework for emergent constraints: case studies of climate sensitivity with PMIP. Clim Past 16, 1715–1735

Retallack, G.J., & Kirby, M.X., 2007. Middle Miocene global change and paleogeography of Panama. *Palaios*, 22, 667-679

Roeckner, E. & Coauthors, 2006. Sensitivity of simulated climate to horizontal and vertical resolution in the ECHAM5 atmosphere model. *Journal of Climate,* 19, 3771-3791

Rommerskirchen, F., Condon, T., Mollenhauer, G., Dupont, L. M., & Schefuss, E., 2011. Miocene to Pliocene development of surface and subsurface temperatures in the Benguela Current system. *Paleoceanography*, 26(PA3216). https://doi.org/10.1029/2010PA002074

Rousselle, G., Beltran, C., Sicre, M. A., Raffi, I., & De Rafelis, M., 2013. Sea-surface condition changes in the Equatorial Pacific during the Mio-Pliocene as inferred from coccolith geochemistry. *Earth and Planetary Science Letters*, 361, 412–421

Ruddiman, W. F., & Kutzbach, J. E. (1989). Forcing of late Cenozoic northern hemisphere climate by plateau uplift in southern Asia and the American west. *Journal of Geophysical Research: Atmospheres*, 94(D15), 18409–18427. http://doi.org/10.1029/JD094iD15p18409

Sagoo, N., Valdes, P., Flecker, R., & Gregoire, L. J., 2013. The Early Eocene equable climate problem: can perturbations of climate model parameters identify possible solutions? *Philosophical Transactions of the Royal Society a: Mathematical, Physical and Engineering Sciences*, 371(2001), 20130123–20130123. http://doi.org/10.1098/rsta.2013.0123

Sagoo, N. & Storelvmo, T. 2017. Testing the Sensitivity of Past Climates to the Indirect Effects of Dust. *Geophysical Research Letters*, 44, 5807–5817

Sangiorgi, F., Bijl, P. K., Passchier, S., Salzmann, U., Schouten, S., McKay, R., et al., 2018. Southern Ocean warming and Wilkes Land ice sheet retreat during the mid-Miocene. *Nature Communications*, 9(1), 317. https://doi.org/10.1038/s41467-017-02609-7

Sangiorgi, F., Bijl, P.K., Passchier, S., Salzmann, U., Schouten, S., McKay, R., Cody, R.D., Pross, J., Van De Flierdt, T., Bohaty, S.M. & Levy, R., 2018. Southern Ocean warming and Wilkes Land ice sheet retreat during the mid-Miocene. *Nature Communications*, 9(1), 1-11

Scheiner, F., Holcová, K., Milovský, R., & Kuhnert, H., 2018. Temperature and isotopic composition of seawater in the epicontinental sea (Central Paratethys) during the Middle Miocene Climate Transition based on Mg/Ca, δ18O and δ13C from foraminiferal tests. *Palaeogeography, Palaeoclimatology, Palaeoecology*, 495, 60–71. https://doi.org/10.1016/j.palaeo.2017.12.027

Sepulchre, P., Caubel, A., Ladant, J.-B., Bopp, L., Boucher, O., Braconnot, P., Brockmann, P., Cozic, A., Donnadieu, Y., Estella-Perez, V., Ethé, C., Fluteau, F., Foujols, M.-A., Gastineau, G., Ghattas, J., Hauglustaine, D., Hourdin, F., Kageyama, M., Khodri, M., Marti, O., Meurdesoif, Y., Mignot, J., Sarr, A.-C., Servonnat, J., Swingedouw, D., Szopa, S., & Tardif, D., 2019. IPSL-CM5A2. An Earth System Model designed for multi-millennial climate simulations, *Geosci. Model DeDiscuss*., https://doi.org/10.5194/gmd-2019-332

Seki, O., Schmidt, D. N., Schouten, S., Hopmans, E. C., Sinninghe Damsté, J. S., & Pancost, R. D., 2012. Paleoceanographic changes in the Eastern Equatorial Pacific over the last 10 Myr. *Paleoceanography*, 27(3). https://doi.org/10.1029/2011PA002158

Shaw, T. A., Baldwin, M., Barnes, E. A., Caballero, R., Garfinkel, C. I., Hwang, Y. T., et al. 2016. Storm track processes and the opposing influences of climate change. *Nature Geoscience*, 9(9), 656–664

Shephard, G. E., Muller, R. D., Liu, L., & Gurnis M., 2010. Miocene drainage reversal of the Amazon River driven by plate-mantle interaction, *Nature Geoscience*, 3(12), 870-875

Shevenell, A. E., Kennett, J. P., & Lea, D. W., 2004. Middle Miocene Southern Ocean Cooling and Antarctic Cryosphere Expansion. *Science*, 305(5691), 1766–1770

Shevenell, A. E., Kennett, J. P., & Lea, D. W., 2004. Middle Miocene Southern Ocean Cooling and Antarctic Cryosphere Expansion. *Science*, 305(5691), 1766–1770 https://doi.org/10.1126/science.1100061

Shields, C. A., Bailey, D. A., Danabasoglu, G., Jochum, M., Kiehl, J. T., Levis, S., & Park, S., 2012. The Low-Resolution CCSM4, *Journal of Climate*, 25, 3993-4014, doi:10.1175/JCLI-D-11-00260.1

Sijp, W. P., Heydt, von der, A. S., Dijkstra, H. A., Flögel, S., Douglas, P. M. J., & Bijl, P. K., 2014. The role of ocean gateways on cooling climate on long time scales, *Glob. Planet. Change,* 119, 1–22 http://dx.doi.org/10.1016/j.gloplacha.2014.04.004.

Simon, D., Marzocchi, A., Flecker, R., Lunt, D.J., Hilgen, F.J. & Meijer, P. Th., 2017. Quantifying the Mediterranean freshwater budget throughout the late Miocene: New implications for sapropel formation and the Messinian Salinity Crisis, *Earth and Planetary Science Letters*, 472, 25-37

Sosdian, S. M., Greenop, R., Hain, M. P., Foster, G. L., Pearson, P. N., & Lear, C. H., 2018. Constraining the evolution of Neogene ocean carbonate chemistry using the boron isotope pH proxy. *Earth and Planetary Science Letters*, 498, 362–376.

Sosdian, S.M., Babila, T.L., Greenop, R., Foster, G.L. and Lear, C.H., 2020. Ocean Carbon Storage across the middle Miocene: a new interpretation for the Monterey Event. *Nature communications*, *11*(1), 1-11

Spicer, R.A., Harris, N.B.W., Widdowson, M., Herman, A.B., Guo, S., Valdes, P.J., Wolfe, J.A., & Kelley, S.P., 2003. Constant elevation of Southern Tibet over the past 15 million years. *Nature*, 412, 622-624

Stärz, M., Jokat, W., Knorr, G., & Lohmann, G., 2017. Threshold in North Atlantic-Arctic Ocean circulation controlled by the subsidence of the Greenland-Scotland Ridge. *Nature Communications*, 8(1), 15681. http://doi.org/10.1038/ncomms15681

Stein, R., Fahl, K., Schreck, M., Knorr, G., Niessen, F., Forwick, M., et al., 2016. Evidence for ice-free summers in the late Miocene central Arctic Ocean. *Nature Communications*, *7*(1), 1-13. http://doi.org/10.1038/ncomms11148

Steinke, S., Groeneveld, J., Johnstone, H., & Rendle-Bühring, R., 2010. East Asian summer monsoon weakening after 7.5Ma: Evidence from combined planktonic foraminifera Mg/Ca and δ18O (ODP Site 1146; northern South China Sea). *Palaeogeography, Palaeoclimatology, Palaeoecology*, 289(1), 33–43. https://doi.org/10.1016/j.palaeo.2010.02.007

Stevanovic, M.P., & Pantic, N., 1954. O sarmatskoj flori i fauni iz zeleznickih useka kod Bozdarevca Annales Geologiques de la Peninsule Balkanique 22, 53-68; Utescher, T., Djordjevic-Milutinovic, D., Bruch, A., Mosbrugger, V., 2007. Palaeoclimate and vegetation

change in Serbia during the last 30 Ma. *Palaeogeography, Palaeoclimatology, Palaeoecology*, 253, 141-152

Stoll, H. M., Guitian, J., Hernandez-Almeida, I., Mejía, L. M., Phelps, S., Polissar, P., et al., 2019. Upregulation of phytoplankton carbon concentrating mechanisms during low CO_2 glacial periods and implications for the phytoplankton pCO2 proxy. *Quaternary Science Reviews*, 208, 1-20

Su, B., Jiang, D., Zhang, R., Sepulchre, P., and Ramstein, G., 2018. Difference between the North Atlantic and Pacific meridional overturning circulation in response to the uplift of the Tibetan Plateau. *Clim. Past*, 14, 751–762, https://doi.org/10.5194/cp-14-751-2018

Sun, X., & Wang, P., 2005. How old is the Asian monsoon system?--Palaeobotanical records from China. *Palaeogeography, Palaeoclimatology, Palaeoecology*, 222, 181-222

Super, J.R., Thomas, E., Pagani, M., Huber, M., O'Brien, C.L. & Hull, P.M., 2020. Miocene Evolution of North Atlantic Sea Surface Temperature. Paleoceanography and Paleoclimatology. Accepted Author Manuscript. doi:10.1029/2019PA003748

Super, J. R., Thomas, E., Pagani, M., Huber, M., O'Brien, C., & Hull, P. M. (2018). North Atlantic temperature and pCO_2 coupling in the early-middle Miocene. *Geology*, 46(6), 519–522

Syabryaj, S., Utescher, T., Molchanoff, S., & Bruch, A.A., 2007. Vegetation and palaeoclimate in the Miocene of Ukraine. *Palaeogeography, Palaeoclimatology, Palaeoecology*, 253, 153-168

Syabryaj, S., 2002. Vegetation and climate of the Ukraine in the Neogene. *Acta Universitatis Carolinae Geologica*, 46, 49-55

Takeuchi, A., Larson, P.B., & Suzuki, K., 2007. Influence of paleorelief on the Mid-Miocene climate variation in southeastern Washington, northeastern Oregon, and western Idaho, USA. *Palaeogeography, Palaeoclimatology, Palaeoecology*, 254, 462-476

Tao, J.-J., 1997. The paleofloristic and paleoclimatic changes during the Mid-Miocene in China. In: Jablonski, N.G. (Ed.), The changing face of East Asia during the Tertiary and Quaternary. The University of Hong Kong, Hong Kong

Tierney, J. & Tingley, M., 2014. A Bayesian, spatially-varying calibration model for the TEX86 proxy Geochimica et Cosmochimica Acta 127(C), 83 - 106. https://dx.doi.org/10.1016/j.gca.2013.11.026

Thiede, J., Jessen, C., Knutz, P., Kuijpers, A., Mikkelsen, N., Nørgaard-Pedersen, N., & Spielhagen, R. F., 2011. Millions of Years of Greenland Ice Sheet History Recorded in Ocean Sediments. *EPIC3Polarforschung, Bremerhaven, Alfred Wegener Institute for Polar and Marine Research & German Society of Polar Research,* 80(3), 141-159, ISSN: 0032-2490.

Thompson, S. L. & Pollard, D., 1997. Greenland and Antarctic mass balances for present and doubled atmospheric CO2 from the GENESIS version-2 global climate model, *Journal of Climate*, 10, 871–900

Tzanova, A., Herbert, T. D., & Peterson, L., 2015. Cooling Mediterranean Sea surface temperatures during the Late Miocene provide a climate context for evolutionary transitions in Africa and Eurasia. *Earth and Planetary Science Letters*, 419, 71–80. https://doi.org/10.1016/j.epsl.2015.03.016

Uhl, D., Bruch, A., Traiser, C., Klotz, S., 2006. Palaeoclimate estimates for the Middle Miocene Schrotzburg flora (S Germany): a multi-method approach. *International Journal of Earth Sciences*, 95, 1071-1085

Uhl, D., Mosbrugger, V., Bruch, A. & Utescher, T., 2003. Reconstructing palaeotemperatures using leaf floras–case studies for a comparison of leaf margin analysis and the coexistence approach. *Review of Palaeobotany and Palynology*, 126(1-2), 49-64

Utescher, T., Bruch, A.A., Erdei, B., François, L., Ivanov, D., Jacques, F.M.B., Kern, A.K., Mosbrugger, & Spicer, R.A., 2014. The Coexistence Approach—theoretical background and practical considerations of using plant fossils for climate quantification. *Palaeogeography, Palaeoclimatology, Palaeoecology*, 410, 58-73

Utescher, T., Djordjevic-Milutinovic, D., Bruch, A., Mosbrugger, V., 2007. Palaeoclimate and vegetation change in Serbia during the last 30 Ma. *Palaeogeography, Palaeoclimatology*, *Palaeoecology*, 253, 141-152

Utescher, T., Mosbrugger, V., Ashraf, A.R., 2000. Terrestrial climate evolution in northwest Germany over the last 25 million years. *Palaios*, 15, 430-449

Valdes, P.J., Armstrong, E., Badger, M.P., Bradshaw, C.D., Bragg, F., Davies-Barnard, T., Day, J.J., Farnsworth, A., Hopcroft, P.O., Kennedy, A.T. & Lord, N.S., 2017. The BRIDGE HadCM3 family of climate models: HadCM3@ Bristol v1. 0. *Geoscientific Model Development*, 10, 3715-3743

Valcke, S. 2006. OASIS3 user's guide (prism-2-5). Tech. Rep. TR/CMGC/06/73, PRISM Report No 3, CERFACS, Toulouse, France

van Ufford, A. Q., & Cloos M., 2005. Cenozoic tectonics of New Guinea, *AAPG Bulletin*, 89(1), 119-140

Vincent, E. and Berger, W.H., 1985. Carbon dioxide and polar cooling in the Miocene: The Monterey hypothesis. *The carbon cycle and atmospheric CO_2: Natural variations Archean to present*, *32*, 455-468

von der Heydt, A., Dijkstra, H.A., 2006. Effect of ocean gateways on the global ocean circulation in the late Oligocene and early Miocene. *Paleoceanography,* 21, PA1011. http://dx.doi.org/10.1029/2005PA001149.

Wang, S., Shi, Q., Hui, Z., Li, Y., Zhang, J. & Peng, T., 2015. Diversity of Moschidae (Ruminantia, Artiodactyla, Mammalia) in the Middle Miocene of China. *Paleontological Research*, 19(2), 143-156

Wang, W.-M., 2006. Correlation of pollen sequences in the Neogene palynofloristic regions of China. *Palaeoworld*, 15, 77-99

Wang, P., 1990. Neogene stratigraphy and paleoenvironments of China. *Palaeogeography, Palaeoclimatology, Palaeoecology*, 77, 315-334

Weidick, A., Williams, R. S. & Ferrigno, J. G., 1995. Satellite Image Atlas of Glaciers of the World: Greenland, *US Government Printing Office*

Wheeler, E.A., Wiemann, M.C., & Fleagle, J.G., 2007. Woods from the Miocene Bakate Formation, Ethiopia: Anatomical characteristics, estimates of original specific gravity and ecological inferences. *Review of Palaeobotany and Palynology*, 146, 193-207

White, J.M., & Ager, T.A., 1994. Palynology, paleoclimatology and correlation of middle Miocene beds from Porcupine River (locality 90-1), Alaska. *Quaternary International*, 22-23, 43-77

Wiemann, M.C., Manchester, S.R., Wheeler, E.A., 1999. Paleotemperature estimation from dicotyledonous wood anatomical characters. *PALAIOS*, 14, 459-474

Wilson, D. S., & Luyendyk B. P., 2009. West Antarctic paleotopography estimated at the Eocene-Oligocene climate transition, *Geophysical Research Letters*, 36(16), L16302

Wilson, D. S., Jamieson, S. S. R., Barrett, P. J., Leitchenkov G., Gohl K., & Larter, R. D., 2012. Antarctic topography at the Eocene–Oligocene boundary, *Palaeogeography, Palaeoclimatology, Palaeoecology*, 335–336(0), 24-34

Winkler, A., Wolf-Welling, T., Stattegger, K. & Thiede, J. 2002. Clay mineral sedimentation in high northern latitude deep-sea basins since the Middle Miocene (ODP Leg 151, NAAG). International Journal of Earth Sciences, 91, 133-148.

Wolfe, J.A., 1971. Tertiary climatic fluctuations and methods of analysis of Tertiary floras. *Palaeogeography, Palaeoclimatology, Palaeoecology*, 9(1), 27-57

Yang, J., Spicer, R.A., Spicer, T.E. & Li, C.S., 2011. 'CLAMP Online': a new web-based palaeoclimate tool and its application to the terrestrial Paleogene and Neogene of North America. *Palaeobiodiversity and Palaeoenvironments*, 91(3), 163

Yao, Y.-F., Bruch, A.A., Mosbrugger, V., & Li, C.-S., 2011. Quantitative reconstruction of Miocene climate patterns and evolution in Southern China based on plant fossils. *Palaeogeography, Palaeoclimatology, Palaeoecology*, 304, 291-307

You, Y., Huber, M., Müller, R. D., Poulsen, C. J., & Ribbe, J. (2009). Simulation of the middle Miocene climate optimum. Geophysical Research Letters, 36(4).

Zachos, J., Dickens, G., Zeebe, R., 2008. An early Cenozoic perspective on greenhouse warming and carbon-cycle dynamics. *Nature,* 451(7176), pp. 279-283.

Zachos, J., Pagani, M., Sloan, L., Thomas, E. & Billups, K., 2001. Trends, rhythms, and aberrations in global climate 65 Ma to present. *Science*, 292(5517), 686-693

Zhang, X., Prange, M., Steph, S., Butzin, M., Krebs, U., Lunt, D. J., Nisancioglu, K. H., Park, W., Schmittner, A., Schneider, B., & Schulz, M., 2012b. Changes in equatorial Pacific thermocline depth in response to Panamanian seaway closure: Insights from a multi-model study. *Earth and Planetary Science Letters*, 317-318, 76-84

Zhang, Y., Pagani, M., & Liu, Z., 2014. A 12-Million-Year Temperature History of the Tropical Pacific Ocean. *Science*, 344, 84–87. https://doi.org/10.1126/science.1246172

Zhang, Y. G., Pagani, M., Liu, Z., Bohaty, S., & DeConto, R., 2013. A 40-million-year history of atmospheric CO_2. *Philosophical Transactions of the Royal Society of London Series* A, 371. https://doi.org/20130096

Zhang, Z.-S., Ramstein, G., Schuster, M., Li, C., Contoux, C., Yan, Q., 2014. Aridification of the Sahara desert caused by Tethys Sea shrinkage during the Late Miocene. *Nature* 513, 401-404

Zhang, Z., Nisancioglu, K. H., Ninnemann, U. S., 2013. Increased ventilation of Antarctic deep water during the warm mid-Pliocene. *Nat. Commun*. 4, 1499

Zhang, Z.-S., Nisancioglu, K., Bentsen, M., Jiputra, J., Bethke, I., Yan, Q., Risebrobakken, B., Andersson, C., & Jansen, E., 2012a. Pre-industrial and mid-Pliocene simulations with NorESM-L. *Geosci. Model De*5, 523-533

Zhao, L.-C., Wang, Y.-F., Liu, C.-J., & Li, C.-S., 2004. Climatic implications of fruit and seed assemblage from Miocene of Yunnan, southwestern China. *Quaternary International*, 117, 81-89

Zhi-Cheng, L., Lin, A.T.-S., Shun-Wen, Y., Liao, T.-P., Gui-Wen, X., 2013. Fossil Seed from the Miocene Shihti Formation of Taiwan. *TAO: Terrestrial, Atmospheric and Oceanic Sciences*, 24, 731

Zhou, H., Helliker, B. R., Huber, M., Dicks, A., & Akçay, E., 2018. C4 photosynthesis and climate through the lens of optimality. *Proceedings of the National Academy of Sciences*, 115(47), 12057-12062

Zhu, J., & Poulsen, C. J. 2019. Quantifying the Cloud Particle-Size Feedback in an Earth System Model. *Geophysical Research Letters*, 46(19), 10910–10917. http://doi.org/10.1029/2019GL083829

Zhu, J., Poulsen, C. J., & Tierney, J. E., 2019. Simulation of Eocene extreme warmth and high climate sensitivity through cloud feedbacks. *Science Advances*, 5(9), eaax1874. http://doi.org/10.1126/sciadv.aax1874

Table 1: Late Miocene experiments with paleogeography that falls within 11.6-5.3Ma (Tortonian & Messinian)

Modelling effort	Target time period	Resolution Atm/Ocn	Length (years analyzed)	CO_2 levels	Veg	Methane levels	Aerosols	Orbit	Greenland ice sheet	Antarctic ice sheet	Paleo-geographic forcing used	Exp Names (original study)	Exp Names (this study)	Refs
COSMOS T31 (AWI)	Tortonian (11-7Ma)	3.75° x 3.75° / ~3°	2000 (last 100)	278 450	Prescribed Micheels et al. 2007; 2011)	PI (650)	PI	modern	No	modern Antarctic IS height	Tortonian (11-7 Ma) Micheels et al. 2011 with minor modifications cf. Knorr et al. 2011	MIO ICE_FULL_ CO2_450	"COSMOS Late Miocene 278/450ppm"	Knorr et al. 2011 Knorr & Lohmann 2014
				278 450					No	25% modern Antarctic IS height		ICE_Quarter _CO2_278 ICE_Quarter _CO2_450	"COSMOS Late Miocene ICEQ 278/450ppm"	Knorr & Lohmann 2014
HadCM3L - Bradshaw	Late Miocene	3.75° x 2.5° / 3.75° x 2.5°	2100 (last 50)	280 400	Dynamic	PI (760)	PI	Modern	Yes	Yes	Markwick, 2007	tczth tczti	"HadCM3L Late Miocene 280/400ppm"	Bradshaw et al., 2012
HadCM3L - Farnsworth	Tortonian	3.75° x 2.5° / 3.75° x 2.5°	7422 (last 100)	400	Dynamic	PI (760)	PI	Modern	Yes	Yes	Getech Plc.	teupn	"HadCM3L Tortonian 400ppm"	Farnsworth, et al. 2019a
	Messinian											teupo	"HadCM3L Messinian 400ppm"	
NorESM-L	10Ma	T31 ~3.75° /~3°	>2000 (last 200)	420 560	Idealized	PI	PI	Modern	No	No	Zhang et al., 2014	LM 420 LM 560	"NorESM-L 10Ma 350/560ppm"	Zhang et al., 2014

Table 2: Middle and Early Miocene experiments with paleogeography that falls within 20-11.6Ma (Burdigalian, Langhian & Serravallian)

Modelling effort	Target time period	Resolution Atm/Ocn	Length (years analyzed)	CO_2 levels ppmv	Veg	Methane levels ppb	Aerosols	Orbit	Greenland ice sheet	Antarctic ice sheet	Paleo-geographic forcing used	Exp Name (original study)	Exp Name (this study)	Refs
CCSM-NH3	~20-14Ma	T31 ~3.75° /~3x1.5°	1100 (last 100)	355 560	Fixed - early Miocene	PI (760)	PI	modern	Herold et al., 2008	Herold et al., 2008	Herold et al 2011a	m0015 m0025	"CCSM-NH3 355ppm" "CCSM-NH3 560ppm"	Herold et al 2011; 2012
CCSM3 T42 (MARUM)	MMCO	T42 ~2.8° / 1°	1500 (last 100)	400 200	Frigola et al. (2018) based on Pound et al. (2012), Wolfe (1985), Morley (2011)	PI (760)	PI	modern	No	6.e6 km3	Frigola et al. (2018) based on Herold et al. (2011a), Hall (2012), Montes et al. (2012)	MMCO MMCO_200	"CCSM3 T42 MMCO 400ppm" "CCSM3 T42 MMCO 200ppm"	Frigola et al. (2018)
	MMG			200 400						23.e6 km3		MMG MMG_400	"CCSM3 T42 MMG 200ppm" "CCSM3 T42 MMG 400ppm"	Frigola et al. (2018)
CCSM4	~20-14 Ma	~1.9° x 2.5° / 1°	2000 (last 100)	400	Fixed - early Miocene	PI (791)	PI	modern	0.29e6 km^3	6.5e6 km^3	As described in in this article (updated Herold et al 2011a)	B.MIO_400_C4	"CCSM4 400ppm"	
CESM1 (CAM5)	~20-14 Ma	~1.9° x 2.5° / 1°	3000 (last 50)	400	Fixed early Miocene	PI (791)	PI (aerosol flux close to PI)	modern	0.29e6 km^3	6.5e6 km^3	As described in in this article (updated Herold et al 2011a)	B.MIO_400_C5	"CESM1 400ppm"	
COSMOS T31 (AWI)	Middle Miocene (Herold ~20-14)	3.75° x 3.75° / ~3°	2000 (last 100)	278 450	Dynamic	PI (650)	PI	modern	No	Herold et al., 2008	Middle Miocene (Herold et al 2011a) + regional bathymetry reconstruction (15 Ma) North Atlantic/Arctic (Ehlers &Jokat,2013)	EO_278 EO_450	"COSMOS Mid Miocene 278ppm" "COSMOS Mid Miocene 450ppm"	Stärz et al., 2017
HadCM3L - Bradshaw	Mid Miocene	3.75° x 2.5° / 3.75° x 2.5°	2000 (last 50)	850 560 400 280	Dynamic	760 (PI)	PI	Modern	No	90mSLE	Markwick, 2007	teudt teudl teudi teude	"HadCM3L Mid Miocene 90SLE 850/560/400/280ppm"	Bradshaw et al. 2020
				850 560 400 280						55mSLE		teuds teudk teudc teudz	"HadCM3L Mid Miocene 55SLE 850/560/400/280ppm"	
				850 560 400 280						No		teudu teudq teudp teudo	"HadCM3L Mid Miocene NOSLE 850/560/400/280ppm"	
HadCM3L - Farnsworth	Langhian	3.75° x 2.5° / 3.75° x 2.5°	7422 (last 100)	280 400 560	Dynamic	760 (PI)	PI	Modern	No	Yes	Getech Plc.	teupl teupL teupla	"HadCM3L Langhian 280/400/560ppm"	Farnsworth, et al. 2019a
IPSLCM5A2	20Ma	3.75° ×1.875° /~2x0.5°	3000 (last 100)	840 560 420	Idealized	291 (PI)	PI	Modern	Yes	Yes	ERC MAGIC	C20M-ICE-GA-840 C20M-ICE-GA C20M-ICE-GA-420	"IPSLCM 20Ma 840/560/420ppm"	
				560					No			C20M-ICE-NoGIS	"IPSLCM 20Ma NoGIS 560ppm"	
NorESM-L	20Ma	T31 ~3.75° /~3°	>2000 (last 200)	350 560	Idealized	PI	PI	Modern	No	No	Zhang et al., 2014	EM 350 EM 560	"NorESM-L 20Ma350/ 560ppm"	Zhang et al., 2014

Table 3: Orbital parameter sensitivity experiments

Modelling effort	Target time period	Resolution Atm/Ocn	Length (years analyzed)	CO_2 levels (ppmv)	Veg	Aerosols	Orbit	Greenland ice sheet	Antarctic ice sheet	Paleo-geographic forcing used	Exp Names	Exp Names (this study)	Refs
Genesis (slab ocean)	Middle Miocene (Herold ~20-14Ma)	T31/slab	50 (last 30)	280 840 2240	Dynamic	PI	3 different orbital configurations	No	Fully Glaciated	Herold et al 2012	1FUCObi 1FUMEbi 1FUWAbi 3FUCObi 3FUMEbi 3FUWAbi 8FUCObi 8FUMEbi 8FUWAbi	1FUCObi 1FUMEbi 1FUWAbi 3FUCObi 3FUMEbi 3FUWAbi 8FUCObi 8FUMEbi 8FUWAbi	Gasson et al., 2016
				280 840 2240					Partially Glaciated		1MECObi 1MEMEbi 1MEWAbi 3MECObi 3MEMEbi 3MEWAbi 8MECObi 8MEMEbi 8MEWAbi	1MECObi 1MEMEbi 1MEWAbi 3MECObi 3MEMEbi 3MEWAbi 8MECObi 8MEMEbi 8MEWAbi	
				280 840 2240					Unglaciated		1NOCObi 1NOMEbi 1NOWAbi 3NOCObi 3NOMEbi 3NOWAbi 8NOCObi 8NOMEbi 8NOWAbi	1NOCObi 1NOMEbi 1NOWAbi 3NOCObi 3NOMEbi 3NOWAbi 8NOCObi 8NOMEbi 8NOWAbi	
HadCM3L - Marzocchi	Late Miocene (Messinian)	3.75° x 2.5° / 3.75° x 2.5°	200 plus additional 2100-year spin-up without orbital variability (last 50)	280	Dynamic	PI	modern 125k orbit min seasonality max seasonality NH max seasonality SH	Reduced	Reduced	Markwick, 2007	tdiub tdiud tdiue tdiuf tdiug	"HadCM3L ModernOrbit" "HadCM3L 125kOrbit" "HadCM3L min seasonality" "HadCM3L max seasonality NH" "max seasonality SH"	Marzocchi et al., 2016; Simon et al., 2017; Marzocchi et al., 2019

Table 4: Description of key characteristics associated with the various baseline paleogeographic forcing used

Baseline paleogeographic forcing used	Panama Gateway	Bering Strait	Barents Sea Landmass	Indonesian Seaway	Tethys Seaway	Greenland-Scotland Ridge	Canadian Archipelago
Middle and Early Miocene							
Herold et al. 2011a	Open	Closed	Present	Open	Open	Deep	Closed
Described in this article (updated Herold et al 2011a, see supplementary information)	Open	Closed	Present	Open	Open	Shallow	Closed
Frigola et al. (2018) which is based on Herold et al. (2012), Hall (2012), Montes et al. (2012)	Open	Closed	Present	Open	Open	Deep	Closed
Middle Miocene (Herold) + regional bathymetry reconstruction (15 Ma) North Atlantic/Arctic (Ehlers & Jokat, 2013)	Open	Closed	Present	Open	Open	Deep	Closed
ERC MAGIC Poblete et al. accepted	Open	Closed	Present	Open	Closed	Deep	Closed
Zhang et al., 2014 20Ma	Open	Closed	Present	Open	Open	Shallow (less than 450m)	Closed
Getech Plc.	Open	Closed	Filled with land in region of LGM Fennoscandian ice sheet	Open	Closed	Shallow	Closed
Late Miocene							
Markwick, 2007	Open	Closed	Present	Open	Closed	Deep	Closed
Tortonian (11-7 Ma) Micheels et al. 2011 with minor modifications cf. Knorr et al. 2011	Open	Closed	Present	Open	Closed	Deep	Open
Getech Plc.	Open	Closed	Present	Open	Closed	Deep	Closed
Zhang et al., 2014 10Ma	Open	Closed	Present	Open	Closed	Shallow (250-300m)	Closed

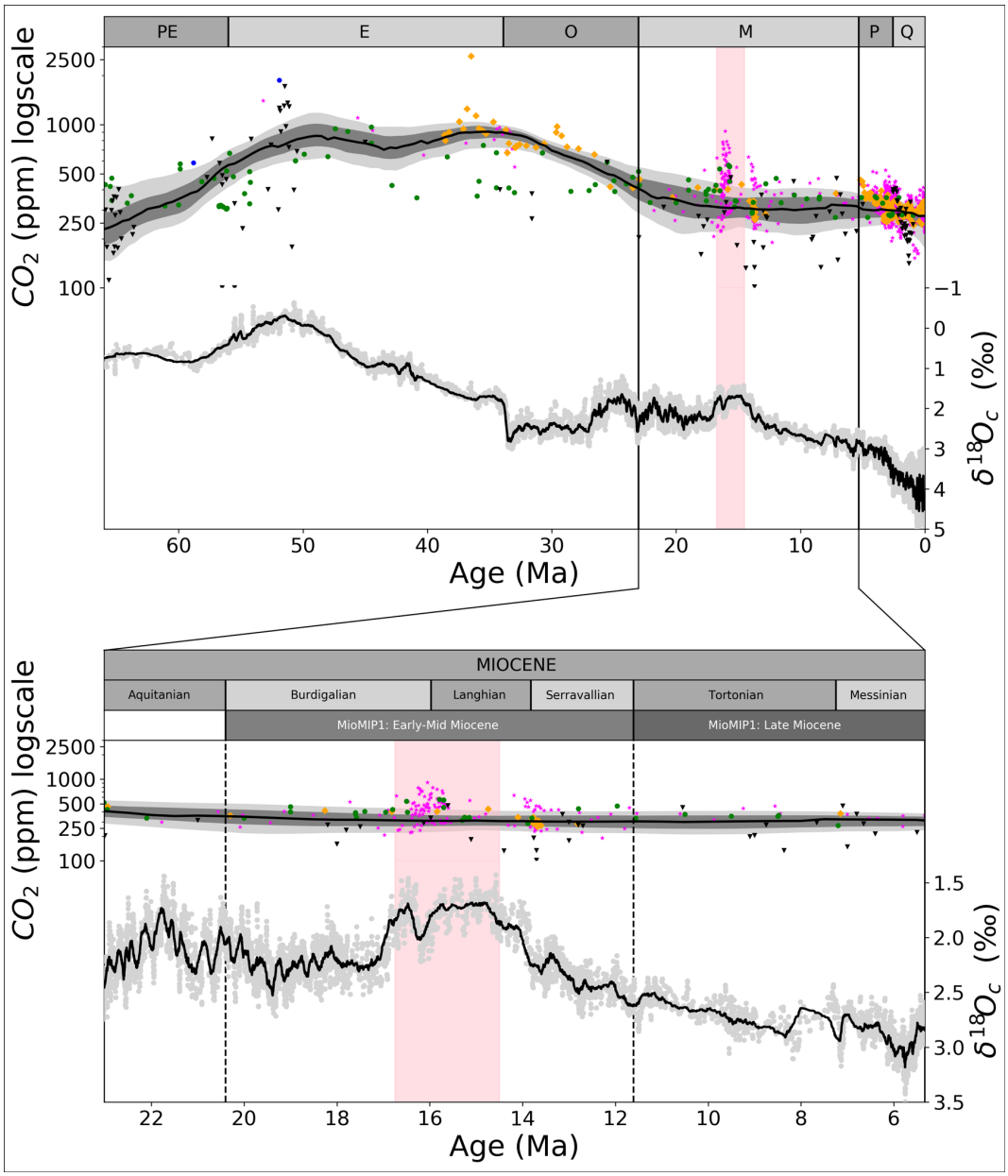

Fig. 1: The Miocene within the Cenozoic. The Late Miocene (Tortonian and Messinian, 11.6-5.3Ma) and Early-Middle Miocene (Burdigalian, Langhian and Serravallian, 20-11.6Ma). Multiproxy CO_2 reconstructions from Foster et al. (2017) compilation and Sosdian et al. (2018). CO_2 from leaf stomata shown in green circles, pedogenic carbonate $\delta^{13}C$ as black triangles, boron isotopes in foraminifera as pink stars, liverwort $\delta^{13}C$ as blue octagons and $\delta^{13}C$ of alkenones as orange diamonds. The most likely fit through the data is shown as the black line and 68 and 95% confidence intervals are shown as dark and light grey bands. Benthic oxygen isotopic composition ($\delta^{18}O_c$) taken from Zachos et al. (2001 and 2008). The MioMIP Early/ The time period abbreviations shown in the top bar are as follows: PE=Paleocene, E=Eocene, O=Oligocene, M=Miocene, P=Pliocene, Q=Quaternary.

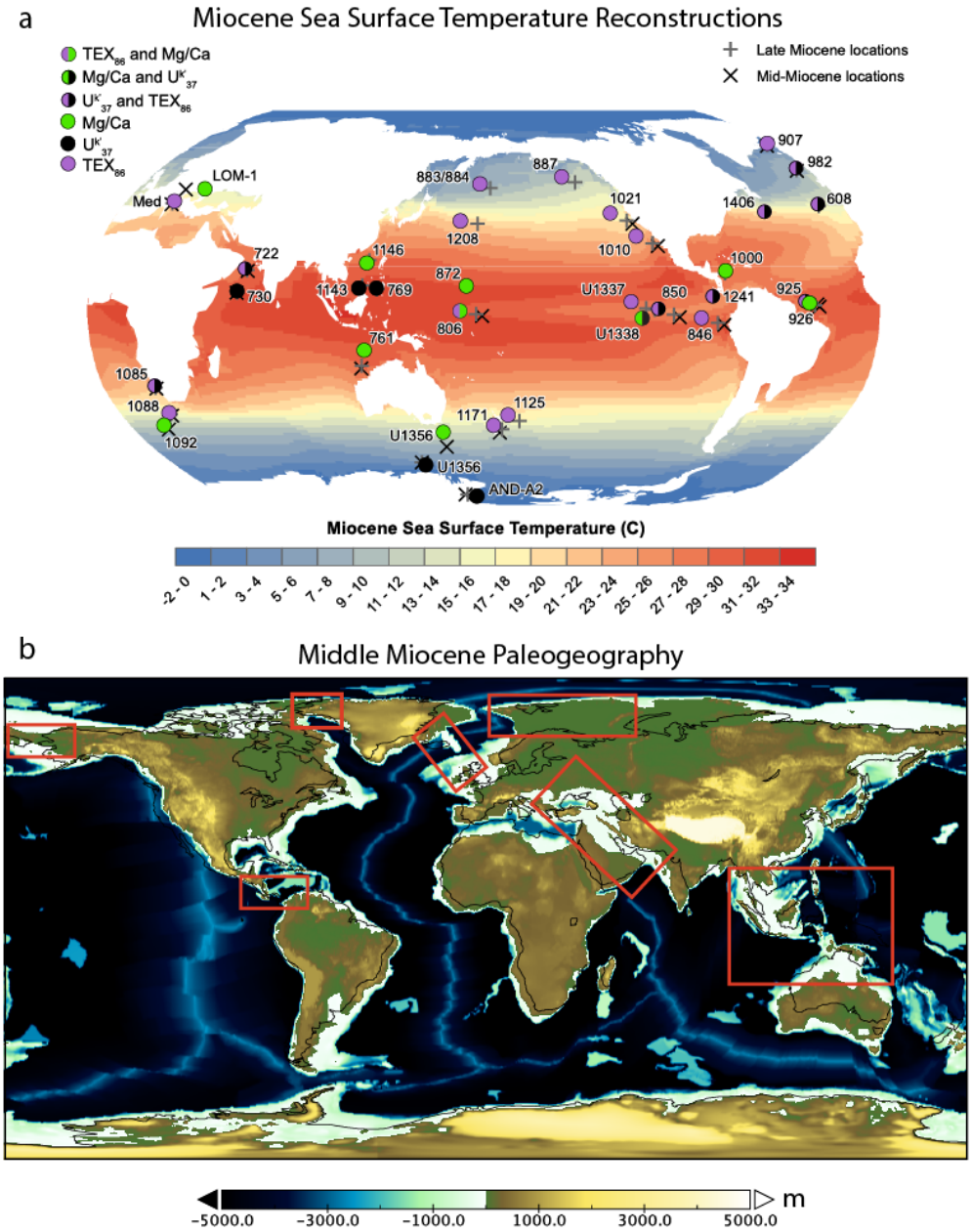

Fig. 2: (a) The Middle and Late Miocene sea surface temperature reconstructions synthesized and used within our model-data comparison. The cross (plus) symbols indicate the average Middle (Late) Miocene site location, while filled circles indicate the modern site location. The color coding of each circle indicates the type of proxy record available for each site. The contoured sea surface temperature field shown is derived from the multi model mean of all of the simulations listed in Table 2 with Middle Miocene boundary conditions. (b) The Middle Miocene paleogeography described and made available in this article (updated Herold et al 2011a, see supplementary information). The red boxes highlight prominent paleogeographic features that evolved over the Miocene and into the Pliocene, namely: Panama Gateway, Bering Strait, Barents Sea Landmass, Indonesian Seaway, Tethys Seaway, Greenland-Scotland Ridge and the Canadian Archipelago. See Table 4 for a description of the key characteristics associated with the various baseline paleogeographic forcings used across the MioMIP simulations.

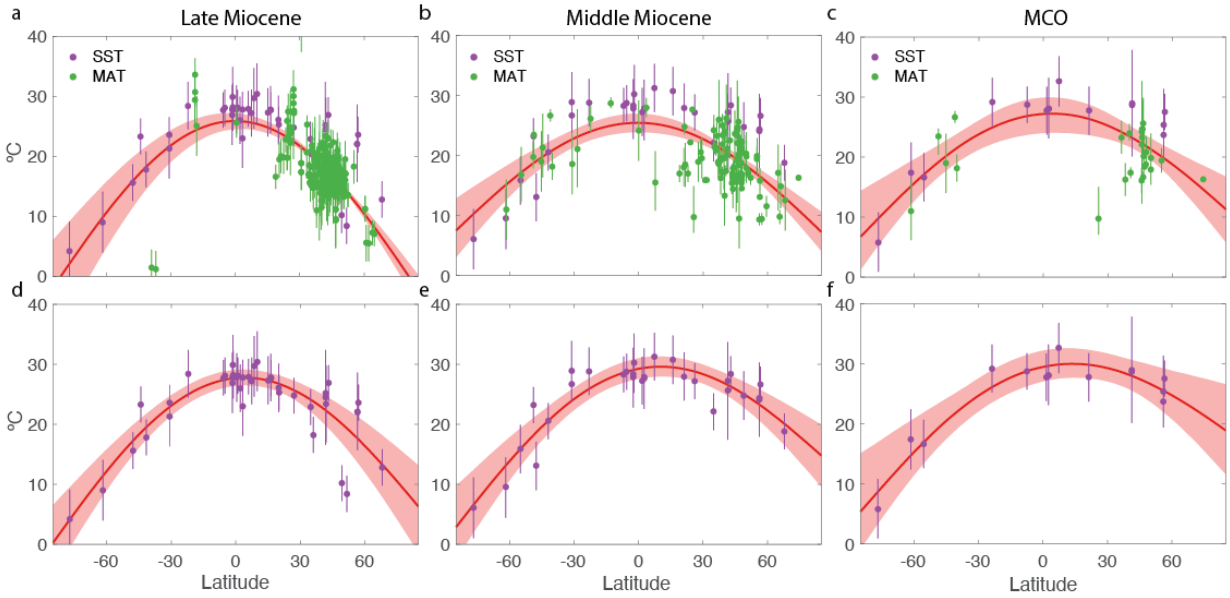

Fig. 3: (Top row) Average zonal mean surface temperature estimate (red line), +/- one standard deviation (red shading), computed from proxy MAT (green) and SST (purple) data for (a) the Late Miocene, (b) Middle Miocene, (c) and MCO. (Bottom row) Average zonal mean surface temperature estimate calculated using only the SST (purple) data for (d) the Late Miocene, € Middle Miocene, and (f) MCO.

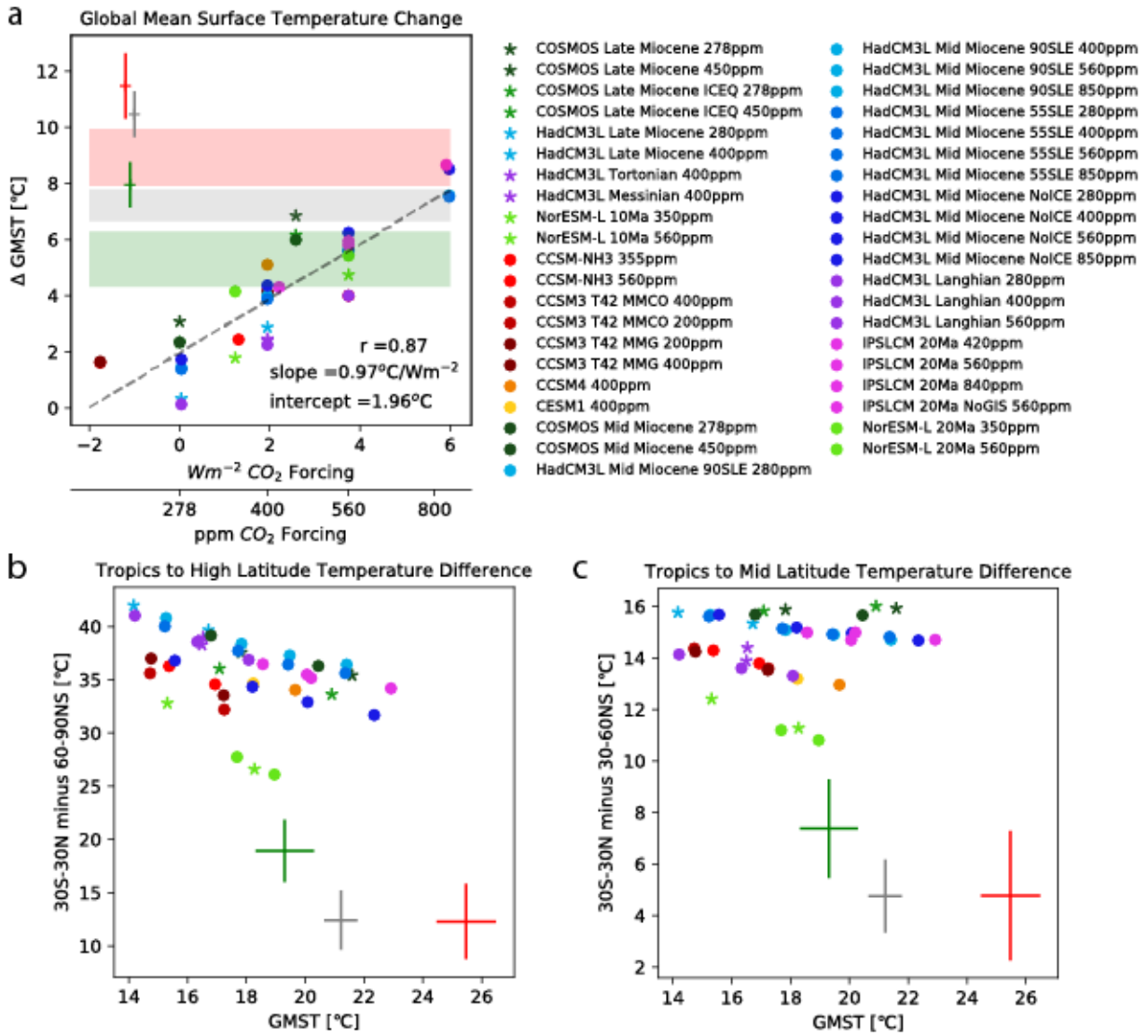

Fig. 4: (a) The global mean surface temperature change (relative to the preindustrial control) versus prescribed atmospheric CO_2 concentration. The green, grey and red shading indicate the Late Miocene, Middle Miocene and MCO global mean surface temperature change estimates derived from the mean annual terrestrial and sea surface temperature reconstructions (Fig. 3, top row), while the crosses show the equivalent global mean surface temperature change estimates based only on the sea surface temperature proxies (Fig. 3, bottom row). (b & c) Global mean surface temperature versus (b) the tropics (30°S-30°N) to high latitude (60-90°N&S) temperature difference and (c) the tropics (30°S-30°N) to middle latitude (30-60°N&S) temperature difference. The green, grey and red shading indicate the Late Miocene, Middle Miocene and MCO estimates derived from the mean annual terrestrial and sea surface temperature reconstructions (Fig. 3, top row).

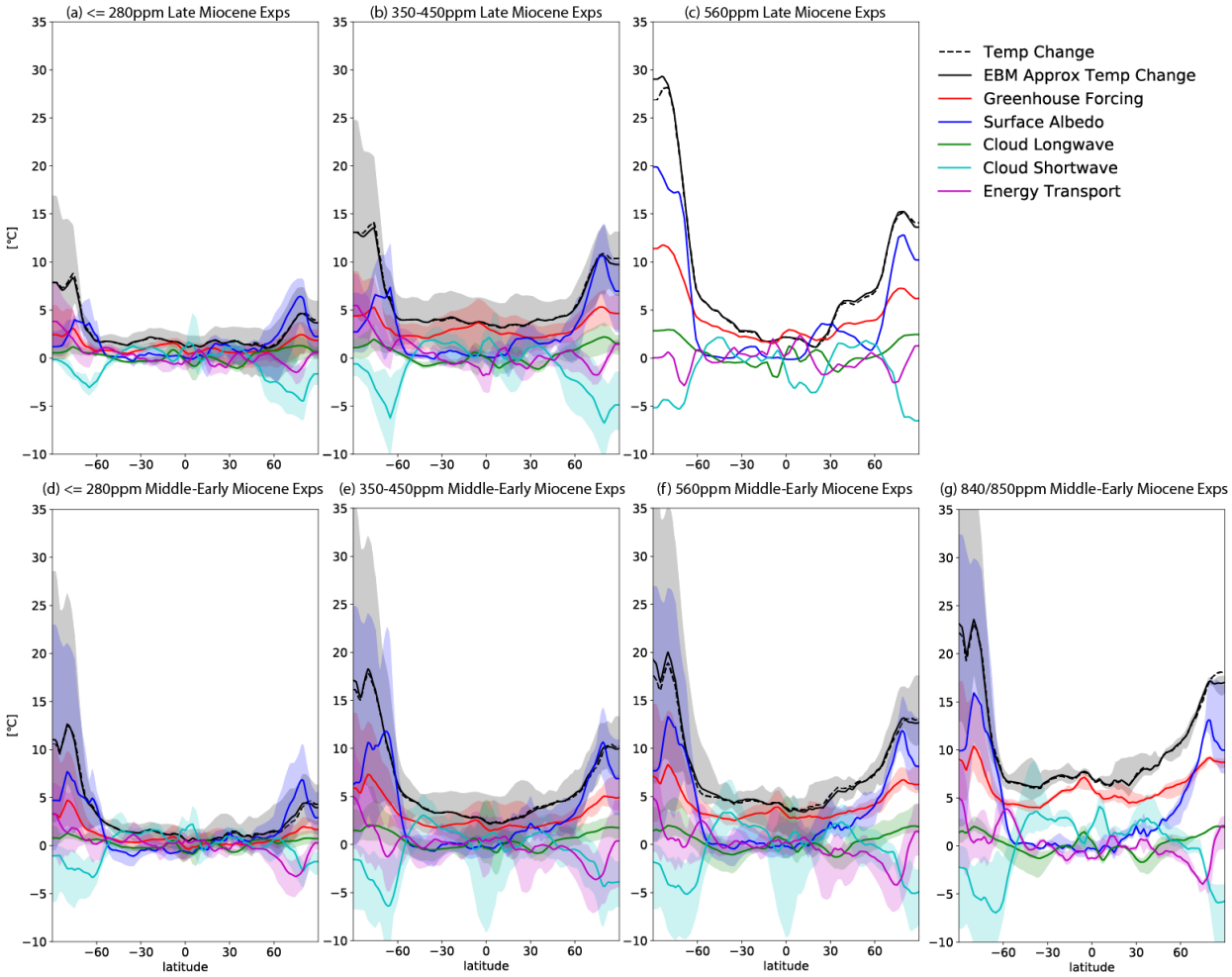

Fig. 5: The multi-model-mean of the energy balance analysis for the set of Late Miocene experiments with (a) 278 or 280 ppm, (b) 350-450 ppm and (c) 560 ppm CO_2, and the set of Middle-Early Miocene experiments with (d) 278 or 280 ppm, (e) 350-450 ppm, (f) 560 ppm, and (g) 840/850 ppm CO_2. Note that the variables required for this analysis were not available for the HadCM3L Tortonia, Messinian and Langhian experiments, see Figs S3 & S4 for the individual experiments.

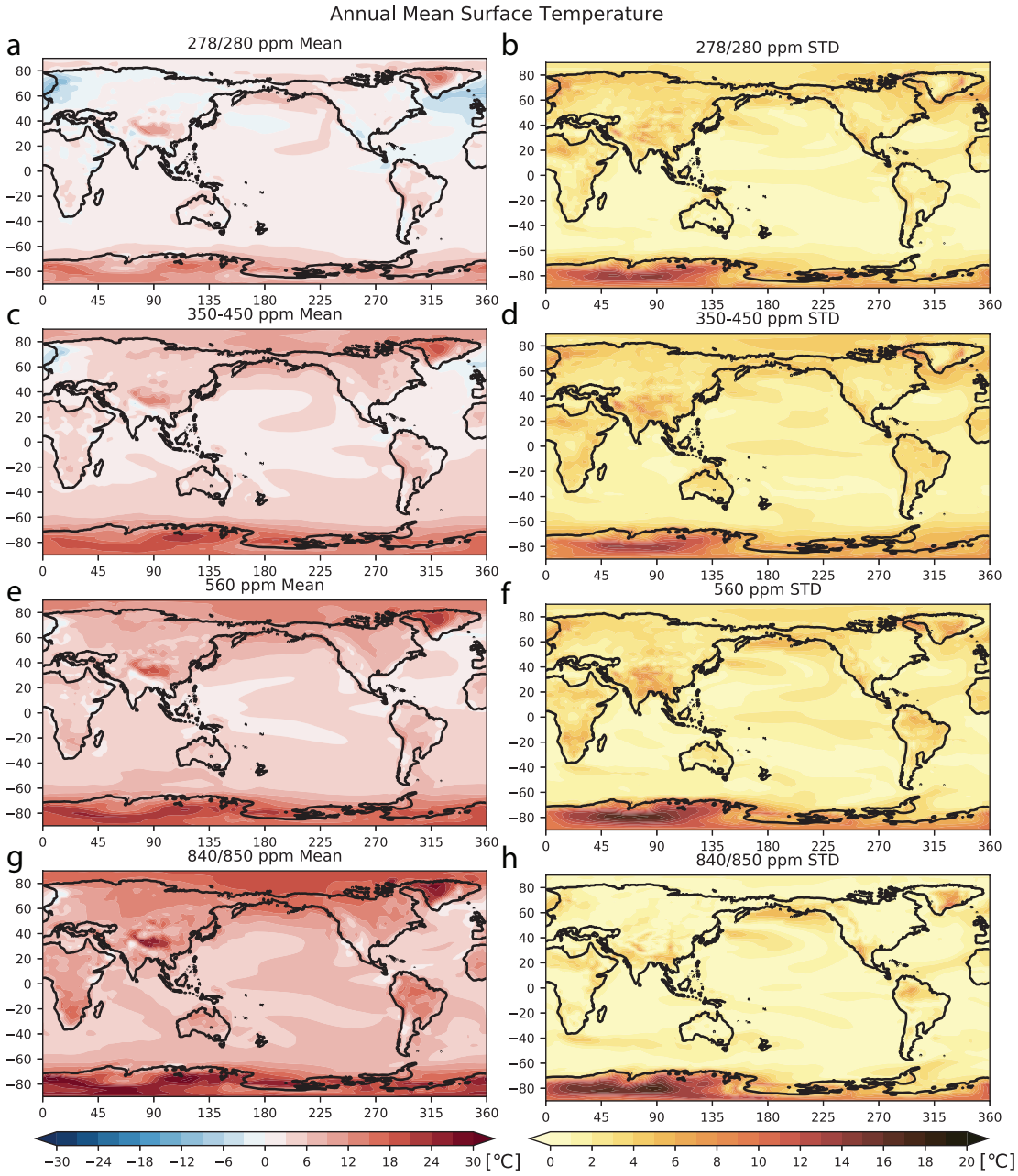

Fig. 6: (Left) The multi-model-mean of the annual mean surface temperature change relative to the preindustrial control for the set of experiments with (a) 278 or 280 ppm, (c) 350-450 ppm, (e) 560 ppm, and (g) 840/850 ppm CO_2. (Right) The standard deviation of this temperature change across the experiments making up each set. The continental outline from the updated Herold et al 2011a paleogeographic boundary conditions described in this article has been used (see supplementary information).

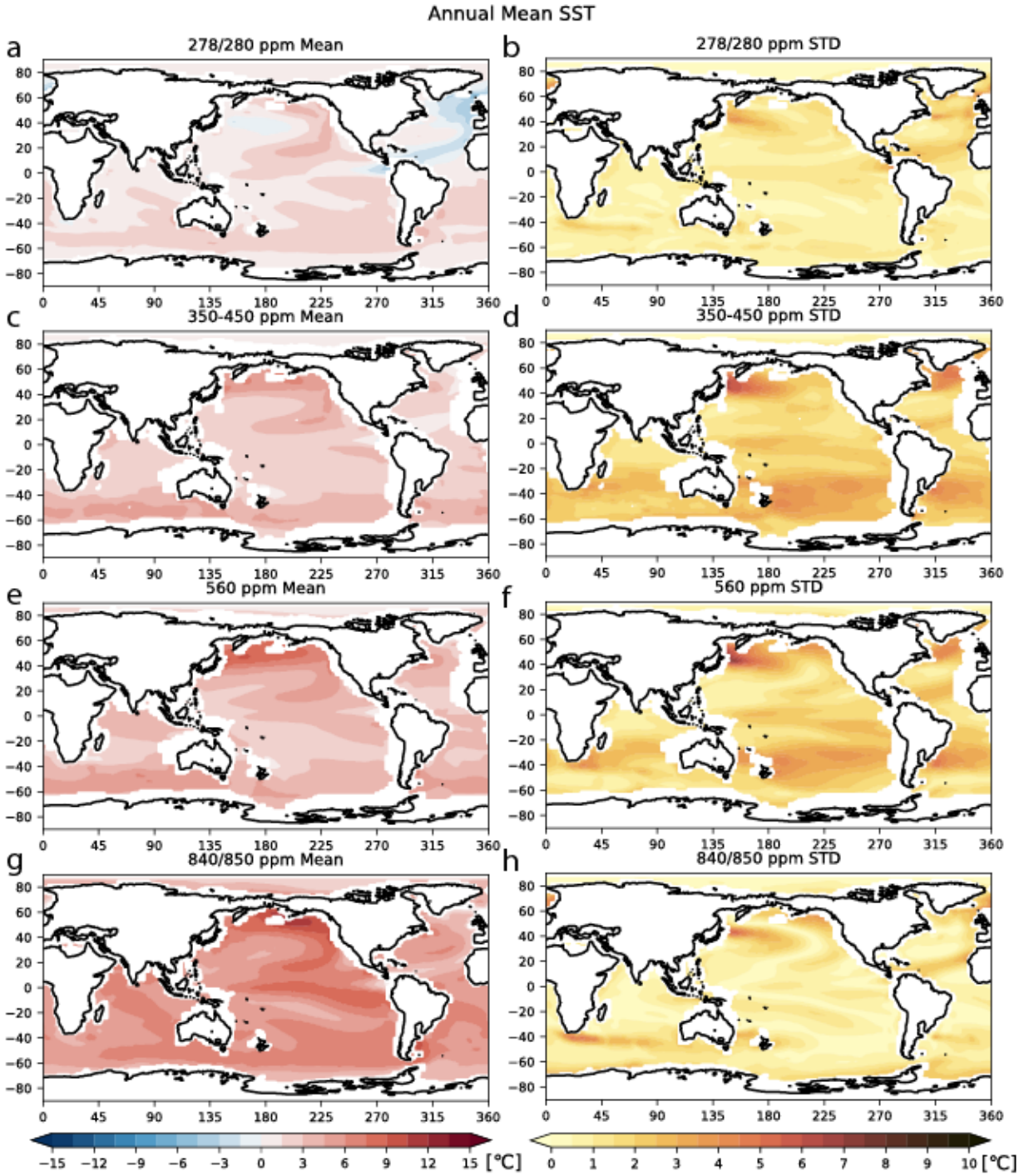

Fig. 7: (Left) The multi-model-mean of the annual mean sea surface temperature change relative to the preindustrial control for the set of experiments with (a) 278 or 280 ppm, (c) 350-450 ppm, (e) 560 ppm, and (g) 840/850 ppm CO_2. (Right) The standard deviation in this temperature change across the experiments making up each set. The continental outline from the updated Herold et al 2011a paleogeographic boundary conditions described in this article has been used (see supplementary information).

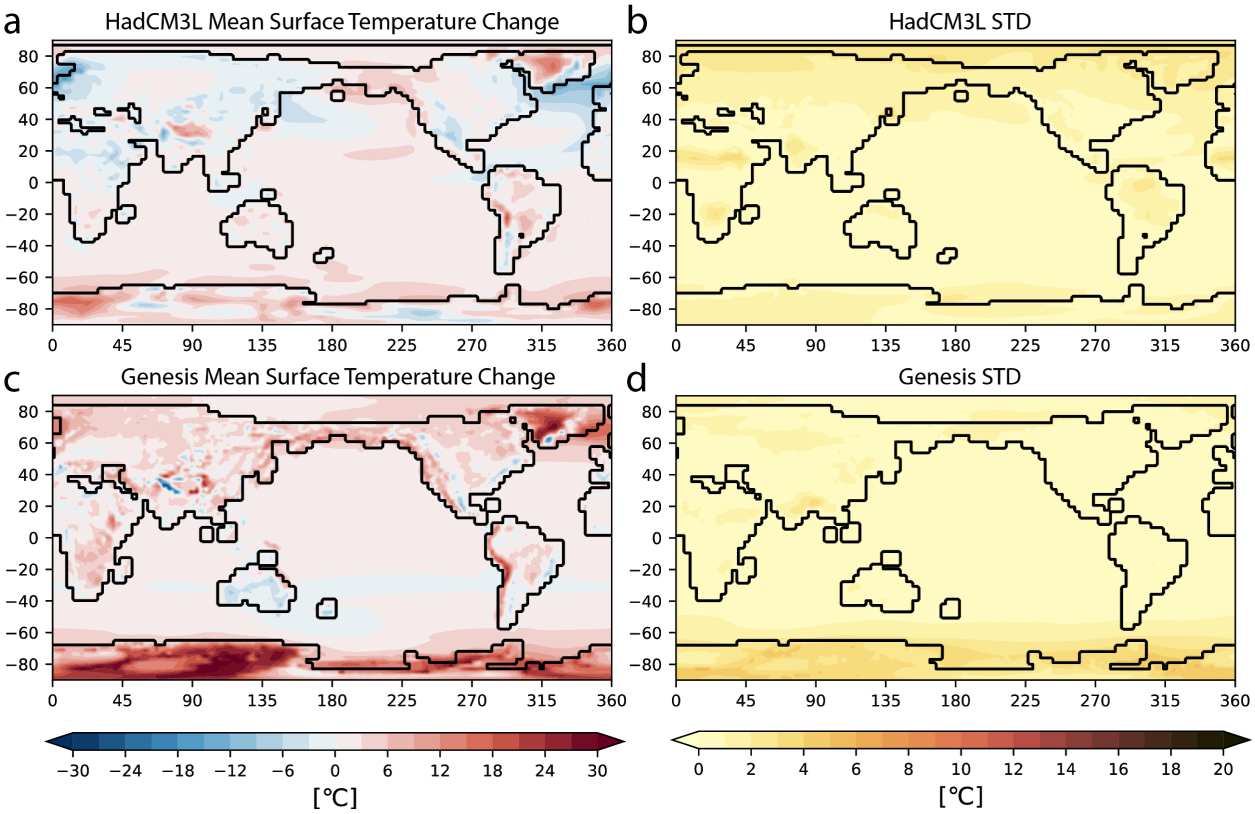

Fig. 8: (Left) The multi-model-mean of the annual mean surface temperature change relative to the preindustrial control for the Orbital sensitivity simulations outlined in Table 3 (a) HadCM3L, (c) Genesis (Table 3, only the simulations that have 280 ppm CO_2). (Right) The standard deviation in this temperature change across the experiments making up each set of (b) HadCM3L, (d) Genesis 280ppm CO_2 experiments. Note that the same colorbar as in Fig. 5 has been used to facilitate comparison. See Fig. S6 for a version of the standard deviation plots that has a colorbar that ranges from 1 to 10°C.

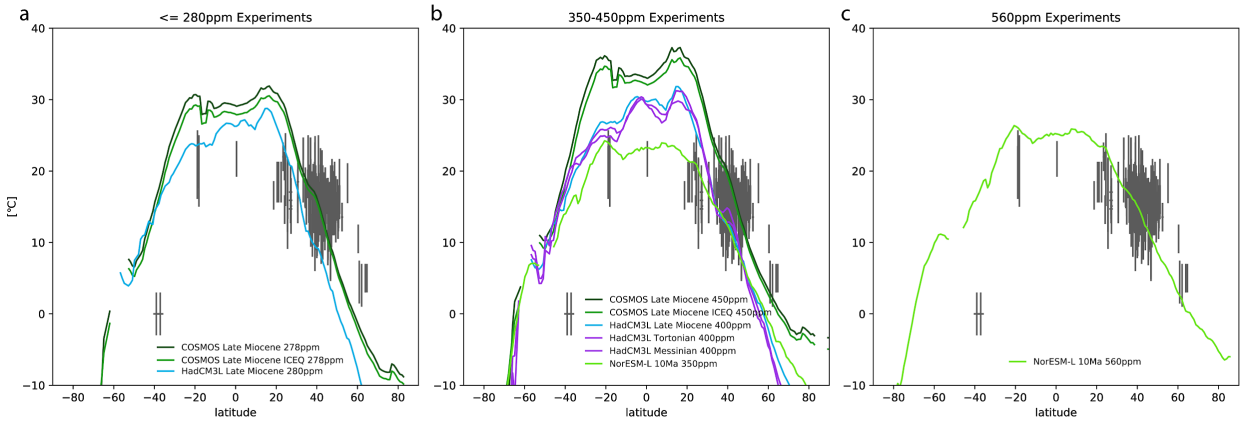

Fig. 9: Zonal-mean, annual-mean land surface temperature for all Late Miocene experiments. Superimposed in gray are Late Miocene in age mean annual terrestrial temperature reconstructions. Each panel distills the Late Miocene experiments by prescribed atmospheric CO_2 concentration.

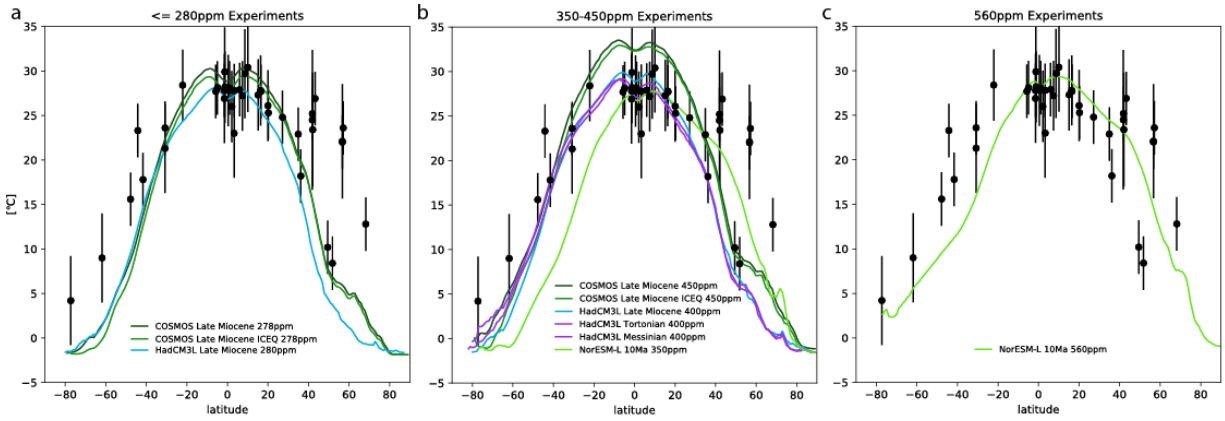

Fig. 10: Zonal-mean, annual-mean, sea surface temperature for all Late Miocene experiments. Superimposed in black are Late Miocene in age mean annual sea surface temperature reconstructions. Each panel distills the Late Miocene experiments by prescribed atmospheric CO_2 concentration.

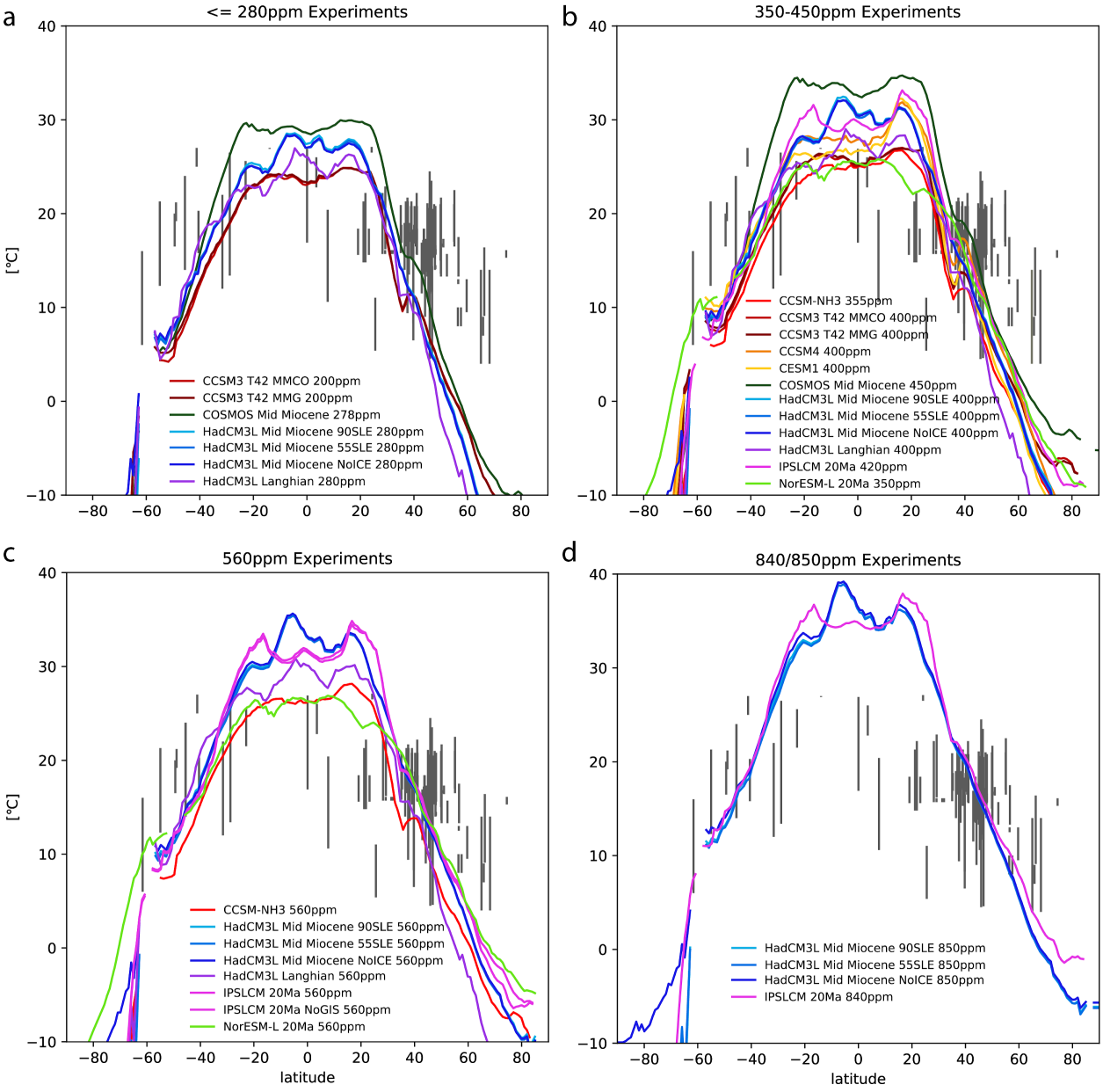

Fig. 11: Zonal-mean, annual-mean land surface temperature for all Middle-Early Miocene experiments. Superimposed in gray are Middle Miocene in age mean annual terrestrial temperature reconstructions. Each panel distills the Middle and Early Miocene experiments by prescribed atmospheric CO_2 concentration.

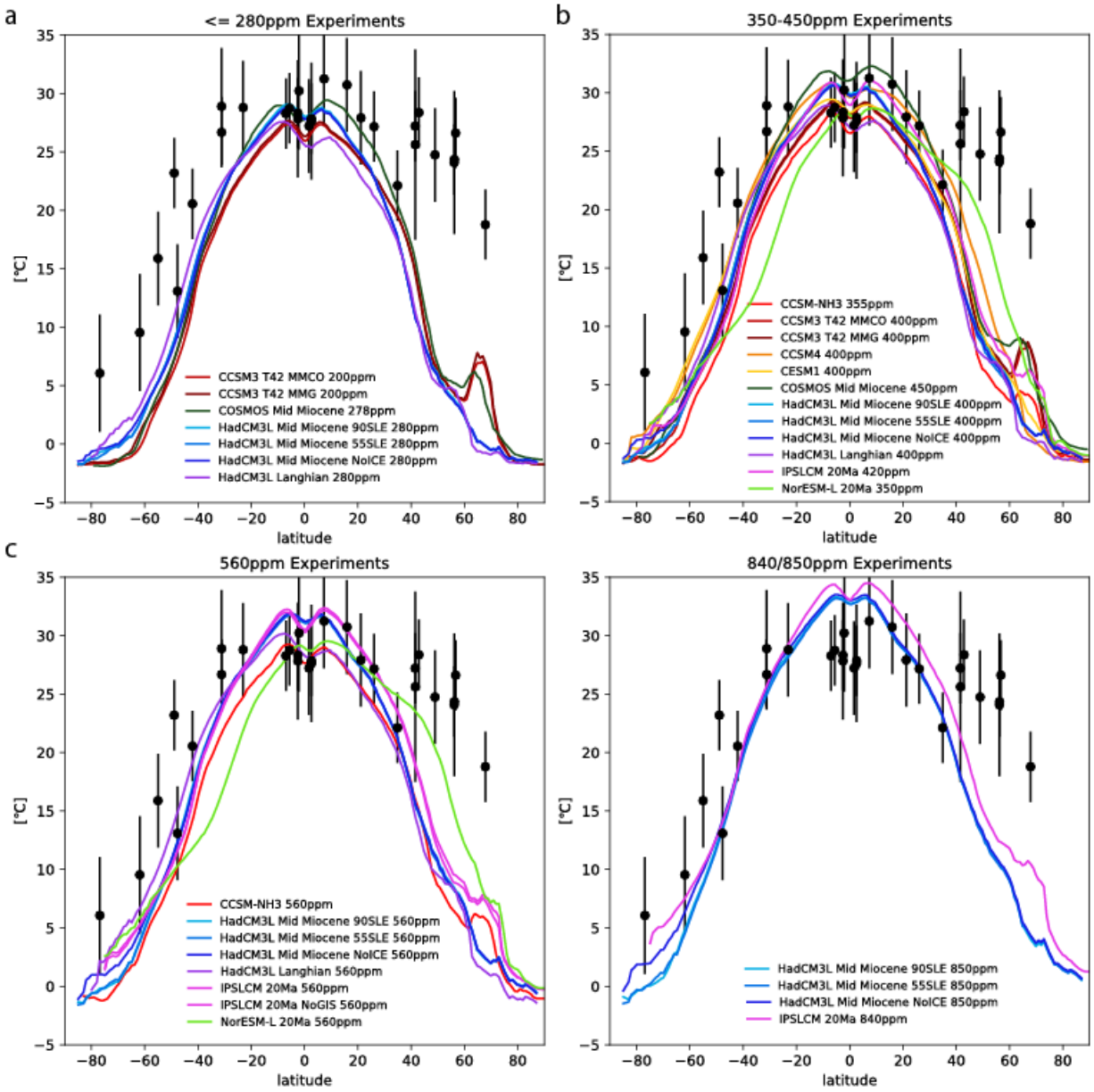

Fig. 12: Zonal-mean, annual-mean, sea surface temperature for all Middle and Early Miocene experiments. Superimposed in black are Middle Miocene in age mean annual sea surface temperature reconstructions. Each panel distills the Middle to Early Miocene experiments by prescribed atmospheric CO_2 concentration.

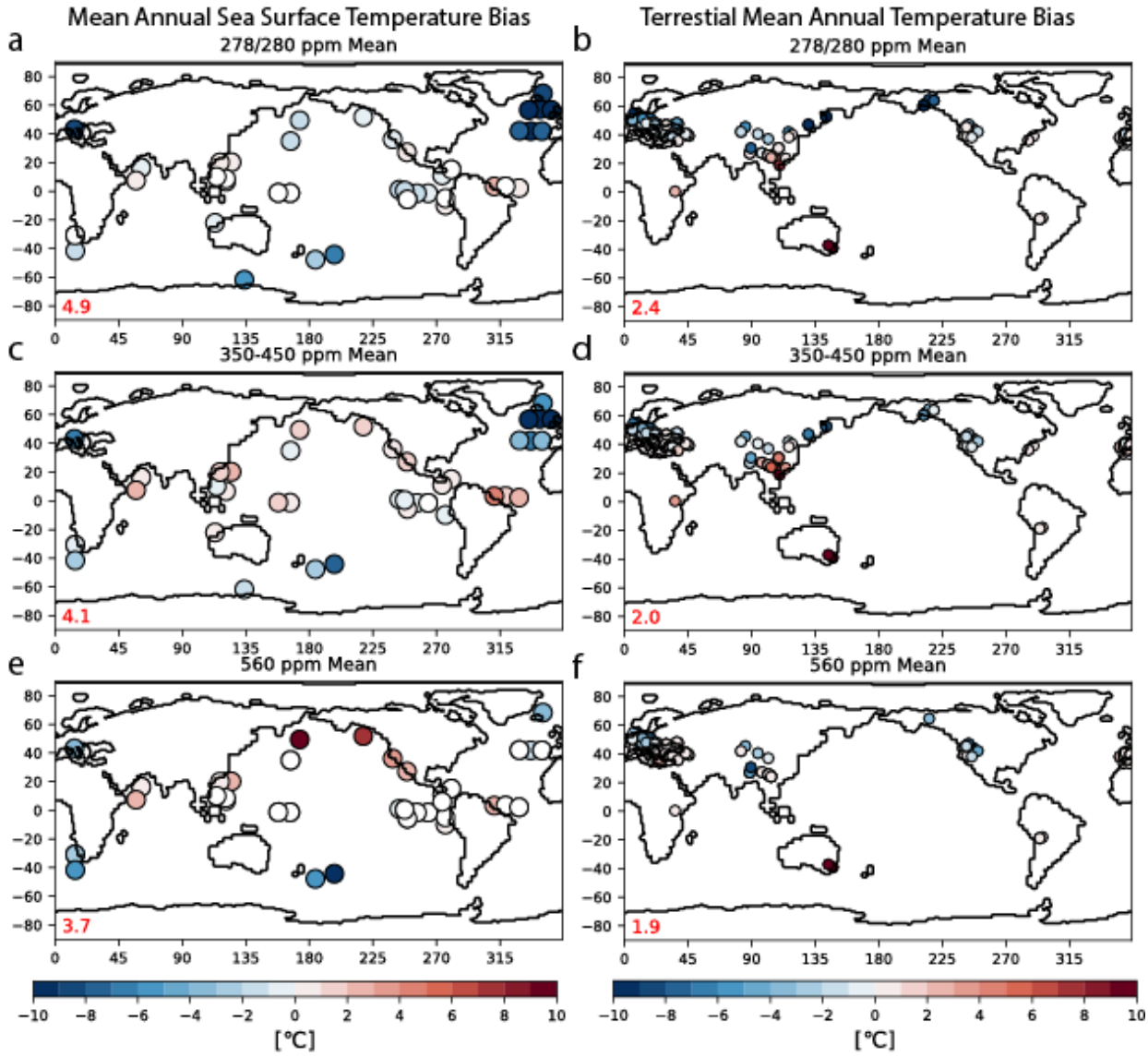

Fig. 13: Late Miocene multi-model-mean (Left) sea surface, (Right) terrestrial mean annual temperature bias. The average of individual model bias at each site (Figs. S8 and S9) is calculated across the set of Late Miocene experiments with (a/b) 278 or 280 ppm, (c/d) 350-450 ppm, (e/f) 560 ppm, and (g/h) 840/850 ppm. The root-mean-square-error across all the sites is shown in red on the bottom left. The continental outline from COSMOS T31 (AWI) (Knorr et al., 2011) has been used.

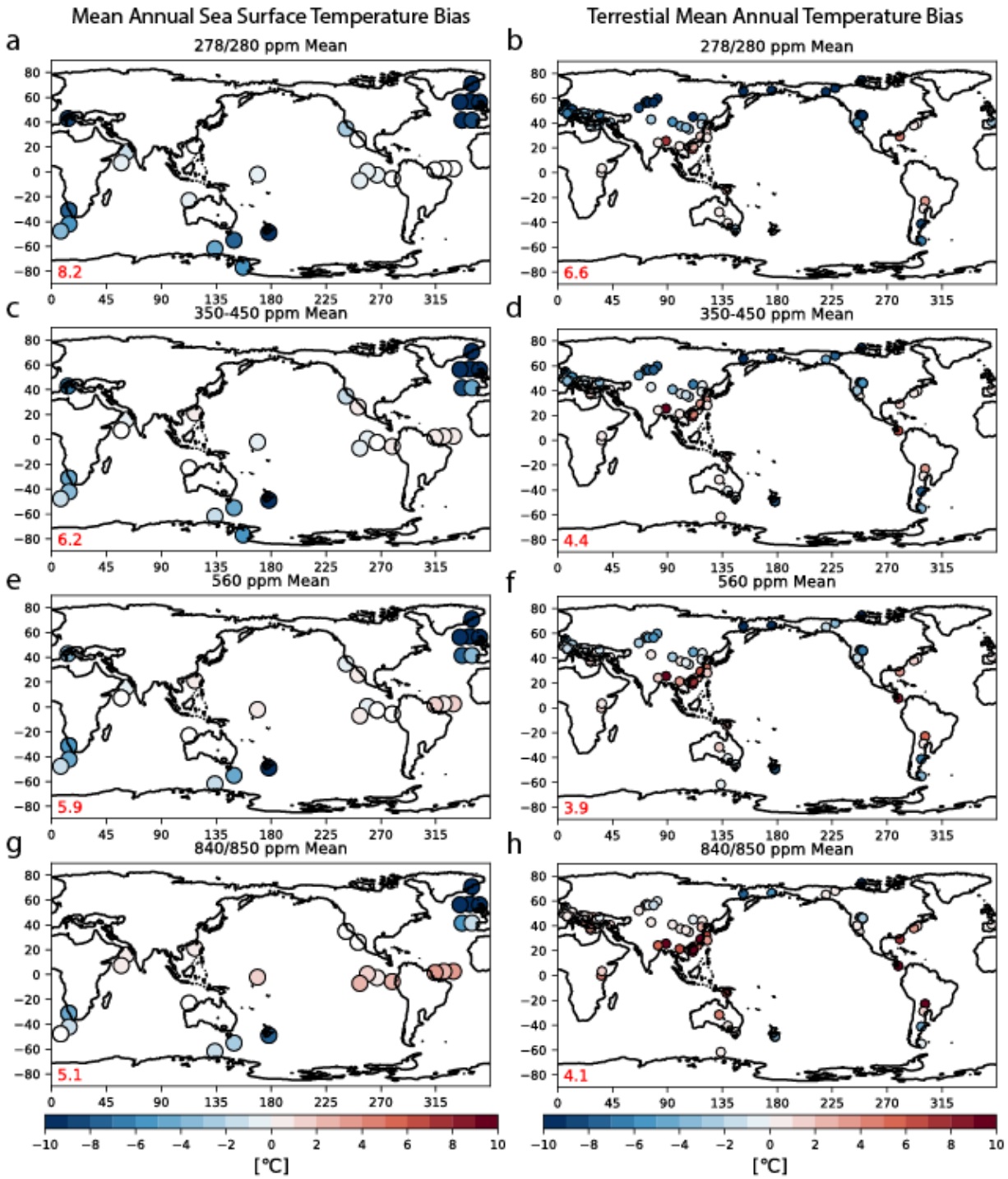

Fig. 14: Middle Miocene multi-model-mean (Left) sea surface, (Right) terrestrial mean annual temperature bias. The average of individual model bias at each site (Figs. S10 and S11) is calculated across the set of Middle to Early Miocene experiments with (a/b) 278 or 280 ppm, (c/d) 350-450 ppm, (e/f) 560 ppm, and (g/h) 840/850 ppm. The root-mean-square-error across all the sites is shown in red on the bottom right. The root-mean-square-error across all the sites is shown in red on the bottom left. The continental outline from CCSM3 T42 (MARUM) (Frigola et al., 2018) has been used.

Paleoceanography and Paleoclimatology

Supporting Information for

Simulating Miocene warmth: insights from an opportunistic Multi-Model ensemble (MioMIP1)

N. J. Burls[1], C. D. Bradshaw[2], A. M. De Boer[3], N. Herold[4], M. Huber[5], M. Pound[6], Y. Donnadieu[7], A. Farnsworth[8], A. Frigola[9], E. Gasson[10], A. S. von der Heydt[11], D. K. Hutchinson[12], G. Knorr[13], K. T. Lawrence[14], C. H. Lear[15], X. Li[16], G. Lohmann[17], Daniel J. Lunt[18], A. Marzocchi[19], M. Prange[20], C. A. Riihimaki[21], A.-C. Sarr[22], N. Siler[23], and Z. Zhang[24,25]

[1] Department of Atmospheric, Oceanic and Earth Sciences & the Center for Ocean-Land-Atmosphere Studies, George Mason University, Fairfax, VA 22030, USA.

[2]The Global Systems Institute, University of Exeter, EX4 4QE, United Kingdom and Met Office Hadley Centre, Exeter EX1 3PB, United Kingdom.

[3]Department of Geological Sciences and Bolin Center for Climate Research, Stockholm University, 10691 Stockholm, Sweden.

[4]The NSW Department of Planning, Industry and Environment, Science Division, Climate and Atmospheric Science, New South Wales, Australia.

[5]Department of Earth, Atmospheric, and Planetary Sciences, Purdue University, West Lafayette, IN, 47907, USA.

[6]Department of Geography and Environmental Sciences, Northumbria University, Newcastle, NE1 8ST, UK.

[7]Aix Marseille Univ, CNRS, IRD, Coll France, INRA, CEREGE, 13545, Aix en Provence, France.

[8]School of Geographical Sciences, University of Bristol, Bristol, BS8 1SS, UK.

[9]MARUM – Center for Marine Environmental Sciences, University of Bremen, Klagenfurter Str., D-28359 Bremen, Germany.

[10]School of Geographical Sciences, University of Bristol, Bristol, BS8 1SS, UK.

[11]Institute for Marine and Atmospheric Research, Department of Physics, Faculty of Science, Utrecht University, Princetonplein 5, 3584CC Utrecht, The Netherlands.

[12]Department of Geological Sciences and Bolin Center for Climate Research, Stockholm University, 10691 Stockholm, Sweden.

[13]Alfred Wegener Institute Helmholtz Centre for Polar and Marine Research, Bussestrasse 24, D-27570, Germany.

[14]Department of Geology and Environmental Geosciences, Lafayette College, 102 Van Wickle Hall, Easton, PA 18042, USA.

[15]School of Earth and Ocean Sciences, Cardiff University, Main Building, Park Place, Cardiff, CF10 3AT, UK.

[16]Department of Atmospheric Science, School of Environmental studies, China University of Geoscience, Wuhan, 430074, China.

[17]Alfred Wegener Institute Helmholtz Centre for Polar and Marine Research, Bussestrasse 24, D-27570, Germany.

[18]School of Geographical Sciences, University of Bristol, Bristol, BS8 1SS, UK.

[19]National Oceanography Centre, Southampton, UK.

[20]MARUM – Center for Marine Environmental Sciences, University of Bremen, Klagenfurter Str., D-28359 Bremen, Germany.

[21]Council on Science and Technology, Princeton University, Princeton, NJ 08544, USA.

[22]Aix Marseille Univ, CNRS, IRD, Coll France, INRA, CEREGE, 13545, Aix en Provence, France.

[23]College of Earth, Ocean, and Atmospheric Sciences, Oregon State University, Corvallis, OR, USA.

[24]Department of Atmospheric Science, School of Environmental studies, China University of Geoscience, Wuhan, 430074, China.

[25]NORCE Norwegian Research Centre, Bjerknes Centre for Climate Research, 5007 Bergen, Norway.

Contents of this file

Additional Supporting Information (Files uploaded separately)

Table S1: New synthesis of global terrestrial MATs generated for the Middle Miocene.

Table S2: Miocene SST reconstructions. Excel file sheet 1, contains a basic description of published Miocene ocean surface temperature records. Sites are identified by their site numbers (Fig. 2), which are primarily from the Deep Sea Drilling Program, Ocean Drilling Program, or Integrated Ocean Discovery Program. The column on the far right contains hyperlinks to where the data for each site can be accessed electronically. Different colors in the proxy column are used to facilitate the ability to rapidly distinguish between records that utilize different SST proxies (Uk'37 = black, Mg/Ca = green, TEX86= purple). Note that all records are on their original age models using their original calibration. Excel file sheet 2, lists the Late Miocene, Middle Miocene and MCO mean SST values and

uncertainty bounds calculated from these records and used in the model-data comparison.

Dataset S1: *On acceptance, the updated version of the Herold et al. (2011a) Miocene boundary conditions used within the new CESM simulations, and described in Text S1, will be provided as supplementary netcdf files and deposited together with the Tables S1 & S2 in the Zenodo repository.*

Dataset S2: *On acceptance, a netcdf file containing the MioMIP variables used to make all the figures shown will be deposited in the Zenodo repository.*

Text S1.

Description of updated paleogeography

The starting point for this revised paleogeography is the 0.5 x 0.5 degree Miocene dataset described in Herold et al. 2008 with the minor modifications in Herold et al., 2011a included. See Herold et al. 2008 for a description of the base methodology. Below we describe the additional changes that have been made to make our paleogeography more consistent with the available literature. The Greenland-Scotland Ridge (GSR) was likely shallow or above sea-level during the early to middle Miocene, with the exception of the Faroe-Shetland Channel which was relatively deep (Poore et al., 2006). Such details are not reconstructed by the method of Mueller et al., 2008a (used by Herold et al. 2008) given the generic workflow which utilises an age-depth relationship, sediment deposition and Large Igneous Province (LIP) emplacement. Consequently, in the Herold 2008 dataset the GSR was almost absent and Iceland was below sea level, having potentially large implications for deep water formation (Herold et al., 2012; Robinson et al., 2011). To correct this discrepancy, a shallow (-100 m) GSR with a deep Faroe-Shetland Channel (~ -4,500 m to be consistent with surrounding bathymetry) is implemented. Based on fossil flora Iceland is known to have been sub-areal in the middle Miocene (Denk et al., 2005; Grimsson et al., 2007).

While Mueller et al. 2008b implement large igneous provinces (LIPs) in their paleobathymetry there is some error associated with their methods. For the Miocene, the estimated depths of some LIPs were checked against foraminifera-based depth estimates from deep sea drilling data. Accordingly, based on drilling reports the Madagascar Ridge, Mascarene Ridge and Kerguelen Plateau are adjusted to approximately 900, 700 and 2000 m depth respectively. Australian geography was adjusted to better suit the paleogeography established by Langford et al., (1995), namely marine transgressions in the southwest and southeast of the continent. The topography of Papua New Guinea was substantially reduced (to about 30% of the modern) given that the central mountain chain of the island did not uplift until the latest Miocene (van Ufford and Cloos, 2005). The Amazon River was removed in our revised dataset. Evidence suggests the early Miocene Amazon reflected a "mega-wetland" which drained into the Caribbean, switching its drainage channels toward the Atlantic in the middle to late Miocene (Hartley, 2008; Hoorn et al., 2010; Shephard et al., 2010 and references therein). Based on this

data we suggest that the Amazon be represented using a "wetland" plant functional type in climate models (as was done for the CCSM4 simulations; Table 2), though individual modellers may choose to represent the Amazon by changing the land mask to ocean at appropriate grid cells. A marine incursion in southern South America was also implemented based on Markwick (2007).

The Panama gateway was likely open by the early-middle Miocene (see Molnar 2008, for a review), though contradictory evidence exists suggesting no deep passage by 15 Ma (Montes et al., 2012). A geography consistent with that of Iturralde-Vincent (2006) was chosen, leaving only a deep meridional channel between the Pacific and Atlantic Oceans. The Tethys and Mediterranean were re-modelled based on the geographic outline of Karami (2011), which was derived from Meulenkamp and Sissingh (2003). The bathymetry of the Miocene Tethys Ocean is largely unknown, though some information can be gleaned (Hüsing et al., 2009; Meulenkamp and Sissingh, 2003). A somewhat deep bathymetry from the Strait of Gibraltar into the central Mediterranean has been implemented, qualitatively consistent with these studies.

Perhaps the most significant improvement in this revised Miocene paleogeography is the treatment of the Greenland and Antarctic ice-sheets. While the Cenozoic history of the Antarctic ice-sheet is ambiguous there is broad agreement that between the Eocene-Oligocene Transition (~34 Ma) and Middle Miocene Climate Transition (~14 Ma) the East Antarctic ice-sheet experienced significant fluctuations in volume and extent, whereas the West Antarctic Ice Sheet was likely non-existent or insignificantly small (Cramer et al., 2011; Pekar and DeConto, 2006; Zachos et al., 2001). Pekar and DeConto (2006) estimate early Miocene ice volume to be 25 – 70% of the modern East Antarctic Ice Sheet (the contribution of the modern EAIS is equal to ~60 m sea-level rise after isostatic rebound). Cramer et al. (2011) calculated a more conservative ice-volume decrease for the Miocene, with their minimum predicted Miocene ice-volume ~55% of the present (based on a sea-level rise of ~30 m above present, compared to ~65 m for all ice-sheets). An ice-volume and sea-level rise consistent with extreme warmth in the Miocene was chosen. The Antarctic topography is derived from a combination of two datasets. The basis of our Antarctic topography and ice-sheet mask is ice-sheet model output provided by David Pollard (personal comms), calculated using the same methodology as in Pollard and DeConto (2009). This simulated ice-sheet is underlain by modern bedrock and consists of approximately ~6.5 million km^3 of ice, compared to the modern Antarctic ice-sheet volume of ~27 million km^3 (Fretwell et al., 2012). The majority of this simulated ice resides in East Antarctica. For West-Antarctica a modification to this topography is applied as follows: for each grid cell where an ANTSCAPE derived dataset is higher than our base topography then it is used instead. The ANTSCAPE dataset is produced as a sum of 40% Eocene maximum topography, as seen in Figure 5 Wilson et al., (2012) and 60% modern bedrock. This is done in light of the suggestion that West Antarctic bedrock was higher than present at the Eocene-Oligocene Transition (Wilson and Luyendyk, 2009) and thus probably lay somewhere between modern and Eocene-Oligocene elevations during the Miocene.

For the Greenland ice-sheet a simulated distribution under a mean Pliocene orbit and an atmospheric CO_2 concentration of 560 ppmv is used (Dolan, 2012), and has a volume of ~0.294

million km^3 (compared to 2.6 million km^3 at present; Weidick et al., 1995). The difference in insolation between a mean Pliocene and Miocene orbit is small (and is smaller than the difference between the present and Miocene orbit), thus this ice-sheet is thought to be an adequate representation for the MCO. It should be noted that evidence for significant Greenland ice-sheets prior to the Pleistocene is scarce. Thus, like our Antarctic ice-sheet, this ice-volume is subject to some indirect inference. In total, our global Miocene ice-volume is ~6.8 million km^3, compared to a global (Antarctica+Greenland) modern volume of 29.6 million km^3 (Fretwell et al., 2012; Weidick et al., 1995). Sea-level change is left at 50 m above present as per Herold et al. (2008) and is consistent with the 65 m sea-level contribution from all of the modern ice-sheets and the 6.8 million km^3 volume of our Miocene ice-sheets.

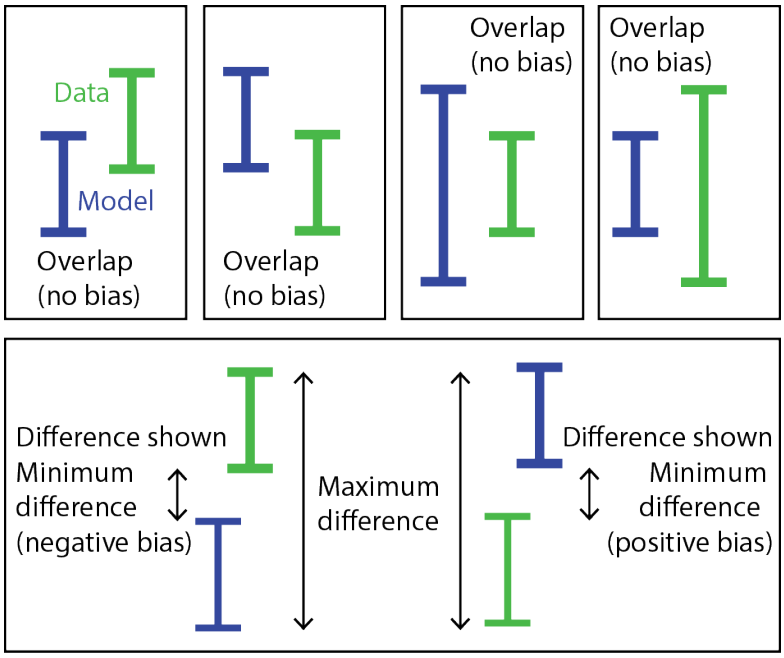

Figure S1. Schematic illustrating the method used to calculate model-data bias. Note that the model uncertainty is derived by including the spread in values across neighboring grid cells.

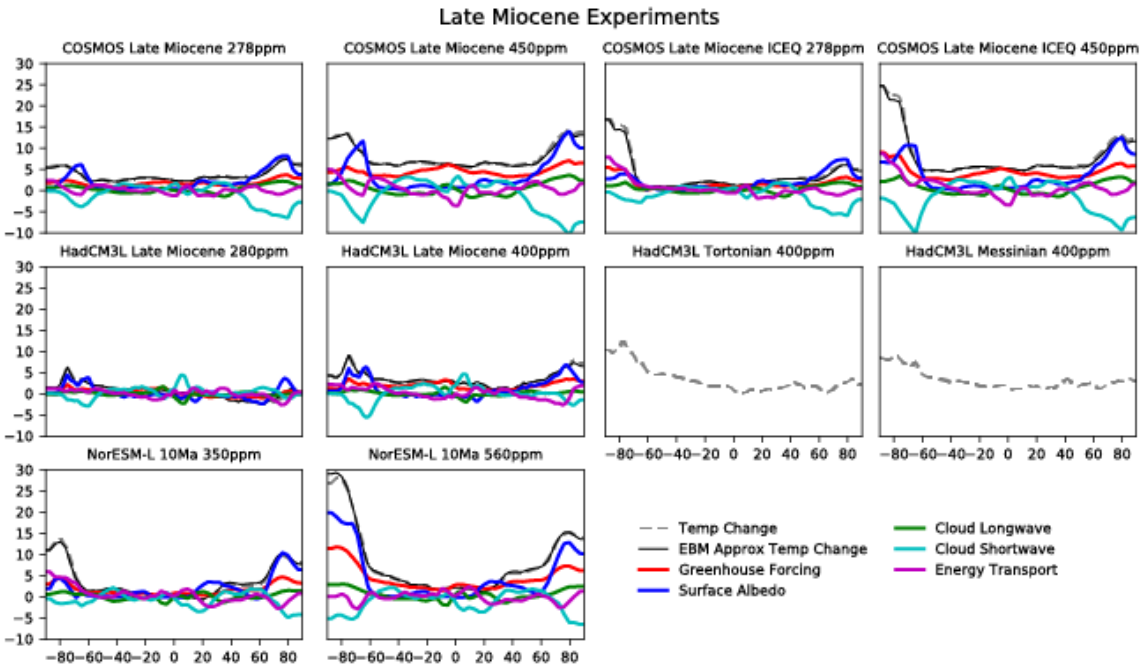

Fig. S2. Zonal mean energy balance analysis for each Late Miocene simulation. Note that the variables required for this analysis were not available for the HadCM3L Tortonia and Messinian experiments.

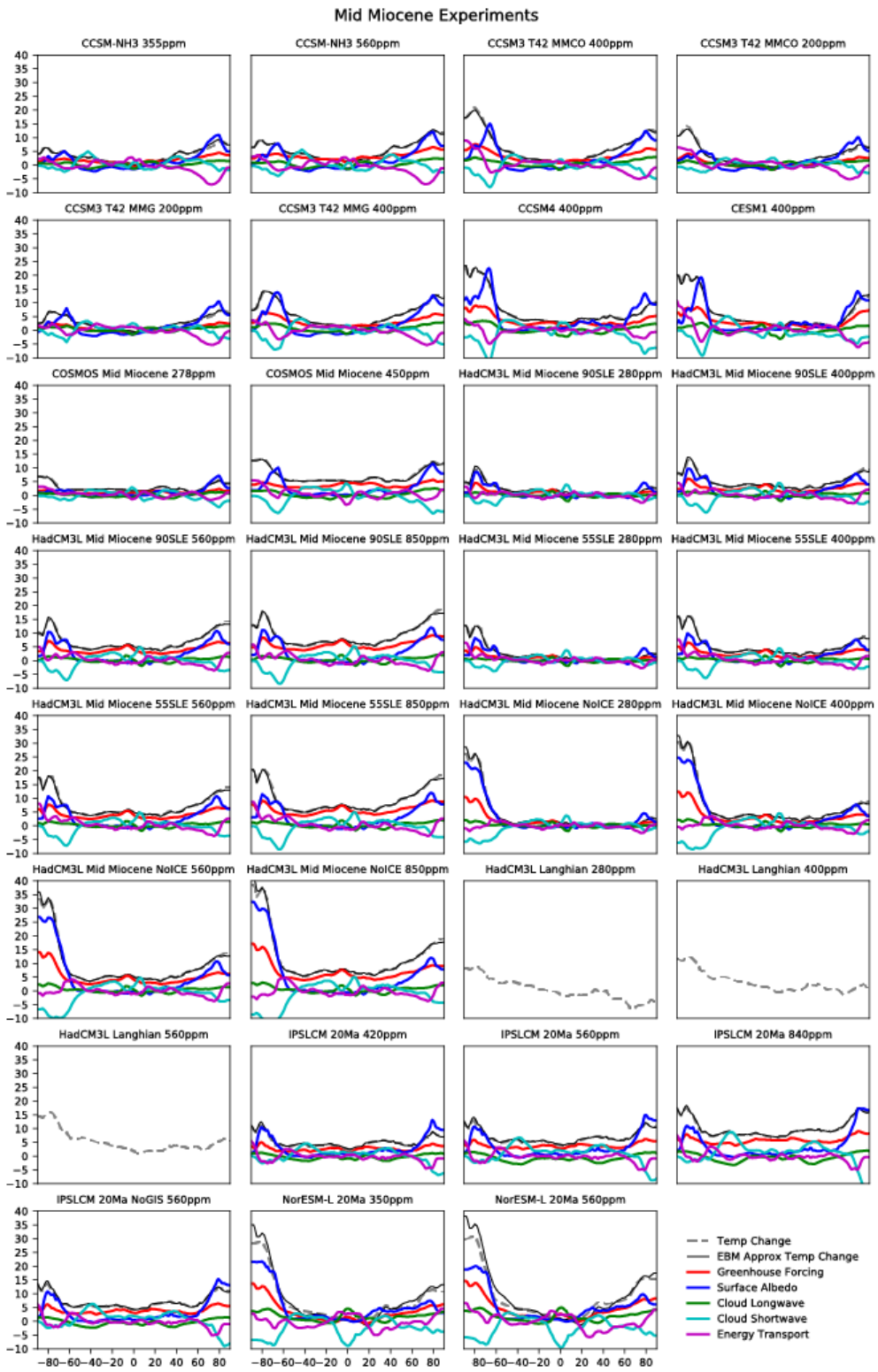

Fig. S3. Zonal mean energy balance analysis for each Middle-Early Miocene simulation. Note that the variables required for this analysis were not available for the HadCM3L Langhian experiments.

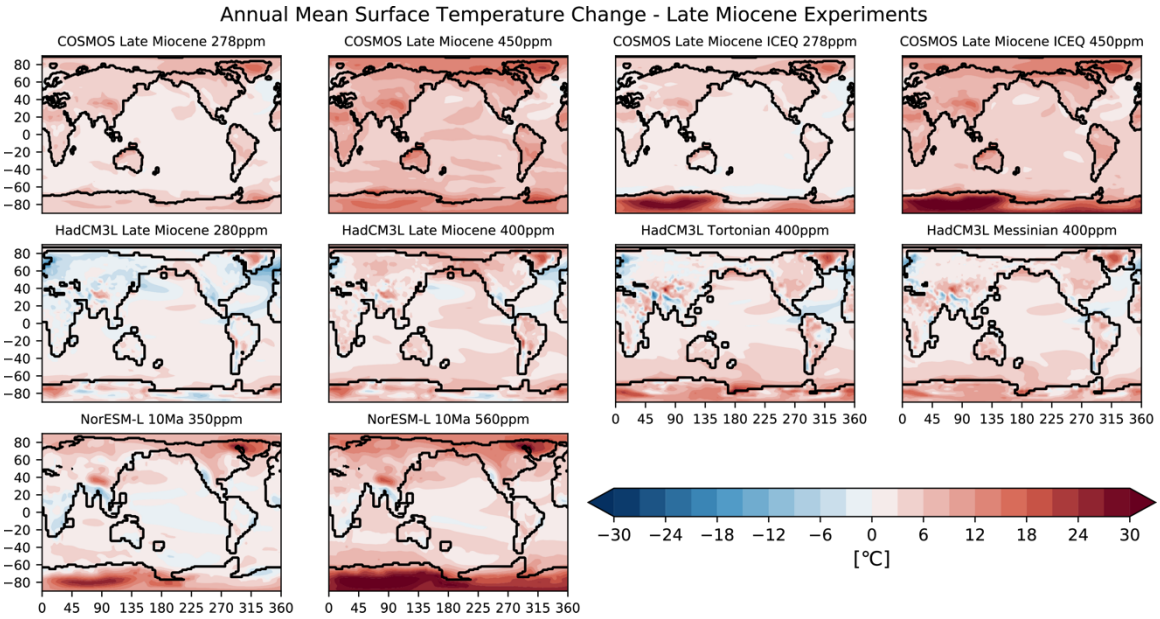

Figure S4. The annual mean surface temperature change relative to the preindustrial control for each Late Miocene simulation listed in Table 1.

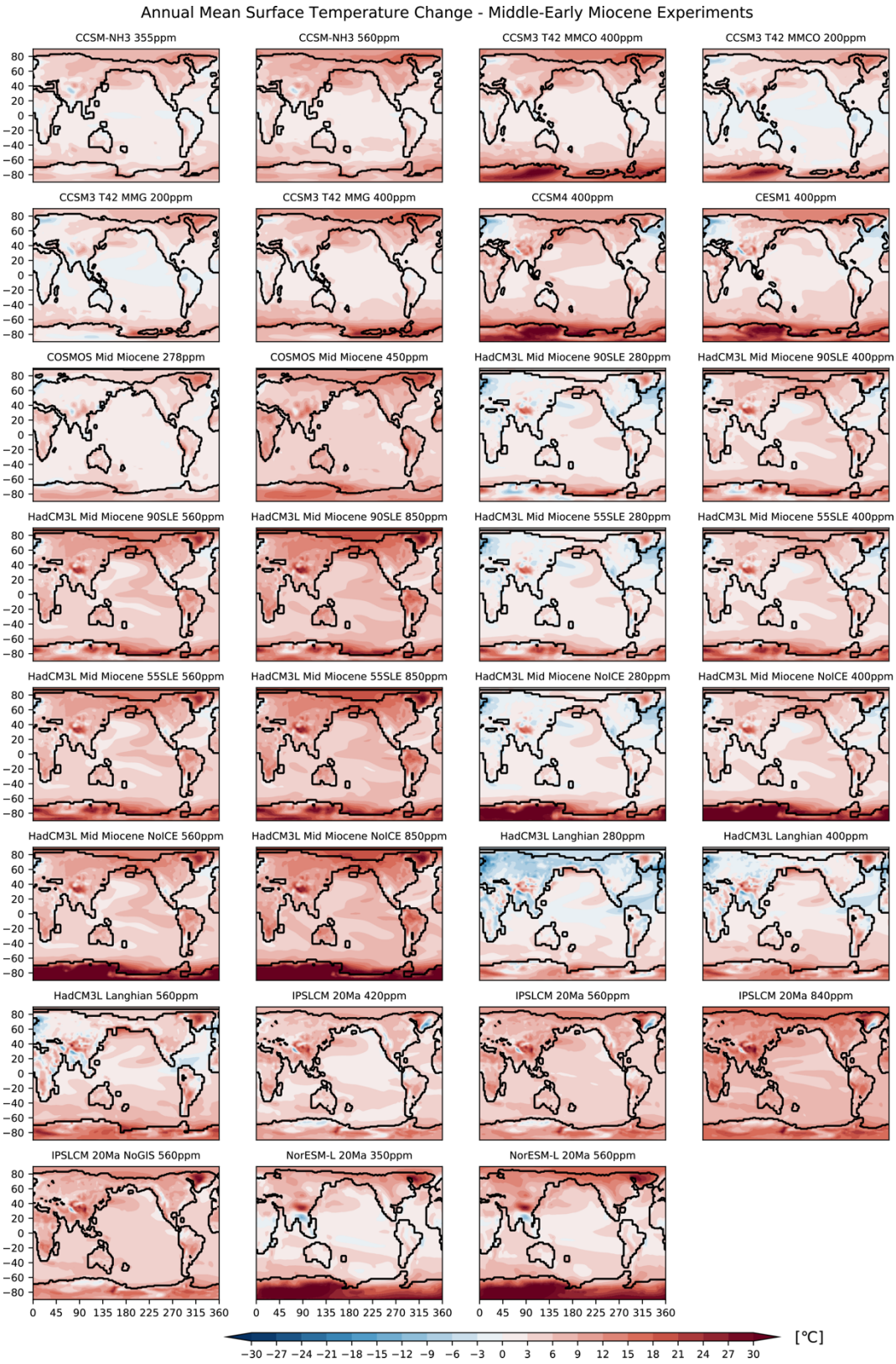

Figure S5. The annual mean surface temperature change relative to the preindustrial control for each Middle to Early Miocene simulation listed in Table 2.

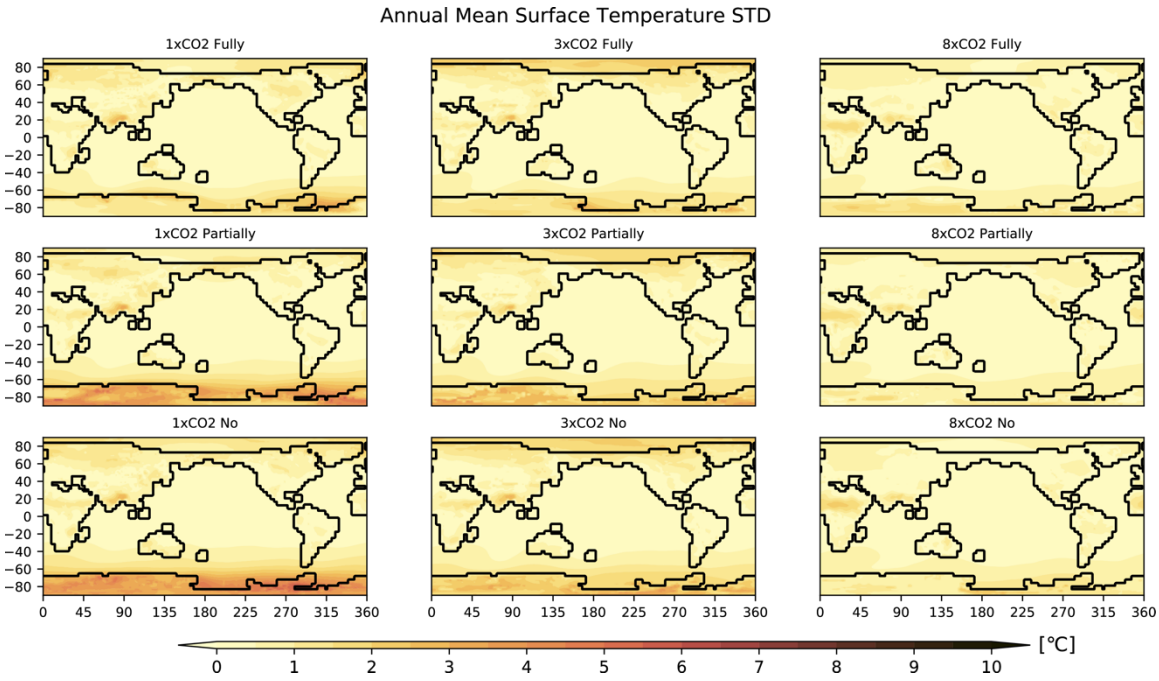

Figure S6. The standard deviation due to varying orbital forcing within the Genesis slab-ocean experiments stratified by CO_2 forcing (1x, 3x, 8x) and Antarctic ice sheet extent (Full, Partial, No).

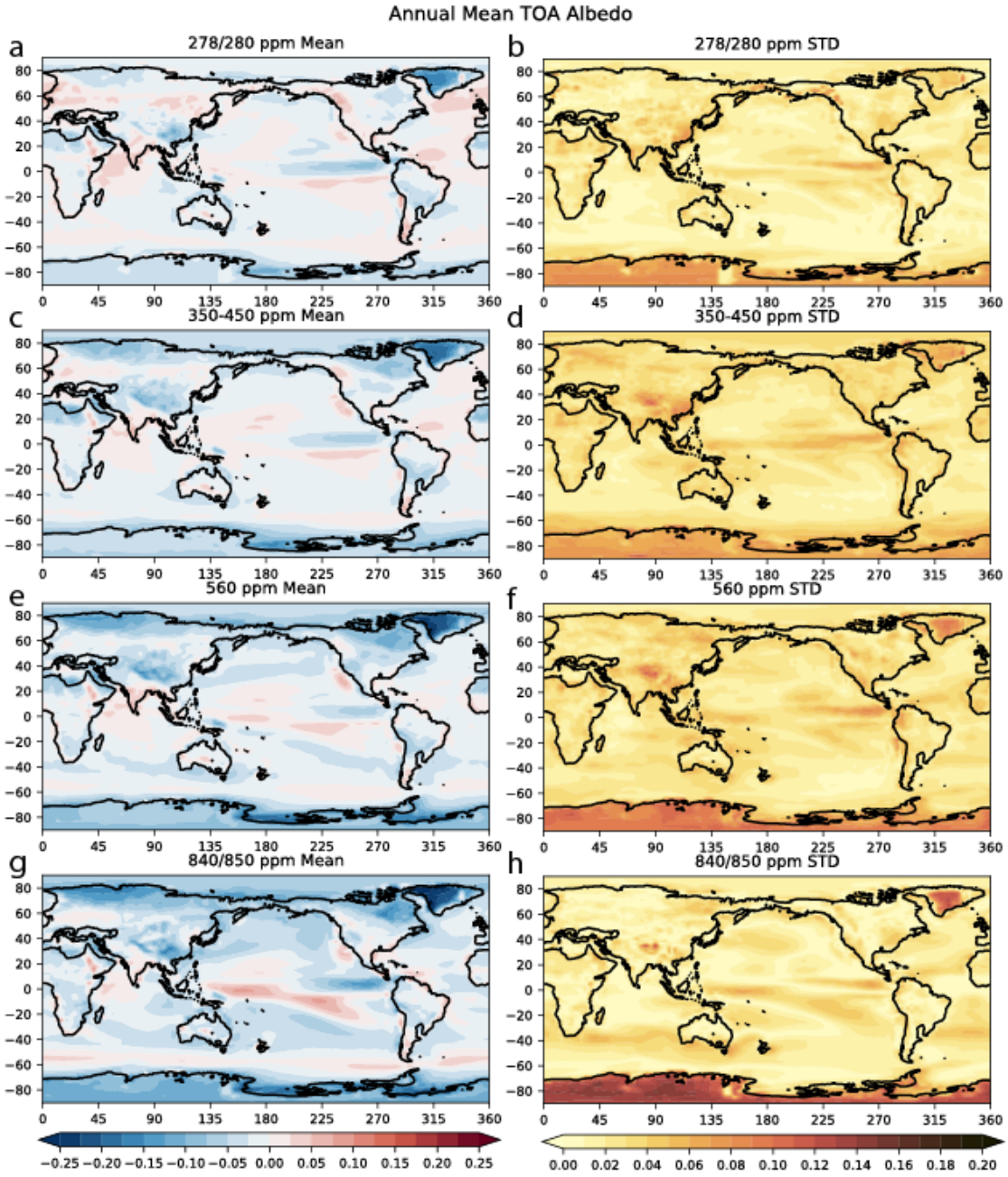

Fig. S7. (Left) The multi-model-mean of the annual mean top-of-the-atmosphere albedo change relative to the preindustrial control for the set of experiments with (a) 278 or 280 ppm, (c) 350-450 ppm, (e) 560 ppm, and (g) 840/850 ppm. (Right) The standard deviation in this albedo change across the experiments making up each set. The continental outline from the updated Herold et al 2011a paleogeographic boundary conditions described in this article has been used.

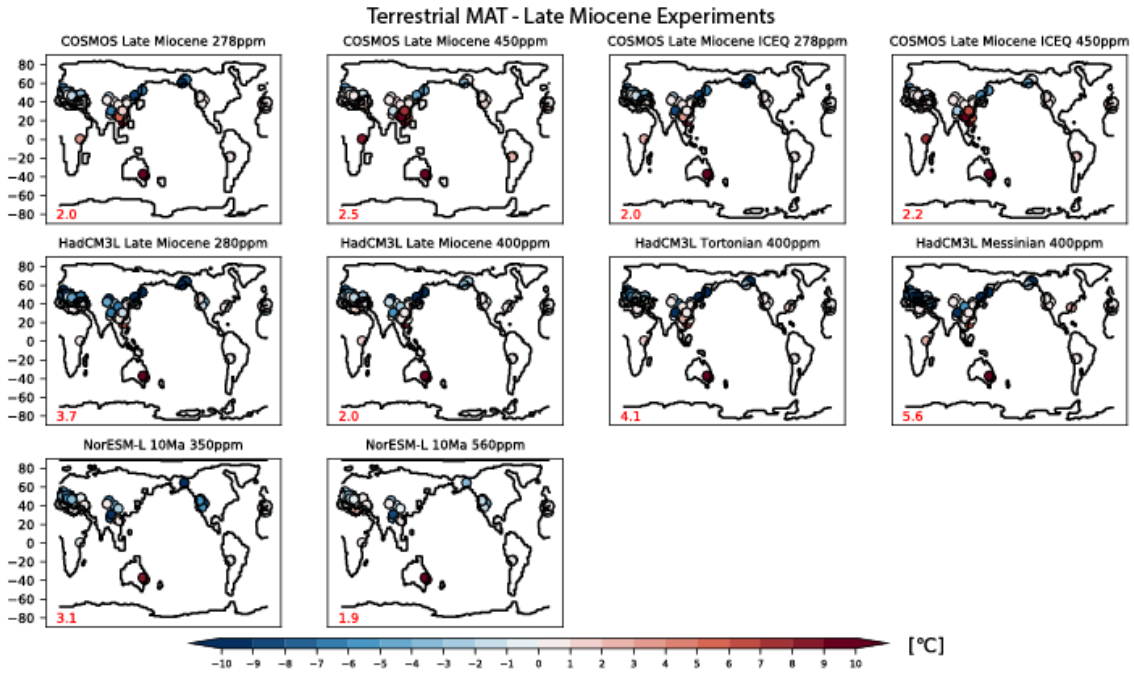

Figure S8. Late Miocene mean annual terrestrial temperature bias for each Late Miocene simulation listed in Table 1. The root-mean-square-error across all the sites is shown in red at the bottom right.

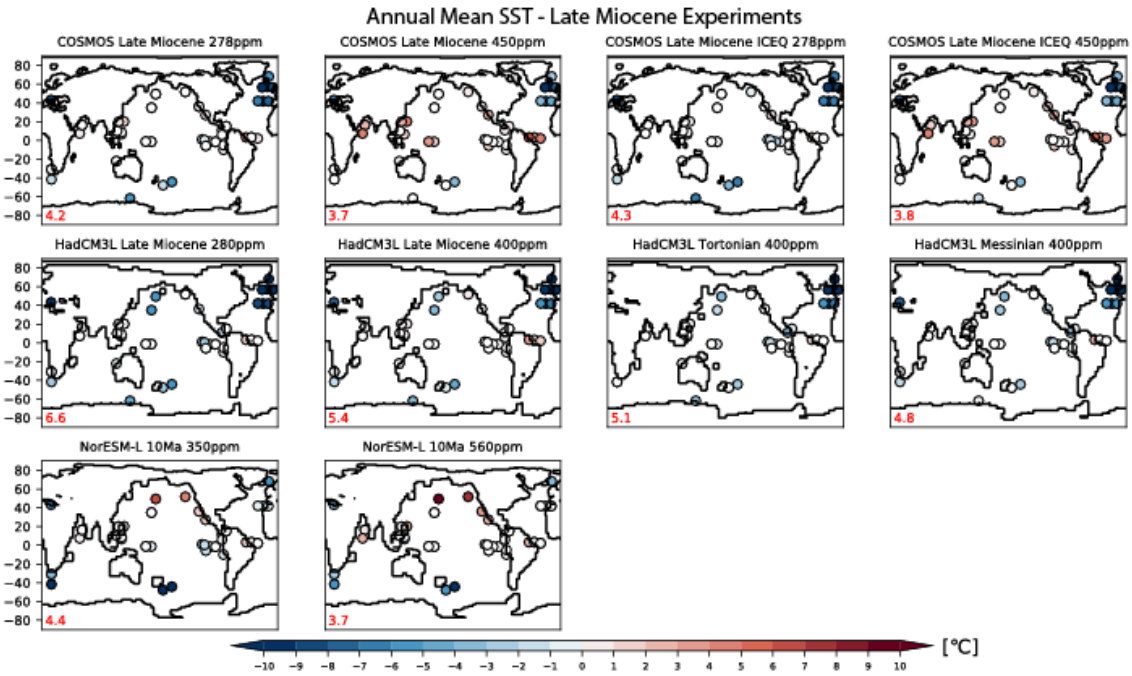

Figure S9. Late Miocene mean annual sea surface temperature bias for each Late Miocene simulation listed in Table 1. The root-mean-square-error across all the sites is shown in red at the bottom right.

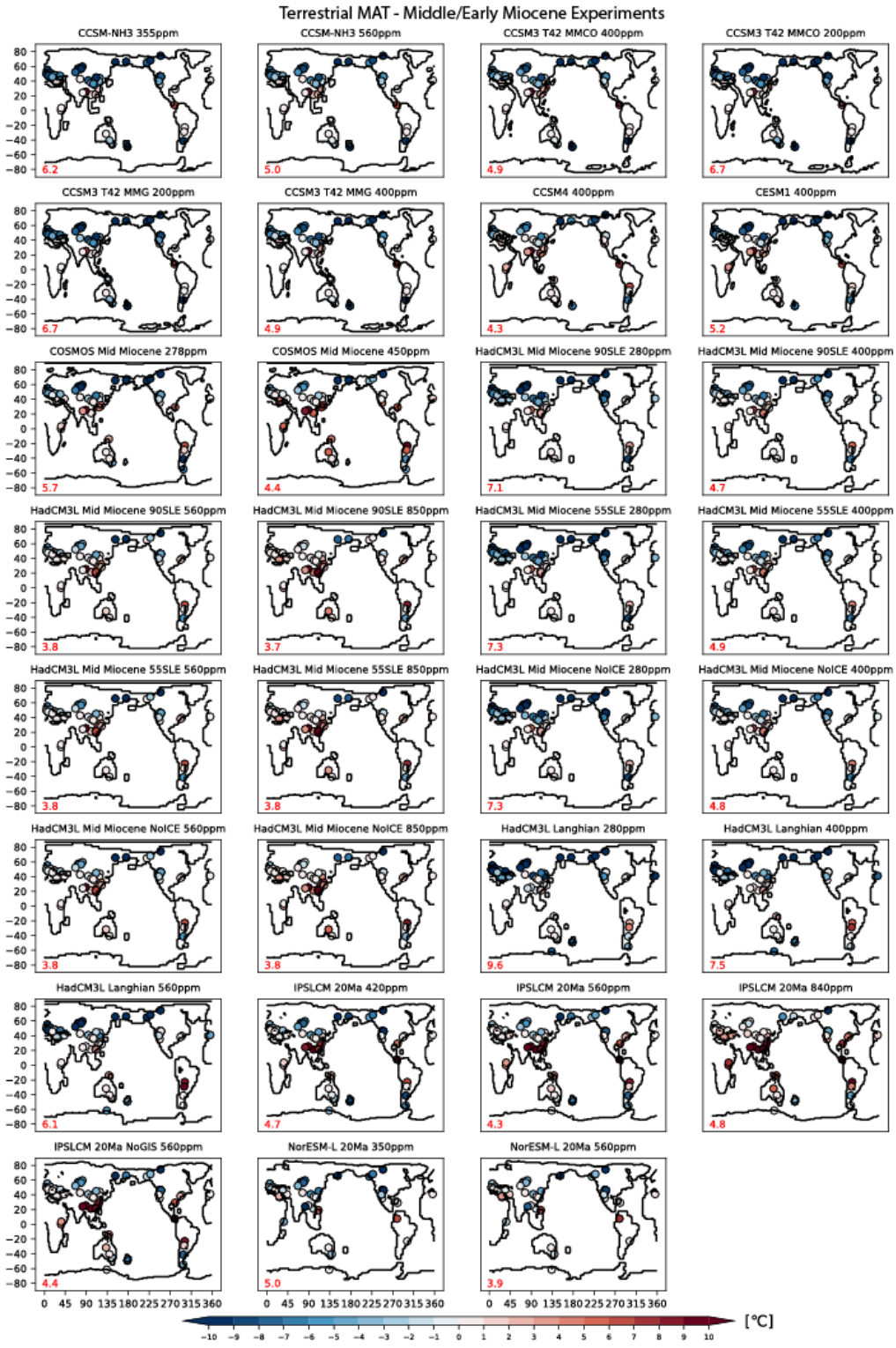

Figure S10. Middle Miocene mean annual terrestrial temperature bias for each Middle to Early Miocene simulation listed in Table 2. The root-mean-square-error across all the sites is shown in red at the bottom right.

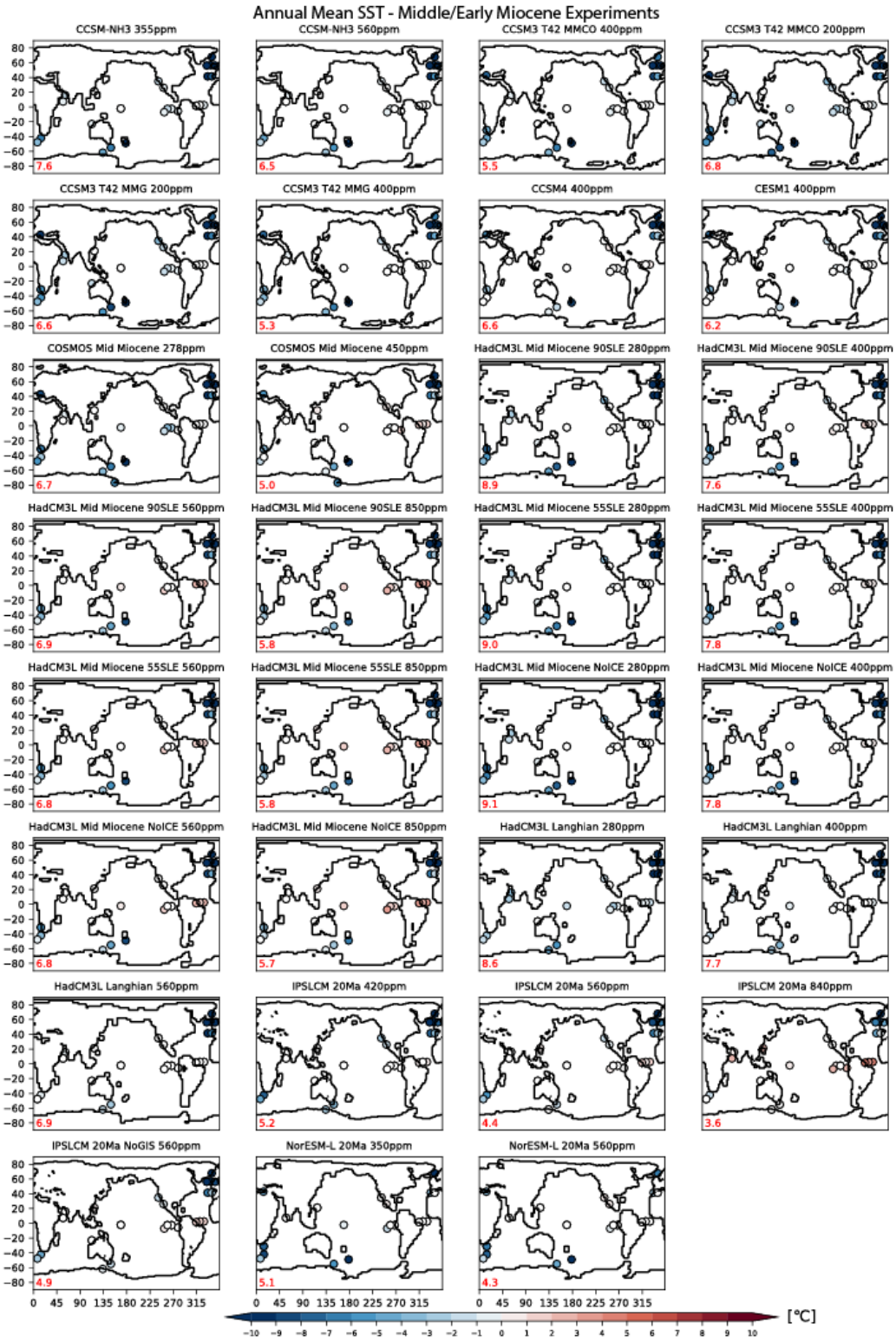

Figure S11. Middle Miocene mean annual sea surface temperature bias for each Middle to Early Miocene simulation listed in Table 2. The root-mean-square-error across all the sites is shown in red at the bottom right.

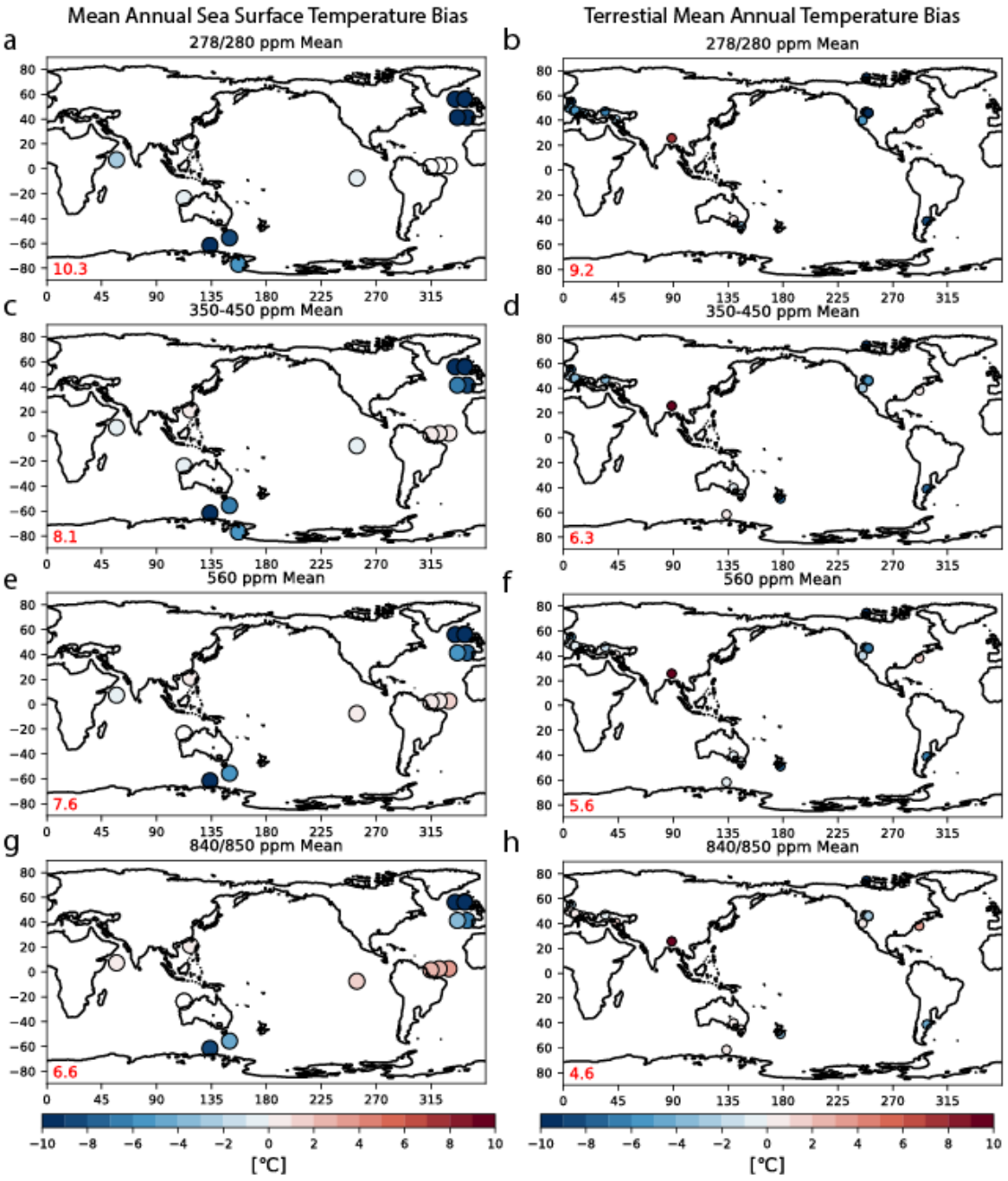

Figure S12. Miocene Climatic Optimum multi-model-mean (Left) sea surface, (Right) terrestrial mean annual temperature bias. The average of the individual model bias at each site is calculated across the set of Middle to Early Miocene experiments with (a/b) 278 or 280 ppm, (c/d) 350-450 ppm, (e/f) 560 ppm, and (g/h) 840/850 ppm. The root-mean-square-error across all the sites is shown in red at the bottom right.